FACULDADE DE ENGENHARIA DA UNIVERSIDADE DO PORTO

Utilizing iron and steel slag as a sustainable material for thermal energy storage

Mariana Magalhães da Cunha Dias

Master's degree in Mechanical Engineering
Fluids and Energy

Supervisor at DTU: Prof. Ming Chen

Co-Supervisor at DTU: Dr. Akhil Panicker

Supervisor at FEUP: Prof. Vítor Leal

July 23, 2026

© Mariana Magalhães da Cunha Dias, 2026

Utilizing iron and steel slag as a sustainable material for thermal energy storage

Mariana Magalhães da Cunha Dias

Master's degree in Mechanical Engineering
Fluids and Energy

Approved in oral examination by the committee:

President: Prof. Paulo Coelho
Examiner: Dr. Behzad Sichani
Member: Prof. Vítor Leal

July 23, 2026

Abstract

Accelerating the integration of intermittent renewable energy sources requires cost-effective and scalable energy storage systems to mitigate the temporal mismatch between electricity generation and grid demand. High-temperature sensible heat thermal energy storage (TES) using packed-beds presents a robust solution. However, relying on natural stones raises resource sustainability concerns. This dissertation evaluates the techno-economic viability of utilizing Electric Arc Furnace (EAF) slag, an abundant industrial byproduct, as an alternative sustainable solid storage medium.

A transient 2D finite element model was developed in COMSOL Multiphysics to simulate the coupled fluid dynamics and thermal behavior within the porous matrix. Restricting the numerical simulations to the charging and resting phases proved sufficient to completely capture the system's performance limits. The charging phase effectively quantified peak pressure drops and maximum thermal capacities, while the resting phase characterized thermocline degradation (front smearing) governed by conduction and axial thermal dispersion.

These physical performance boundaries were subsequently integrated into a MATLAB based economic optimization framework. The techno-economic analysis revealed a critical trade-off between tank geometry and fan pumping power. By implementing an optimized modular architecture composed of multiple parallel units and limiting the maximum porous domain length to 5 m, fluid resistance was successfully minimized, ensuring low auxiliary electricity consumption. Under these optimized multi-unit configurations, the system achieved a highly competitive Levelized Cost of Storage (LCOS) of 6.10 USD/MWh_e for an upscaled grid-scale 100 MWh_{th} facility. These results demonstrate that EAF slag packed-bed systems operate at a small fraction of the cost of chemical batteries or long-term storage hydrogen systems.

Ultimately, this research validates that combining industrial waste revalorization with targeted geometric design provides a highly viable, circular-economy pathway toward low-cost grid stabilization and industrial heat recovery.

Keywords: Thermal Energy Storage (TES) • Packed-bed • Electric Arc Furnace (EAF) Slag • Finite Element Method (FEM) • Techno-Economic Analysis • Levelized Cost of Storage (LCOS)

Resumo

A aceleração da integração de fontes de energia renováveis intermitentes requere sistemas de armazenamento de energia economicamente viáveis e escaláveis para mitigar o desfasamento temporal entre a geração e a procura na rede elétrica. O armazenamento de energia térmica (TES) de alta temperatura por calor sensível em leitos compactados apresenta uma solução robusta. Porém, a dependência de pedras naturais levanta preocupações de sustentabilidade e escassez de recursos. Esta dissertação avalia a viabilidade técnico-económica da utilização de escória de forno de arco elétrico (EAF), um subproduto industrial abundante, como meio de armazenamento sólido alternativo e sustentável.

Foi desenvolvido um modelo transiente em elementos finitos 2D no software COMSOL Multiphysics para simular a dinâmica de fluidos acoplada e o comportamento térmico no interior da matriz porosa. A restrição das simulações numéricas às fases de carga e repouso revelou-se suficiente para delimitar completamente os limites de desempenho do sistema. A fase de carga quantificou com sucesso as perdas de carga máximas e a capacidade térmica máxima, enquanto a fase de repouso caracterizou a degradação da termoclina (front smearing) governada pela condução e pela dispersão térmica axial.

Estas fronteiras de desempenho físico foram subsequentemente integradas num modelo de otimização económica desenvolvido em MATLAB. A análise técnico-económica revelou uma relação crítica entre a geometria do reservatório e a potência consumida pelos ventiladores. Ao implementar uma arquitetura modular otimizada constituída por múltiplas unidades em paralelo e limitando o comprimento máximo do domínio poroso a 5 m, a resistência do fluido foi minimizada com sucesso, garantindo um consumo reduzido de eletricidade auxiliar. Sob estas condições otimizadas de unidades múltiplas, o sistema atingiu um Custo Nivelado de Armazenamento (LCOS) altamente competitivo de 6.10 USD/MWh_e para uma instalação à escala da rede com capacidade de 100 MWh_{th}. Estes indicadores demonstram que sistemas de leitos compactados de escória EAF operam a uma fração do custo das baterias químicas ou de sistemas de armazenamento de longo prazo de hidrogénio.

Em suma, este trabalho valida que a revalorização de resíduos industriais associada à otimização geométrica oferece uma alternativa viável e baseada na economia circular para a estabilização de redes elétricas a custos reduzidos e para a recuperação de calor industrial.

Palavras-chave: Armazenamento de Energia Térmica (TES) • Leito compactado • Escória de Forno de Arco Elétrico (EAF) • Método dos Elementos Finitos (FEM) • Análise Técnico-Económica • Custo Nivelado de Armazenamento (LCOS)

The United Nations Sustainable Development Goals

The United Nations Sustainable Development Goalss (SDGs) provide a global framework for achieving a better and more sustainable future for all. It includes 17 goals (https://sdgs.un.org/goals) to address the world's most pressing challenges, including poverty, inequality, climate change, environmental degradation, peace, and justice.

Integrating high-temperature packed-bed thermal energy storage systems with industrial waste materials, such as iron and steel slags, directly aligns with the United Nations Sustainable Development Goals (SDGs) embraced by the European Union's green transition framework. By bridging industrial waste revalorization with clean energy infrastructure, this approach aligns with the following Sustainable Development Goals:

SDG 7 Ensure access to affordable, reliable, sustainable and modern energy for all

SDG 9 Industry, Innovation, and Infrastructure

SDG 12 Ensure sustainable consumption and production patterns

SDG	Target	Contribution	Performance Indicators and Metrics
7	7.2	The proposed Electric Arc furnace (EAF) slag-based Sensible Heat Thermal Energy Storage (SHTES) system contributes to increasing renewable energy integration by enabling the storage of excess renewable electricity as high-temperature thermal energy. This allows the decoupling of renewable energy production from energy demand, improving the flexibility and reliability of renewable-based energy systems.	By 2030, increase substantially the share of renewable energy in the global energy mix
9	9.4	The implementation of EAF slag-based packed-bed Thermal Energy Storage (TES) supports the modernization and decarbonization of energy-intensive industries by providing a high-temperature heat storage solution capable of supplying industrial thermal processes with renewable or recovered energy.	By 2030, upgrade infrastructure and retrofit industries to make them sustainable, with increased resource-use efficiency and greater adoption of clean and environmentally sound technologies and industrial processes, with all countries taking action in accordance with their respective capabilities
12	12.4	The valorization of EAF slag as a TES material promotes the sustainable management of steelmaking byproducts by converting an industrial waste into a useful energy storage resource, reducing the environmental impacts associated with waste disposal and the extraction of conventional storage materials.	By 2020, achieve the environmentally sound management of chemicals and all wastes throughout their life cycle, in accordance with agreed international frameworks, and significantly reduce their release to air, water and soil in order to minimize their adverse impacts on human health and the environment
	12.5	The use of EAF slag in packed-bed TES systems contributes to waste reduction and circular economy principles by reusing an abundant industrial byproduct as an alternative to naturally extracted storage materials, extending its value beyond the steel production process.	By 2030, substantially reduce waste generation through prevention, reduction, recycling and reuse

Acknowledgements

First and foremost, I would like to express my sincere gratitude to my supervisor at FEUP, Professor Vítor Leal, and to my supervisor at DTU, Professor Ming Chen, for their availability, dedication, and valuable guidance throughout the entire duration of this project. I would also like to thank FEUP and DTU for providing me with the opportunity to develop my master's thesis in collaboration with researchers at DTU through an ERASMUS+ Internship Agreement. I am truly grateful for the knowledge and experience gained during this period, which I will carry with me throughout my professional career.

In addition, I would like to thank Dr. Akhil Panicker at DTU for his unwavering guidance and support. Without his advice and suggestions, I would not have been able to carry out the simulations and complete the project.

I would also like to thank my whole family for their unconditional support at all times. To my mother and father, I would like to thank them for being examples of strength and resilience, and for always believing in me. To my sisters, Clara and Laura, I am also deeply grateful for their constant understanding and for reinforcing my confidence during the most challenging moments of this journey.

Furthermore, I would like to thank my friends from high school, Kika, Joana, Bia, Mansilha and Lia, who have helped me smile even at the least good moments of life and have always been there for me. I would also like to thank my friend Luísa for her support and valuable friendship. I am very lucky to have all of you in my life.

I would also like to thank my university friends, Rodrigues, Curinha, Inês, Diego and Chico, for making this academic journey go by so quickly and always full of joy. To my "afilhados" in Coimbra, Maria, Rita and Jorge, I would also like to thank you for all your support and friendship. It has been a pleasure to accompany you in your academic journey and I am very proud of you. Finally, I would like to thank Diogo for always believing in me and for his contagious optimism, which were decisive to my success and to the conclusion of this project.

I would also like to thank the friends I made at DTU. To my friend Leonor, I would like to thank her for making me feel more at home and for all the funny moments during this journey. To my friends Viviana and Marta, I would like to thank you for the great moments we shared together always filled with laugher and companionship. At last, to my friends at DTU Choir, I would like to thank you for the light and jolly evenings after days of hard work, and for the amazing performances I had the opportunity to experience together.

Mariana Dias

"Nothing in life is to be feared, it is only to be understood"

Marie Curie

Contents

1 Introduction **1**
- 1.1 Motivation . . . 1
- 1.2 Objectives and research questions . . . 4
- 1.3 Methodology . . . 4
- 1.4 Dissertation structure . . . 5

2 Literature Review **6**
- 2.1 Literature search methodology . . . 6
- 2.2 Overview of energy storage technologies . . . 7
- 2.3 Thermal Energy Storage . . . 10
- 2.4 Rock Bed Systems . . . 12
- 2.5 Industrial waste materials . . . 14
  - 2.5.1 Industrial waste revalorization . . . 14
  - 2.5.2 Iron and steel slag . . . 16
- 2.6 Summary . . . 19

3 Material Characterization **20**
- 3.1 Thermophysical Properties . . . 20
- 3.2 Chemical Stability . . . 21

4 Numerical Model Development **31**
- 4.1 Geometry definition . . . 31
- 4.2 Material properties definition . . . 34
- 4.3 Physics interfaces definition . . . 36
  - 4.3.1 Free and porous media flow, Brinkman . . . 37
  - 4.3.2 Heat transfer in solids and fluids . . . 38
  - 4.3.3 Non-isothermal Flow . . . 38
- 4.4 Mesh generation . . . 39
- 4.5 Solver configuration . . . 41
- 4.6 Thermal performance indicators . . . 42
- 4.7 Limitations of the numerical model . . . 44

5 Simulation Cases Results and Discussion **46**
- 5.1 Comparison of the results obtained with different geometries . . . 46
- 5.2 Influence of inlet conditions in the performance of the packed-bed . . . 51
- 5.3 Evolution of the temperature contours in the packed-bed during resting phase . . . 55

6 Techno-Economical Analysis **58**
6.1 Model formulation and assumptions 58
6.2 Techno-economic results 64
6.3 Limitations of the Techno-Economic Analysis (TEA) 78

7 Conclusions and Future Work **80**
7.1 Conclusions 80
7.2 Future work 82

References **83**

Appendix A MATLAB code **88**

Appendix B Results from the TEA analysis **100**

List of Figures

1.1 Annual variability of electricity generation from renewable energy sources and consumption in six European countries [4]. . . . 2
1.2 Mismatch between electricity generation and demand in California on the 30th of April of 2024 [5]. . . . 2
1.3 Global energy storage capacity trends for electricity and Compound Annual Growth Rate (CAGR), according to a Wood Mackenzie 2020 report [6]. . . . 3
1.4 Multi-stage methodology followed in this study. . . . 5

2.1 Research Methodology. . . . 7
2.2 Available energy storage technologies, adapted from [11]. . . . 8
2.3 Schematic diagram of a packed bed thermal storage system during the discharge phase. . . . 13
2.4 Main solid co-products per steelmaking route (average outputs in kg/tonne crude steel) [9]. . . . 16
2.5 Graphical representation of the utilization of steel slag, adapted from [28]. . . . 17

3.1 Phase diagram of the CaO-FeO system at atmospheric pressure. . . . 22
3.2 Phase diagram of the SiO_2-CaO system at atmospheric pressure. . . . 23
3.3 Phase diagram of the SiO_2-FeO system at atmospheric pressure. . . . 23
3.4 Phase diagram of the FeO-Al_2O_3 system at atmospheric pressure. . . . 24
3.5 Phase diagram of the CaO-Al_2O_3 system at atmospheric pressure. . . . 24
3.6 Phase diagram of the SiO_2-Al_2O_3 system at atmospheric pressure. . . . 25
3.7 Ternary phase diagram of the SiO_2-CaO-Fe_2O_3 system, adapted from [45]. . . . 26
3.8 Ternary phase diagram of the SiO_2-CaO-Al_2O_3 system, adapted from [46]. . . . 27
3.9 Specific heat capacity evolution with temperature of the EAF slag considered in the study. . . . 28
3.10 Multiple phases diagram of the EAF slag considered in the study. . . . 29

4.1 Geometric model of the packed bed system with annotated dimensions. . . . 32
4.2 Components of the geometric model of the packed-bed system. . . . 32
4.3 Second geometric model of the packed bed system. . . . 33
4.4 Third geometric model of the packed bed system. . . . 34
4.5 Dynamic viscosity and density functions of air. . . . 35
4.6 Thermal conductivity and specific heat capacity functions of air. . . . 35
4.7 Influence of mesh size on the temperature profile at Point 5. . . . 40
4.8 Associated error with each mesh size for Point 1. . . . 40
4.9 Associated error with each mesh size for Point 9. . . . 40
4.10 Fine mesh used in the simulations using the third geometric model. . . . 41

5.1 Temperature contours (K) and velocity field streamlines (m/s) obtained with the three geometric models after 10 hours of charging, for an inlet air flow rate of 1200 L/min at 890 K. . . . 47
5.2 Temperature contours (K) and velocity field streamlines (m/s) obtained with the three geometric models after 20 hours of charging, for an inlet air flow rate of 1200 L/min at 890 K. . . . 47
5.3 Comparison of the heat storage capacity (kWh) throughout time (h) for the three geometries tested. . . . 48
5.4 Temperature contours (K) and velocity field streamlines (m/s) obtained with the three versions of the third geometry after 10h (left side) and 20h of charging (right side). . . . 49
5.5 Comparison of the heat storage capacity (kWh_{th}) throughout time (h) for the five geometries tested. . . . 50
5.6 Nine auxiliary points positioned across the packed-bed. . . . 51
5.7 Temperature in points 1, 5 and 9 during charging for Case 1. . . . 52
5.8 Temperature in points 1, 5 and 9 during charging for Case 2. . . . 52
5.9 Temperature in points 1, 5 and 9 during charging for Case 3. . . . 52
5.10 Temperature in points 1, 5 and 9 during charging for Case 4. . . . 52
5.11 Pressure contours for the four charging cases considered. . . . 54
5.12 Temperature contours (K) during resting period after 1, 2, 5, 8 and 10 hours of charging. . . . 55
5.13 Evolution of temperature (K) in 9 different points of the packed-bed during resting period. . . . 56

6.1 Levelized Cost of Storage (LCOS) (USD/MWh_e) evolution with the energy storage capacity (MWh_{th}) for different TES materials using the first approach for cross-sectional area calculation. . . . 64
6.2 LCOS (USD/MWh_e) evolution with the energy storage capacity (MWh_{th}) for different TES materials using the second approach for cross-sectional area calculation. 65
6.3 Electric fan power consumption (kWh_e) evolution with the energy storage capacity (MWh_{th}) for the first and third approaches. . . . 67
6.4 Yearly Operation and Maintenance Costs (OPEX) (Thousands of USD) evolution with the energy storage capacity (MWh_{th}) for the first and third approaches. . . . 68
6.5 Capital Expenditure (CAPEX) (Thousands of USD) evolution with the energy storage capacity (MWh_{th}) for the first and third approaches. . . . 68
6.6 LCOS (USD/MWh_e) evolution with the energy storage capacity (MWh_{th}) for the first and third approaches. . . . 69
6.7 LCOS (USD/MWh_e) evolution with the energy storage capacity (MWh_{th}) for different TES materials using multiple TES units and limiting the length of the porous domain to 2 m. . . . 70
6.8 LCOS (USD/MWh_e) evolution with the energy storage capacity (MWh_{th}) for different TES materials using multiple TES units and limiting the length of the porous domain to 5 m. . . . 71
6.9 LCOS (USD/MWh_e) evolution with the energy storage capacity (MWh_{th}) for different TES materials using multiple TES units and limiting the length of the porous domain to 10 m. . . . 71
6.10 LCOS (USD/MWh_e) evolution with the packing fraction of the porous domain. . 73
6.11 OPEX (mil. USD) evolution with the packing fraction of the porous domain. . . 73
6.12 LCOS (USD/MWh_e) variation with the electricity cost (USD/kW_{el}). . . . 74

6.13 OPEX (million USD) variation with the electricity cost (USD/kW$_{el}$). 75
6.14 Net Present Value (NPV) (million USD) variation with the increase relative to the base production cost LCOS (%). 76

List of Tables

2.1 Energy storage technology comparison table, adapted from [13] 9
2.2 Ferrous slag families classification and technology treatment, adapted from [8] . 18
2.3 Thermo-physical properties of EAF Slag and different usual heat storage materials [33] 18

3.1 Thermophysical properties of various rock bed materials 20
3.2 Chemical composition of steel slag (%), adapted from [41] 21
3.3 Composition of the EAF slag used in this study [40] 25

4.1 Properties of the materials used in the model 36
4.2 Specification parameters of each of the tested mesh sizes 39

5.1 Heat Stored after 5, 10, 15 and 20 hours of charging for different geometries tested 48
5.2 Flow rates employed for each simulation case 51
5.3 Coordinates of the auxiliary points 52
5.4 Comparison of the pressure drop obtained from the numerical simulations and through the Ergun equation for each charging case 54
5.5 Maximum and average standard deviation verified in each point. 56

6.1 Unitary cost of the materials used in the TEA 59
6.2 Superwool, vermiculite and steel ratios with the volume of TES and their density (kg/m^3) 60
6.3 Technical parameters obtained for the TES system using EAF slag 76
6.4 Economical parameters obtained for the TES system using EAF slag 77

B.1 Results obtained using one single TES unit and scaling all the dimensions of the porous domain. 100
B.2 Results obtained using one single TES unit and fixing the cross-sectional area of the porous domain to 20 m^2. 101
B.3 Results obtained using multiple TES units and fixing a maximum length of the porous domain in each unit to 2 m. 101
B.4 Results obtained using multiple TES units and fixing a maximum length of the porous domain in each unit to 5 m. 101
B.5 Results obtained using multiple TES units and fixing a maximum length of the porous domain in each unit to 10 m. 102

List of Acronyms and Abbreviations

ABS Air-cooled Blast furnace Slag
ACW Asbestos Containing Wastes
BF Blast furnace
BOF Basic Oxygen furnace
BOS Basic Oxygen furnace Slag
CAES Compressed Air Energy Storage
CAGR Compound Annual Growth Rate
CAPEX Capital Expenditure
CSP Concentrated Solar Power
EAF Electric Arc furnace
EAF C Electric Arc furnace Slag for Carbon Steel
EAF S Electric Arc furnace Slag for Stainless Steel
FEM Finite Element Method
GBS Granulated Blast furnace Slag
GHG Greenhouse Gas
HTF Heat Transfer Fluid
HTTES High Temperature Thermal Energy Storage
HVAC Heating Ventilation and Air Conditioning
LAB Lead Acid Battery
LCOE Levelized Cost of Electricity
LCOS Levelized Cost of Storage
LHTES Latent Heat Thermal Energy Storage
LIB Lithium Ion Battery
MSWI Municipal Solid Waste Incinerators
NPV Net Present Value
OPEX Operation and Maintenance Costs
ORC Organic Rankine Cycle
PCM Phase Change Material
PDE Partial Differential Equation
PEM Proton Exchange Membrane

PHES Pumped Hydro Energy Storage

RES Renewable Energy Sources

RFB Redox Flow Battery

SCM Supplemental Cementitious Materials

SDG Sustainable Development Goals

SHTES Sensible Heat Thermal Energy Storage

SMS Steelmaking slag

SSB Sodium Sulfur Battery

TCES Thermo Chemical Energy Storage

TCP Tricresyl Phosphate

TEA Techno-Economic Analysis

TES Thermal Energy Storage

List of Symbols

Symbols	
$A_{foundation}$	Area of the foundation of each TES unit [m^2]
A_s	External surface area [m^2]
a_r	Extent of conversion
C_p	Specific heat capacity of the TES material [J/(kg·K)]
C_{p_f}	Specific heat capacity of the HTF [J/(kg·K)]
c_{el}	Electricity cost [USD/kWh_{el}]
c_i	Unitary cost of each material i that is part of the system [USD/m^3]
D_p	Pebble diameter [m]
d_z	Thickness (or scaling factor in the z-direction)
E_{NET}	Net electricity output recoverable from the TES unit in each cycle
$E_{pump_{ch}}$	Electric fan power required during charging [kWhe]
$E_{pump_{disch}}$	Electric fan power required during discharging [kWhe]
E_{TES}	Energy storage capacity of the TES system [J]
$E_{TES_{out}}$	Direct thermal energy output from the TES unit [J]
F	External forces applied on the porous medium [N]
G_{ch}	Mass flow rate of the HTF per unit cross-section area during charge [kg/(m^2·s)]
G_{disch}	Mass flow rate of the HTF per unit cross-section area during discharge [kg/(m^2·s)]
h_{in}	Inside convection heat transfer coefficient [W/m^2·K]
h_{out}	Outside convection heat transfer coefficient [W/m^2·K]
I	Identity matrix
k	Thermal Conductivity of the TES material [W/(m·K)]
k_i	Thermal conductivity of the insulation layer i [W/(m·K)]
L	Length of the porous domain [m]
L_{new}	New length of the porous medium calculated from the obtained volume of storage [m]
L_{orig}	Length of the porous domain taken from the COMSOL model [m]
m	Mass of the TES material [kg]
$\dot{m_{ch}}$	Mass flow rate of the HTF during charge [kg/s]
$\dot{m_{disch}}$	Mass flow rate of the HTF during discharge [kg/s]
$\dot{m}_f$	Mass flow rate of the HTF [kg/s]
N_{TES}	Number of TES units
N_{op}	TES operational life [years]
p	Pressure [Pa]
p_A	Absolute pressure [Pa]

Q	Volumetric heat source [W/m^3]
Q_m	Mass source or sink [kg/(m^3·s)]
$Q_{lost,charge}$	Heat lost during the charging process [J]
$Q_{lost,discharge}$	Heat lost during the discharging process [J]
$Q_{lost,rest}$	Heat lost during the resting process [J]
Q_p	Heating (or cooling) due to pressure changes [W/m^3]
Q_{porous}	Porous medium losses [W/m^3]
$Q_{recoverd,fluid}$	Energy recovered by the HTF during discharging [J]
$Q_{released,bed}$	Energy released by the packed-bed during discharging [J]
$Q_{stored,bed}$	Heat stored by the porous medium [J]
$Q_{supplied,fluid}$	Heat supplied by the HTF during the charging process [J]
Q_{ted}	Thermoelastic damping heat source [W/m^3]
Q_{vd}	Viscous dissipation [W/m^3]
q	Heat flux vector [W/m^2]
q_{allow}	Allowable soil bearing pressure [kN/m^2]
q_0	External surface heat input [W/m^2]
r	Discount rate [%]
S_{new}	New side dimension of the porous domain calculated from the obtained volume of storage [m]
S_{orig}	Side dimension of the porous domain taken from the COMSOL model [m]
T	Absolute temperature [K]
T_{amb}	Reference or ambient temperature [K]
T_{bed}	Temperature of the bed [K]
$T_{in,ch}$	Constant high temperature of the air entering the bed during charging process [K]
$T_{in,disch}$	Temperature of the HTF entering the bed in the beginning of the discharging process [K]
$T_{initial}$	Initial temperature of the pebbles [K]
$T_{final,avg}$	Average final temperature of the pebbles [K]
$T_{out,dis}$	Temperature of the HTF leaving the bed during discharge [K]
t_{ch}	Charge phase duration [s]
t_{disch}	Disharge phase duration [s]
U	Overall heat transfer coefficient [W/(m^2·K)]
u	Velocity vector [m/s]
V_i	Volume of each material i that is part of the system [m^3]
$V_{storage}$	Volume of storage material [m^3]
$V_{storage_{orig}}$	Volume of the porous medium from the COMSOL model [m^3]
v	Velocity of the HTF [m/s]
v_{ch}	Superficial velocity of the fluid during charging [m/s]
v_{disch}	Superficial velocity of the fluid during discharging [m/s]

Greek symbols

α_p	Thermal expansion coefficient [K^{-1}]
β	Inertial coefficient
Δh	Phase change enthalpy [J/kg]
$\Delta h\|_{T_{min}}^{T_{max}}$	Maximum fluid enthalpy change [J/kg]
δH_r	Endothermic heat of reaction [J/kg]
δi	Thickness of the insulation layer i [m]

Δp_{ch}	Pressure drop induced by the TES unit during charge [Pa]
Δp_{disch}	Pressure drop induced by the TES unit during discharge [Pa]
ΔT	Temperature variation of the TES material [K]
η_{ch}	Efficiency of the charging process [%]
η_{compr}	Air circulator efficiency [%]
η_{cycle}	Efficiency of a typical Rankine cycle [%]
η_{disch}	Efficiency of the discharging process [%]
$\eta_{overall}$	Overall system efficiency [%]
κ	Permeability of the porous medium [m^2]
μ	Dynamic Viscosity of the HTF [Pa·s]
ρ	Density of the TES material [kg/m^3]
ρ_f	Density of the HTF [kg/m^3]
ρ_i	Density of each material i that is part of the system [kg/m^3]
τ	Viscous stress tensor [N/m^2]
ε_p	Porosity of the solid medium

Chapter 1

Introduction

The present study was developed within the framework of the MSc program in Mechanical Engineering at the Faculty of Engineering of Porto University (FEUP). This project was conducted using the research infrastructure of the Department of Energy Conversion and Storage at the Technical University of Denmark (DTU) in collaboration with supervisors from this department.

1.1 Motivation

The continuous growth of the global population and improvements in living standards have contributed to a significant increase in energy demand worldwide, highlighting the need for a transition towards low-carbon energy production systems [1]. In fact, achieving net-zero Greenhouse Gas (GHG) emissions by mid-century is considered essential for limiting global temperature rise to 1.5°C [2], in line with the objectives set forth by international climate agreements, such as the Paris Agreement.

To reach climate objectives, the integration of Renewable Energy Sources (RES) must be significantly accelerated. However, this shift poses a significant challenge, namely due to the temporal and spatial mismatch between electricity production and demand. This imbalance arises from the fluctuating nature of RES, such as wind, solar and geothermal power, and the varying electricity demand curve [3]. Figure 1.1 illustrates the annual variability of several renewable energy sources in six European countries, whereas Figure 1.2 highlights the differences between solar and wind energy generation and daily demand. Note that the red line in Figure 1.2, frequently called "duck curve", illustrates the electricity demand remaining after subtracting electricity supplied over the course of a day. Therefore, to sustain high shares of renewable electricity, energy systems must integrate solutions that manage fluctuations and keep the supply steady.

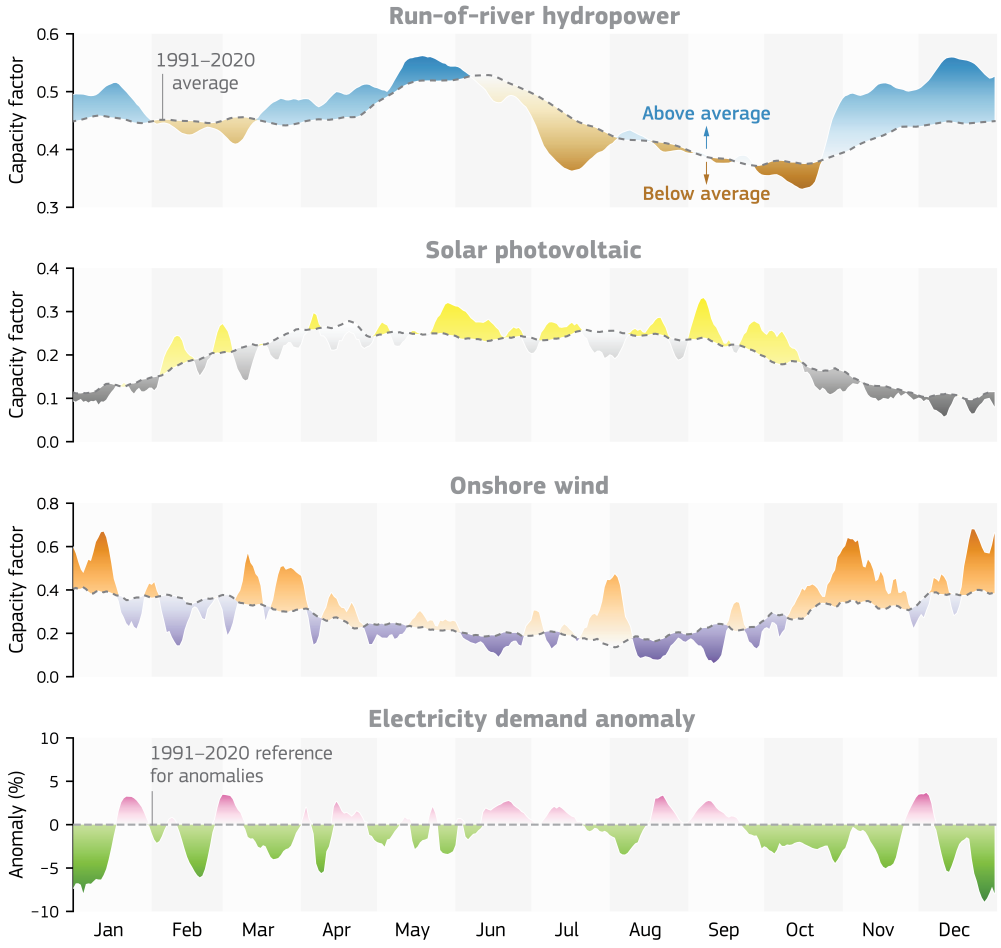

Figure 1.1: Annual variability of electricity generation from renewable energy sources and consumption in six European countries [4].

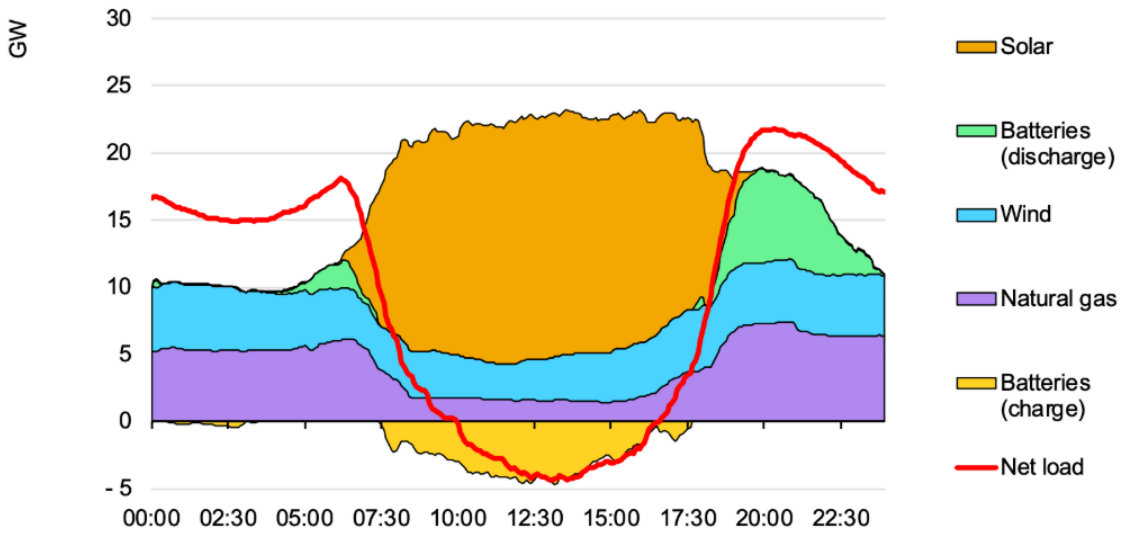

Figure 1.2: Mismatch between electricity generation and demand in California on the 30th of April of 2024 [5].

Energy storage technologies are key in this context. By storing surplus power and releasing it during periods of shortage, storage systems enhance grid flexibility, improve reliability, and reduce dependence on fossil-fuel backup plants. Consequently, energy storage will play a critical role in enabling high shares of renewable energy in future energy systems. The global energy storage capacity is therefore expected to grow significantly over the coming decades, as illustrated in Figure 1.3.

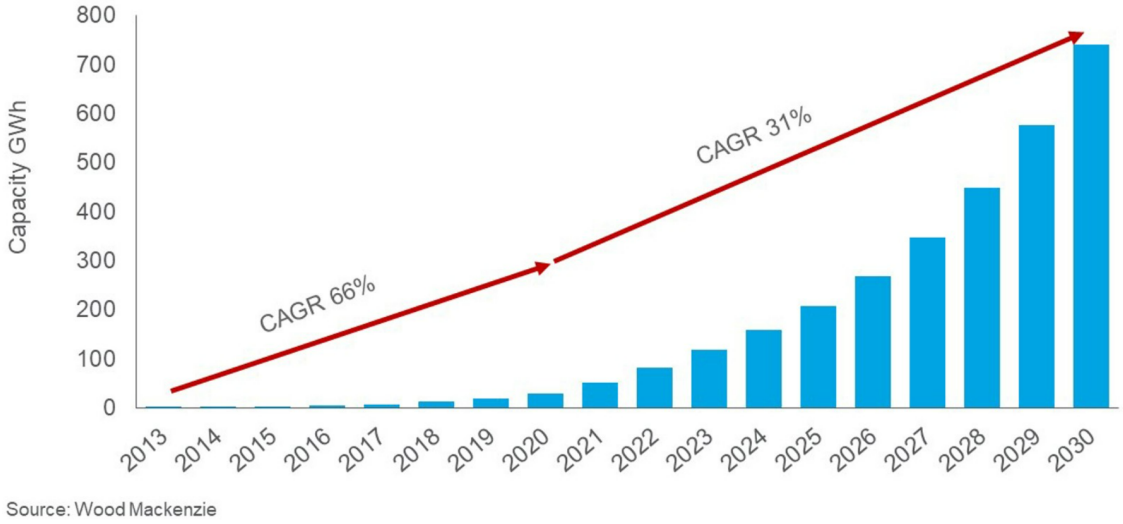

Figure 1.3: Global energy storage capacity trends for electricity and Compound Annual Growth Rate (CAGR), according to a Wood Mackenzie 2020 report [6].

Among the available energy storage options, Thermal Energy Storage (TES) has gained increasing attention due to its cost-effectiveness, scalability, and compatibility with high-temperature applications [7]. TES technologies can be categorized in three groups: Latent Heat Thermal Energy Storage (LHTES), Thermo Chemical Energy Storage (TCES) and Sensible Heat Thermal Energy Storage (SHTES).

Packed-bed TES systems are among the simplest and most cost-effective solutions. This system operates on the principle of sensible heat storage and operates using a bed of rock to store and release heat. This heat may be obtained either directly from high-temperature processes through heat recovery, or indirectly from heat sources powered by electricity, enabling the integration of electricity generated from renewable sources. The stored heat can be utilized across a broad temperature range, enabling applications such as steam generation in industries, district heating networks, and electricity production through integration with external power cycles. Their capability to operate over wide temperature ranges, combined with relatively fast thermal response times, makes these systems particularly attractive for enhancing grid flexibility and supporting energy-intensive industries, renewable energy integration, and power plant operation.

Through the years, a wide variety of potential heat storage materials have been identified, including water, molten salts, concrete, sand, rocks, and Phase Change Materials (PCMs) like paraffins or salt hydrates. Each particular application limits the suitable materials as a function

of the operation temperature range, storage capacity, power and other requirements [8]. However, the use of natural stones or virgin materials may raise sustainability and resource issues.

Industrial by-products such as iron and steel slag can be promising alternatives due to their high thermal stability, chemical resistance, wide availability, and potential to reduce industrial waste. In addition, according to a 2021 report from the World Steel Association [9], more than 400 million tonnes of iron and steel slag are generated annually worldwide, with production increasing alongside global steel demand. This industrial by-product represents approximately 200 kg Electric Arc furnace (EAF) and 400 kg (Blast furnace (BF)/Basic Oxygen furnace (BOF)) of co-products generated per tonne of steel produced. These include slag, dust, sludge, and other materials with significant portions often requiring landfill disposal.

In this context, the use of iron and steel slags as alternative TES materials presents a promising sustainable pathway well aligned with circular economy principles. As abundant industrial by-products, these materials can be revalorized into value-added applications, simultaneously mitigating waste generation and benefiting from their high availability and low cost.

1.2 Objectives and research questions

This project aims to explore the potential of using iron and steel slag as a sustainable medium for thermal energy storage. The focus of this study is the investigation of the thermal and chemical stability of slag, the characterization of its thermophysical properties, and the evaluation of its performance in a large-scale rock bed TES model. The study contributes to understanding how waste-derived materials can support circular economy goals in the energy sector. Key research questions to be addressed include:

1. Are iron and steel slag suitable and reliable sensible heat storage materials, from a thermophysical and chemical perspective?
2. How do iron and steel slag perform as storage media in a large-scale rock bed TES model?
3. How can geometry optimization of the packed-bed system enhance its performance and mitigate fan power requirements to minimize the Levelized Cost of Storage (LCOS)?
4. To which extent can these waste-derived materials support circular economy goals in the energy sector?

1.3 Methodology

This study followed a multi-stage methodology combining literature revision, material characterization, numerical modeling and a techno-economical analysis to evaluate the suitability of iron and steel slag as a TES medium. All the stages that integrated the methodology for this project are represented in the flux diagram illustrated in Figure 1.4.

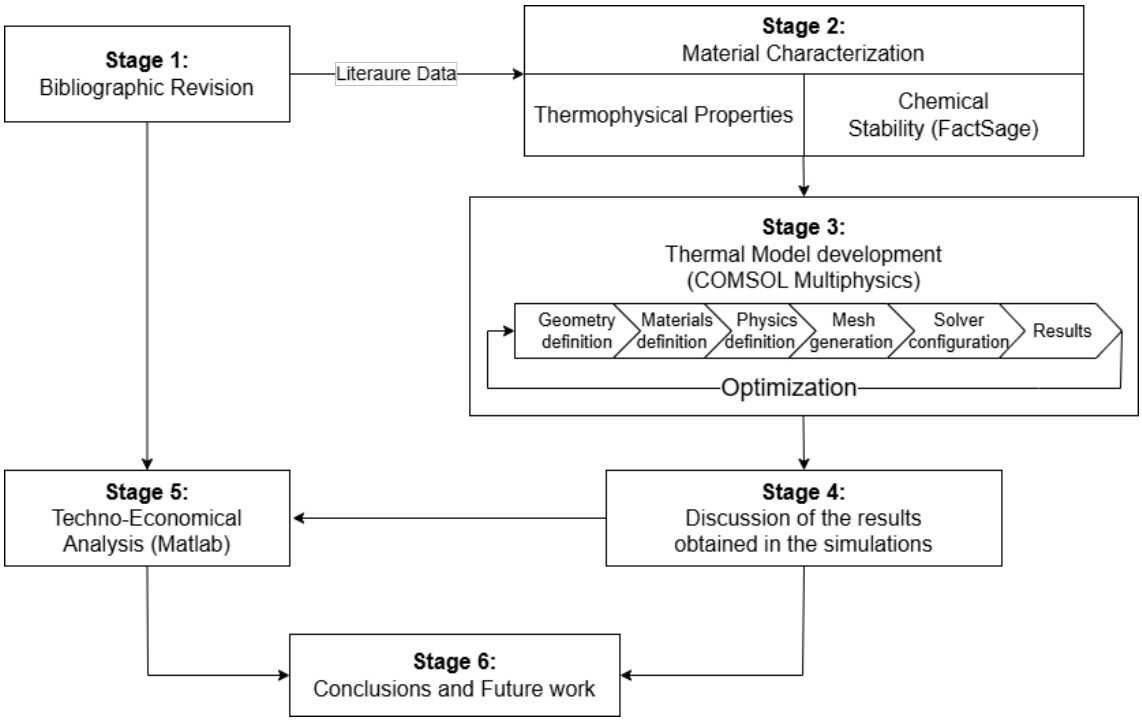

Figure 1.4: Multi-stage methodology followed in this study.

1.4 Dissertation structure

In addition to the introduction, the dissertation is structured into six additional chapters, which are briefly described below.

In Chapter 2, the state of the art is described and related work is presented. In particular, an overview of current energy storage technologies is presented, with a focus on SHTES and the rock bed systems. This chapter also highlights the great potential of industrial waste revalorization, in special, iron and steel slag.

Chapter 3 describes the methodology adopted for the characterization of the materials considered in this work, addressing both their thermophysical properties and chemical compatibility.

Chapter 4 outlines the methodology employed to develop the thermal model. This process encompasses geometry definition, material definition, implementation of the physics interfaces, mesh generation, simulation procedures, and definition of the performance evaluation parameters. To ensure an optimized system, an iterative approach was adopted, refining the geometry and model specifications to enhance overall thermal performance.

In Chapter 5, the results obtained in the numerical simulations are presented and discussed from a critical point of view.

Chapter 6 presents a comprehensive techno-economic assessment of the proposed technology, evaluating its potential integration into relevant applications.

Finally, Chapter 7 summarizes the key findings of this study and offers recommendations for future research.

Chapter 2

Literature Review

This section aims to provide an overview of the main global energy challenges and to highlight the great potential of TES systems to address these challenges. The research methodology adopted to conduct this review is also presented in a first instance.

2.1 Literature search methodology

The research process started with the analysis of the papers and theses from previous students that were made available by the supervisors at the host university. Additionally, other articles were searched on Google Scholar, using keywords such as "Thermal Energy Storage" and "Rock bed systems" and used, as selection criteria, being recent articles (from the last 10 years) and being highly cited papers. These articles were then added to a collection on Mendeley Reference Manager, where they were analyzed, and articles obtained using the snowball method [10] from articles already saved were added to this collection. Finally, Google Gemini (gemini.google.com) was also used to research articles related to more specific topics, in particular, to find materials' properties values in the literature to be used in the modeling process. Once a minimum number (n) of 10 articles, comprising both original research and critical reviews, where found, a solid foundation was established to elaborate the literature review chapter. The methodology followed in this work is summarized in the scheme of Figure 2.1.

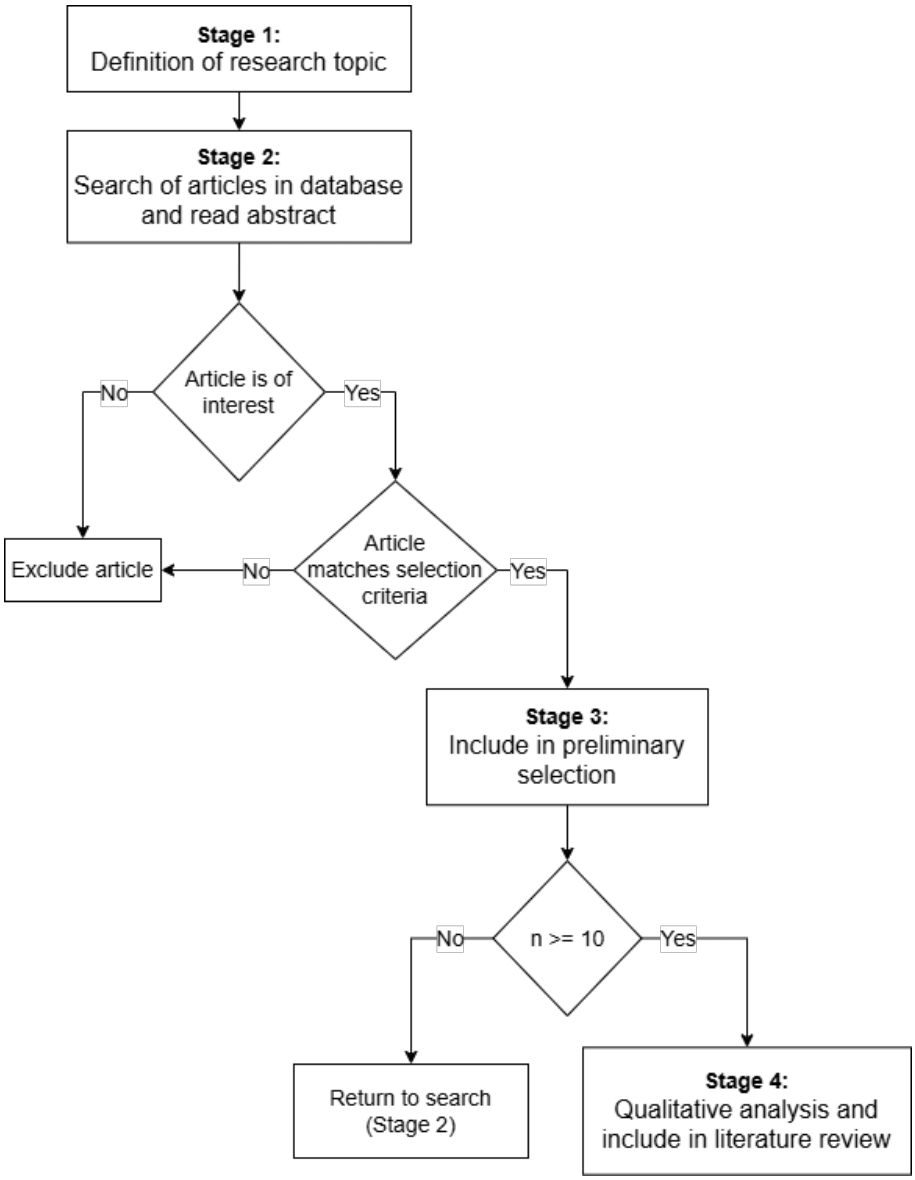

Figure 2.1: Research Methodology.

This research methodology thus enabled to find eleven review articles that presented complete overviews of existing TES technologies, as well as eleven original research articles that focused on the modeling of TES systems and on the comparison of computed results with experimental results.

2.2 Overview of energy storage technologies

Energy storage technologies play a critical role in enabling high renewable penetration. Over the centuries, a wide range of energy storage technologies has been developed to enable the preservation of energy for later use when demand arises. From early solutions, such as pumped hydropower

storage systems based on elevated reservoirs, to increasingly sophisticated systems, such as electrochemical batteries that have become an integral part of our modern life, various types of energy storage mechanisms have been designed to improve flexibility, reliability, and efficiency in energy supply. Figure 2.2 briefly summarizes the available energy storage technologies at present.

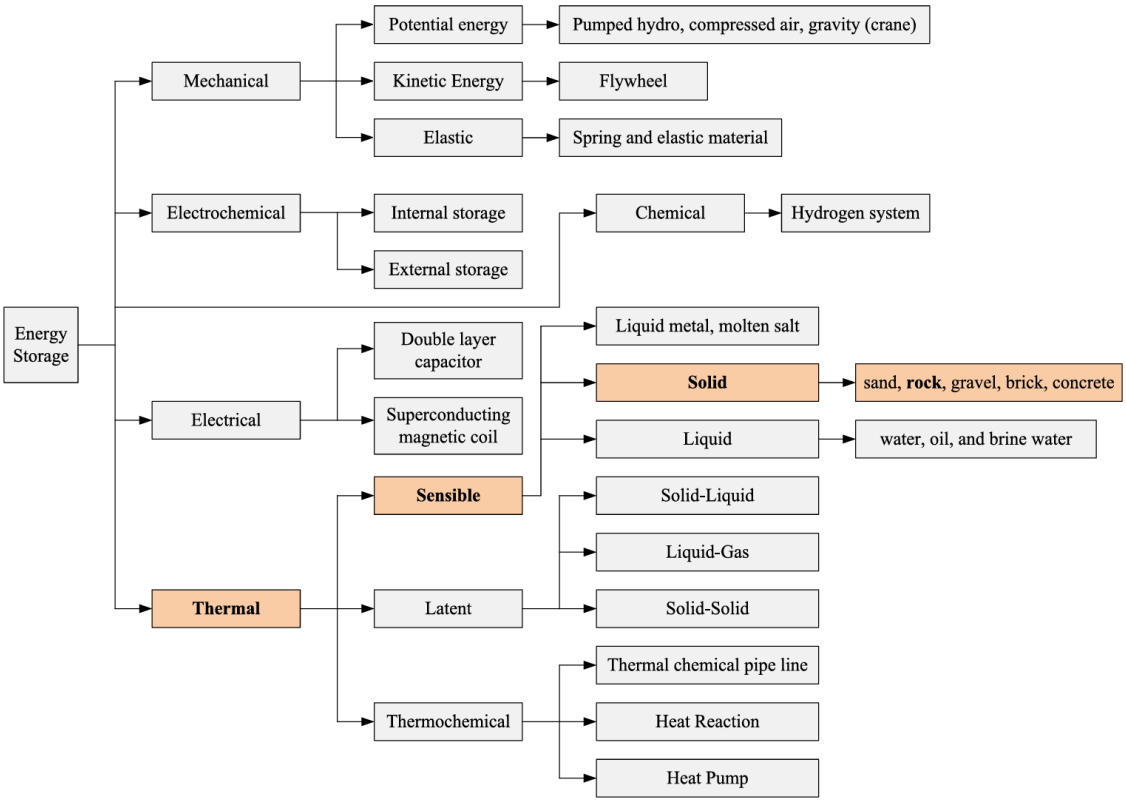

Figure 2.2: Available energy storage technologies, adapted from [11].

Addressing the temporal variability of energy generation and demand, ranging from hourly to seasonal scales, requires a portfolio of storage technologies with complementary characteristics.

Short-term storage solutions, such as lithium-ion batteries, offer high round-trip efficiencies but experience significant self-discharge losses when energy is stored over extended periods. In contrast, long-term storage technologies, including power-to-gas systems, exhibit minimal self-discharge over time but comparatively lower round-trip efficiencies [12]. Therefore, based on the time scale of the mismatch between energy generation and demand, different storage technologies are optimal to minimize energy losses, system costs, and GHG emissions, and maximize system reliability and supply security.

Among the technologies presented in Figure 2.2, electrochemical and TES are likely the most widely adopted technologies. Electrochemical technologies are typically used in consumer applications, whereas TES technologies are used to attend to industrial needs.

A comparison of the different energy storage technologies is summarized in Table 2.1.

Table 2.1: Energy storage technology comparison table, adapted from [13]

Storage Technique	**Power** $[MW]$	**Capacity** $[MWh]$	**Storage Period** $[time]$	**Specific Energy** $[kWh/ton]$	**Energy Density** $[kWh/m^3]$
Eletrochemical Storage					
Lithium Ion Battery (LIB)	0.001 - 0.1	0.25 - 25	Day - month	75 - 200	300
Sodium Sulfur Battery (SSB)	1 - 50	$\leq$ 300	Day	150	150 - 250
Lead Acid Battery (LAB)	0 - 40	0.25 - 50	Day - month	20	70
Redox Flow Battery (RFB)	0.03 - 7	< 10	Day - month	10 - 30	25 - 35
Mechanical Storage					
Compressed Air Energy Storage (CAES)	5 - 300	$\leq$ 250	Day	30 - 60	2 - 6 at 70 - 200 bar
Pumped Hydro Energy Storage (PHES)	< 3100	Small: $\leq$ 5000 Large: $\leq$ 140000	Day - month	0.28 at 100 m	0.28 at 100 m
Chemical Storage					
Hydrogen	Varies	Varies	Hour - month	33330	-
Methane	Varies	Varies	-	10000	-
Thermal Storage					
SHTES	0.001 - 10	-	Day - year	10 - 50	25
LHTES	0.001 - 1	-	Hour - week	50 - 150	100
TCES	0.01 - 1	-	Hour - week	120 - 250	120 - 250

Storage Technique	**Efficiency** $[\%]$	**Lifetime** $[\#cycles]$	**Power Cost** $[\$/kW]$	**Energy Cost** $[\$/kWh]$	**Maturity**
Eletrochemical Storage					
LIB	85 - 100	1000 - 4500	175 - 4000	500 - 2500	Commercialized
SSB	75 - 90	2500	1000 - 3000	300 - 500	Commercialized
LAB	70 - 90	500 - 1000	300 - 600	200 - 400	Mature
RFB	75 - 85	12000	600 - 1500	150 - 1000	Demo / early commercialized
Mechanical Storage					
CAES	60 - 79	8000 - 12000	1250 [1]	50 - 100	Demo / early commercialized
PHES	65 - 82	10000 - 30000	600 - 2000 [1]	80 - 200	Mature
Chemical Storage					
Hydrogen	20 - 50	-	-	6 - 20	Developing /demo
Methane	28 - 45	-	-	-	Developing
Thermal Storage					
SHTES	50 - 90	-	-	0.1 - 13 [2]	Commercialized
LHTES	75 - 90	-	-	10 - 56 [2]	Commercialized for some temperatures and materials
TCES	75 - 100	-	-	-	Developing / demo

[1] From 2014

[2] From 2013

2.3 Thermal Energy Storage

TES systems' functioning is based on three mechanisms: Charging, Storing and Discharging. It is important to highlight that these mechanisms may occur simultaneously. These mechanisms will be explained in detail for the particular case of rock beds in section 2.4. As can be observed in Figure 2.2, there are three types of TES technologies: sensible TES, latent TES, and thermo chemical TES. A brief analysis of these three TES technologies is provided in the following paragraphs.

Sensible Heat Thermal Energy Storage

Sensible Heat Thermal Energy Storage SHTES systems store thermal energy by using a temperature difference (higher or lower temperature, depending upon its application). During charging, storing and discharging, the temperature of the storage medium will be changed accordingly. During these processes, no phase change is involved. The storage capacity of SHTES systems is determined by the temperature difference and the specific heat capacity of the storage material, in accordance with Equation 2.1 [11]:

$$Q = mC_p\Delta T \tag{2.1}$$

where Q is the amount of heat stored in the storage material in J, m is the mass in kg, C_p is the specific heat capacity of the material in J/(kg·K), and ΔT is the temperature change in K.

Due to their simple storage mechanism and relatively low material costs, SHTES systems have been used for many applications, such as residential hot water systems and Heating Ventilation and Air Conditioning (HVAC), industrial waste heat recovery, and systems integrating Concentrated Solar Power (CSP). Common methods are insulated tanks and packed-beds, favored for their low cost and reliability [14].

A wide range of solid and liquid materials has been used for sensible heat storage, such as rock, sand, clay, brick, concrete soil, metal slags, water, and oil. Solid mediums have an advantage over liquids, namely, solid thermal storages have the benefit of allowing for more significant temperature fluctuations [14].

Water is widely utilized as a medium for sensible heat storage because of its high specific heat capacity, low cost, and widespread availability, particularly in low-temperature applications (below 100°C). Furthermore, water is non-toxic, non-flammable, and readily accessible, making it safe for use in systems associated with human environments. These properties render water especially suitable for TES in applications such as domestic hot water supply, refrigerated food preservation, and residential space heating [15].

For higher temperature applications (up to 600°C), molten salts are common and are particularly effective for CSP applications. However, commercial molten salts have disadvantages that impose limitations for exploiting their full potential: they have a limited operational temperature window, with high freezing points at around 225°C, which cause solidification risks in pipes and

require constant, energy-intensive heating; and stability up to 600°C. Furthermore, they can be corrosive, and their availability and costs are subject to the demand for fertilizers, their primary market [16].

On the other hand, solid materials like rocks, sand and industrial by-products are used as effective SHTES mediums, due to their wide availabitity, low-cost and sustainability advantages. Furthermore, these materials have the ability to hold higher temperatures than water and, in some cases, molten salts, and have relatively higher density, which makes them more suitable for storage involving high-temperature application, including heat supply for industrial processes [17] and electricity generation through the conversion of stored thermal energy into steam to drive turbines [18].

Latent Heat Thermal Energy Storage

Latent Heat Thermal Energy Storage LHTES systems absorb or release latent heat during isothermal phase change of the storage materials. The amount of energy stored in LHTES is generally higher than that of SHTES, since the magnitude of latent heat is generally higher than that of sensible heat. In LHTES, the solid–liquid phase change is the most popular option as its integration in TES is financially appealing.

Major advantages of this storage are its ability to store large amounts of energy at relatively constant temperature, and minimizing potential heat loss to the surroundings due to temperature difference which is experienced by SHTES systems [11]. The storage capacity of LHTES systems is strongly associated with the latent heat of phase change of the storage material, in accordance with Equation 2.2 [11]:

$$Q = m\Delta h \tag{2.2}$$

where m represents the mass (kg) and Δh is the phase change enthalpy (J/kg).

LHTES systems consist of three main components: a containment for the storage medium, a PCM as energy storage and a heat exchange surface to facilitate energy storage and withdrawal. Depending on the operating temperature of the TES, various PCMs with desired melting points and other characteristics can be chosen.

Low-temperature applications of LHTES systems include refrigeration and air conditioning, where PCMs such as paraffin wax or salt hydrates are commonly employed due to their favorable melting points and thermal properties. In contrast, high-temperature applications, such as CSP systems, typically employ molten salts or metal alloys that can withstand higher thermal loads and provide efficient energy storage [19]. Additionally, eutetic materials that customize mixtures of organic and/or inorganic compounds have been designed to achieve specific melting points [20], as well as other innovations, such as the integration of advanced materials and nanotechnology to enhance the thermal conductivity of PCMs, are being developed. Recent research also focuses on enhancing PCM performance through advanced material design, including the incorporation of

high-conductivity additives and nanomaterials to improve thermal conductivity and overall heat transfer characteristics [21].

Thermochemical Energy Storage

Thermochemical Energy Storage TCES systems use chemical reactions to store and provide energy. The charging mechanism consists of an endothermic reaction where a reactant A requires enthalpy of reaction ΔH_r to origin compounds B and C, as illustrated in Equation 2.3. During the discharging, the reverse reaction occurs where compounds B and C are recombined into reactant A by releasing the enthalpy reaction [11].

$$A + \Delta H_r \rightleftharpoons B + C \tag{2.3}$$

The heat stored in thermochemical heat storage is given by Equation 2.4:

$$Q = a_r \, m \, \delta H_r \tag{2.4}$$

where a_r is the extent of conversion, m is the mass of storage material (kg) and δH_r (J/kg) is the endothermic heat of reaction.

When compared to sensible heat and latent heat storage, thermochemical energy storage can yield five and ten times higher energy storage, respectively, and thermal losses can be minimized or even eliminated as products can be stored at room temperature. These characteristics make TCES systems particularly attractive for long-term storage of solar thermal energy. However, despite their theoretical advantages, thermochemical systems remain at a relatively early stage of technological development, with limited large-scale practical implementation to date. Consequently, further research and development are required to address existing technical and economic challenges [22].

In conclusion, each of the three thermal energy storage TES technologies presents distinct advantages and limitations. Nevertheless, their broad range of operating principles, temperature levels, and performance characteristics enables their adaptation to a wide variety of practical applications.

2.4 Rock Bed Systems

Packed-bed configurations are widely regarded as a robust solution for High Temperature Thermal Energy Storage (HTTES) due to their high heat transfer areas and the utilization of low-cost storage medium materials.

These systems operate by elevating the temperature of a Heat Transfer Fluid (HTF) through electrical-to-thermal conversion, subsequently storing the energy within a solid packed bed of natural rock or industrial by-products. Figure 2.3 illustrates the scheme of a packed-bed system

during the discharging phase. This system allows for the large-scale decoupling of energy generation and demand [3]. Studies have shown that rock bed storage systems can store energy at a thermal capacity of at least 450 kWh [3], with temperatures up to 600°C.

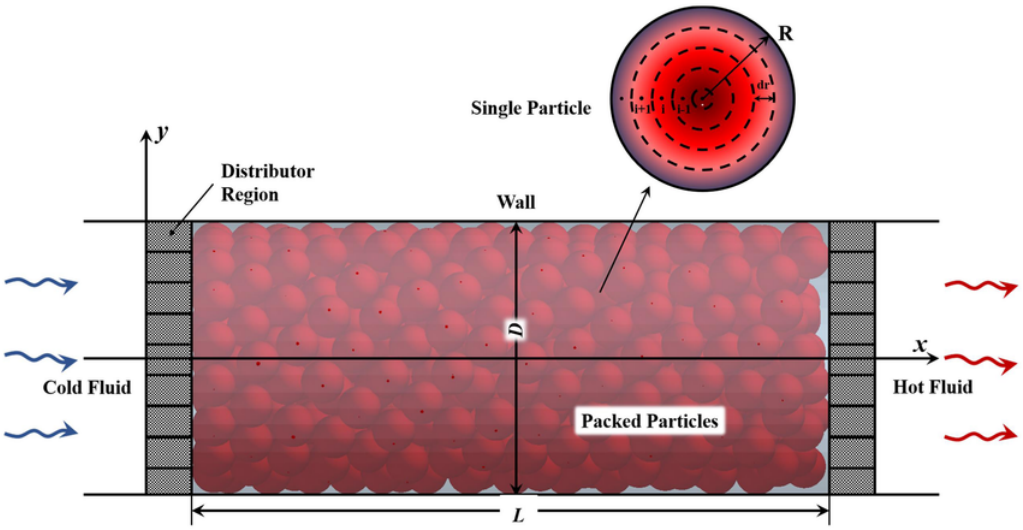

Figure 2.3: Schematic diagram of a packed bed thermal storage system during the discharge phase.

Rock bed TES systems offer several notable advantages. They are capable of operating over a wide temperature range and exhibit relatively fast thermal response times, making them suitable for applications relevant to grid balancing, energy-intensive industrial processes, renewable energy integration, and conventional power generation. In addition, contrary to storage technologies that rely on elevated topography or significant pressure differentials, rock bed TES systems do not impose specific geological requirements, thereby increasing their flexibility in site selection. Furthermore, they are generally more cost-effective than molten salt–based TES systems, mainly due to the use of inexpensive and widely available storage media. Their operation at pressures close to ambient conditions also reduces the need for complex sealing systems and heavy structural components, which can simplify system design and lower overall capital costs. On top of that, rock beds are characterized by a long cycle and calendar life-time due to minimal cycle-induced degradation of the storage material and they present no safety or environmental concerns [3].

On the other hand, rock bed TES systems also present some limitations, primarily associated with the lower volumetric heat capacity and thermal conductivity of air compared to those of thermo-oils, molten salts, sodium, or other HTFs [23]. Furthermore, the available literature about experimental data for rock bed HTTES systems is limited to laboratory and pilot-scale investigations, due to the large air flow and surface area required. Therefore, the economic feasibility of industrial-scale rock bed systems still needs to be evaluated [3]. Nevertheless, in contrast to electrochemical batteries, rock bed HTTES systems offer significant scaling potential, as charging and discharging power can be adjusted independently of the storage capacity.

The operating principle of a rock bed system comprises three main stages: charging, storage, and discharging. During the charging phase, high-temperature fluid, usually air, previously heated

by an electric heater or another suitable heating device, is introduced into the system through the inlet. Heat transfer from the fluid to the storage medium occurs predominantly by convection. As the hot fluid flows through the porous rock bed, a temperature gradient develops along the axial direction in the porous medium, with higher temperatures near the inlet and progressively lower temperatures toward the outlet.

Once the rock bed is fully charged, both the inlet and outlet are closed to minimize heat losses, as the primary objective is to preserve the stored thermal energy. The insulation layers surrounding the system further reduce thermal losses to the environment, thereby enhancing storage efficiency.

When energy recovery is required, the discharging phase begins. Cold fluid is introduced through the outlet side and flows in the opposite direction, absorbing the thermal energy stored in the rocks through convective heat transfer. As the fluid heats up while passing through the bed, it exits from the previously hotter end and can later be used for power generation or other energy conversion processes.

2.5 Industrial waste materials

Industry plays a fundamental role in modern society by generating employment, supporting economic growth, fostering technological innovation, and improving overall living standards. However, one downside to increased industrialization is the massive amount of waste it creates [24]. Industrial by-products include chemicals, metals, sludge, and other hazardous and non-hazardous waste materials, which can lead to environmental contamination, affecting air, water, and soil quality and posing risks to ecosystems and wildlife, if not properly managed.

In this way, the revalorization of industrial waste materials for high-value applications, such as their utilization in TES systems, represents a promising strategy to reduce environmental impacts while promoting a circular economy. Recycling and repurposing industrial by-products can reduce the demand for virgin raw materials, thereby limiting resource extraction and associated environmental impact. Furthermore, the utilization of industrial waste prevents it from being sent to landfills and often requires less energy than extracting and processing raw materials which, in turn, results in fewer overall GHG emissions [24].

Besides the many environmental benefits, reusing industrial waste and by-products can bring economical advantages. In particular, the utilization of industrial waste can reduce waste disposal fees for companies and energy consumption in the short term, while also enabling the generation of new income from the sale of recycled materials.

2.5.1 Industrial waste revalorization

Over the last few decades, a wide range of industrial waste and by-products has been studied and their potential for sensible heat storage has been evaluated, some of which are being produced to integrate commercial systems and achieve considerable benefits [8].

Asbestos Containing Wastes (ACW) wide availability, low cost and desirable thermo-physical and chemical properties make it a suitable material for SHTES applications. Asbestos is a group of

six naturally-occurring fibrous silicate minerals that have been widely used to produce materials resistant to fire, spun products, etc, because of its low thermal conductivity, high mechanical strength, resistance to chemical and biological attacks, and low cost [25]. However, they are toxic and can cause serious health diseases, including fibrosis and cancer [26]. Thus, the treatment and revalorization of these materials is a key issue. To convert asbestos containing-wastes into an inert material several processes are used and, in the end, melted ACW results in glass and ceramics. It has been observed that, for a temperature of 900 °C, the glass crystallizes to form ceramic made of Wollastonite ($Ca(Ca,Mn)Si_2O_6$), Akermanite ($Ca_2MgSi_2O_7$) and Augite ($Ca(Mg,Fe)Si_2O_6$) [8]. This new structure obtained is stable under repetitive cycles of heating and cooling from room temperature to 1000 °C, hence, it is clear that ACW are suitable for HTTES applications, in particular, in CSP plants [25].

Another alternative SHTES material are fly ashes. These are micron-sized particles present in gaseous effluents produced by industrial combustions such as coal fired power plants or Municipal Solid Waste Incinerators (MSWI). The fly ashes are collected by electrostatic filters from the industrial gas effluents and various technologies are available today for fly ash vitrification. According to a study that used plasma torch vitrification of MSWI Fly Ash [27], as SHTES materials, the glass form is relevant up to 600 °C, while the ceramic can be used up to 1100 °C. Their densities, thermal capacity, thermal conductivity, coefficient of thermal expansion and Young modulus fall within current ranges of values of refractory materials. Their major original advantages for being used as SHTES materials are their sustainable character, large availability, wide operational temperature range and low cost.

On the other hand, construction and demolition (C&D) waste materials, like concrete and bricks, can also be repurposed as raw materials for sensible heat storage. The accelerated urbanization and demand for new infrastructure construction over the past few decades have resulted in a considerable amount of construction materials being wasted at the construction site due to improper disposal. Therefore, developing C&D waste recycling strategies remains critical to achieve a more sustainable construction industry, which remains a major contributor to GHG emissions [28]. Furthermore, natural disasters, like earthquakes and hurricanes destroy many buildings and produce a large amount of waste that could be reused for noble ends.

In fact, conventional concrete provides one of the most economical options for SHTES materials due to its wide availability, relatively low cost, and large thermal mass per unit volume, which enables the storage of significant amounts of heat. However, it has a degradation in strength and a change in its microstructure beyond 500 °C, which limits the usage of concrete in TES applications that require higher operational temperature when compared with other solid media [29]. Nevertheless, the use of different formulations and the incorporation of additives, such as Supplemental Cementitious Materials (SCM), enables the material to maintain a higher strength and a better thermal resistance both during and after high temperature exposure, overcoming the previous drawback.

At the same time, demolished bricks, particularly ceramic and clay-based types, present a great potential for storage medium for TES as their production process involves high temperatures.

These are effective, low-cost, and durable materials for HTTES in industrial applications for high-temperature storage in steam generation and power plants [30]. In addition, clay bricks can be modified with additives like Tricresyl Phosphate (TCP) to improve thermo-mechanical properties or combined with PCMs to enhance heat capacity [31].

Finally, iron and steel slags have gained increasing attention as potential materials for sensible heat storage due to their large availability, low cost, and significant sustainability potential. In addition, these materials exhibit favorable chemical stability and thermophysical properties that make them suitable for thermal energy storage applications. Their characteristics and potential applications will be discussed in greater detail in the following section.

2.5.2 Iron and steel slag

Steel is a vital component of the modern world due to its exceptional durability, malleability, and recyclability, which make it widely used in several industrial areas. The main solid co-products produced during iron and steel production are slag (90% by mass), dust and sludge. Figure 2.4 was taken from a 2021 World Steel Association report and provides a general idea of the volume of each by-product generated to produce a tonne of steel.

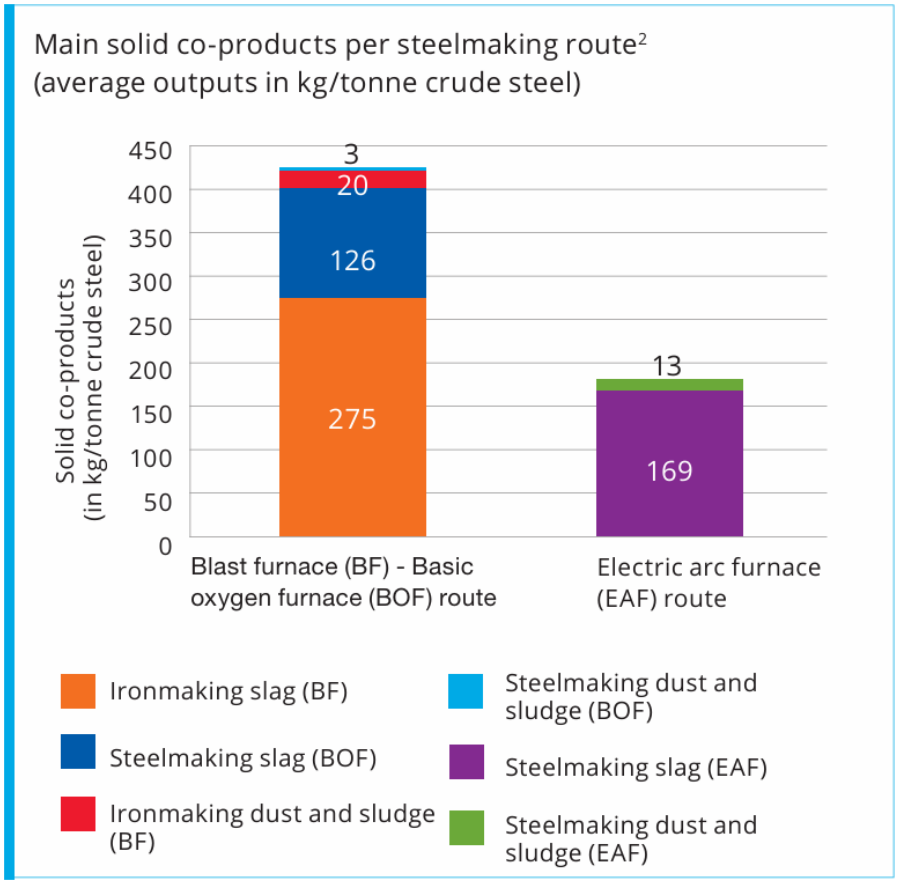

Figure 2.4: Main solid co-products per steelmaking route (average outputs in kg/tonne crude steel) [9].

According to [9], more than 400 million tonnes of iron and steel slag are produced annually worldwide. Slag is a mixture of silica, calcium oxide, magnesium oxide, and aluminium and iron oxides. Slag can also contain some heavy metals in its composition, which can be hazardous for health and the environment, if not treated properly. For this reason, dumping slag in landfills should not be considered as a long term solution for waste management. Currently, the world-wide average recovery rate for slag varies from over 80% for steelmaking slag to nearly 100% for ironmaking slag [9], while the European Union recycles roughly 92% of its steel slag [32]. Therefore, even though many countries are able to recover a great part of this by-product, a great effort still needs to be made to increase the recovery rate for slag to nearly 100% worldwide. Fig 2.5 illustrates the distribution of steel slag utilization across different sectors.

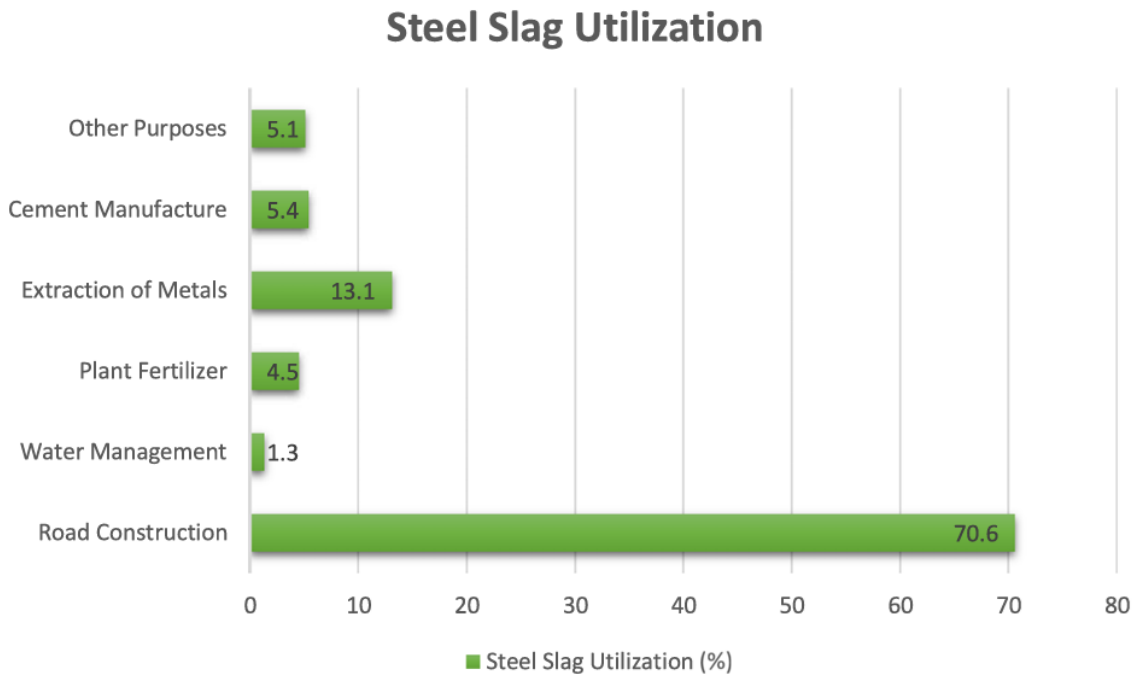

Figure 2.5: Graphical representation of the utilization of steel slag, adapted from [28].

Slags can be classified into families depending on their nature, and their treatment technologies will vary according to the slag family and to the posterior applications of this by-product. Table 2.2 summarizes the slag families according to the European Steel Association and their respective treatment technology.

Table 2.2: Ferrous slag families classification and technology treatment, adapted from [8]

Ferrous slag family	**From**	**Treatment technology**
Granulated Blast furnace Slag (GBS)	Production of iron by thermochemical reduction in a blast furnace	Rapid quenching of the molten slag with high pressure, high volume water sprays, grinding of the granulated slag to cement fineness
Air-cooled Blast furnace Slag (ABS)	-	Crushing and screening of the air cooled slag
Basic Oxygen furnace Slag (BOS)	Solidification of the steel in a basic oxygen furnace and generated by the addition of limestone and/or dolomite	Crushing and screening of the slag that has been air cooled and watered
Electric Arc furnace Slag for Carbon Steel (EAF C)	Melting of scrap in an electric arc furnace	Crushing and screening of the slag that has been air cooled and watered
Electric Arc furnace Slag for Stainless Steel (EAF S)	Melting of scrap in an electric arc furnace	Crushing and screening of the slag that has been air cooled and watered
Steelmaking slag (SMS)	Steel production process to the subsequent treatment of crude steel	-

The thermophysical properties of ferrous slag indicate that this material exhibits characteristics well suited for TES applications, according to the criteria established by the International Energy Agency, in particular, density, specific heat capacity and thermal conductivity. Table 2.3 highlights that the values obtained for steel slags are similar to other materials used in packed-beds for thermal heat storage.

Table 2.3: Thermo-physical properties of EAF Slag and different usual heat storage materials [33]

Property	EAF Slag 1	EAF Slag 2	Cofalit ®	HT Concrete	Alumina (99.5 %)
Density (kg/m^3)	3430	4110	3120	2750	3960
Specific Heat (J/kg K)	865	837	900	916	800
Thermal Condusctivity (W/mK)	1.47	1.51	1.5 - 2.0	1.0	18.0

In addition, iron and steel slags present high thermal stability up to 1200 °C, limited by the melting process of the material [8]. This makes iron and steel slags suitable for applications that require a high operation temperature, from CSP systems to industrial heat recovery. Particularly in CSP systems, the substitution of molten salts with this low-cost industrial by-product has the potential to significantly reduce the cost of thermal energy storage systems and, consequently, the overall cost of electricity production.

On the other hand, the major drawback of using steel and iron slag as TES material may be the compatibility between this material and the HTF or the container material. Nevertheless, positive results have been obtained. According to the results presented in [33], there is no corrosion in the EAF slags used in the study when working with air as HTF at temperatures up to 1000°C. In this

case, it can be said that there is compatibility between the EAF slags used as the porous medium and air as HTF in a rock bed system, which could therefore lead to the elimination of expensive heat exchangers [8].

Overall, the thermophysical and chemical properties of iron and steel slags, together with their associated environmental and economic advantages, highlight the strong potential of these waste materials for the development of efficient and cost-effective thermal energy storage solutions. However, even though interest in this industrial by-product as an alternative material for TES is growing in both research and industry [33], there are still few studies that have addressed experimentally or computationally use of EAF slag as TES inventory material. [34] presents the experimental testing of a 400 kWh_t packed-bed prototype using an Air Test Loop facility to validate the use of steel slag as a low-cost TES material and uses the results to successfully validate an accurate computational model developed in ANSYS Fuent. [35] investigated the suitability of slag pellets as a high-temperature thermal storage medium for CSP plants through experimental testing using a German Aerospace Center (DLR) test facility ("HOTREG") in Stuttgart and numerical modelling, yielding an agreement of over 90 %. In this way, its technological and economical viability has yet to be proven at a commercially relevant scale.

2.6 Summary

Overall, the use of iron and steel slag for TES presents an opportunity to address multiple challenges, including waste management, energy storage, circular economy and climate change.

Rock bed sensible thermal storage systems offer a simple and cost-effective solution for storing thermal energy. While they have limitations, their low material cost, availability, and high-temperature capability make them attractive for various applications.

Chapter 3

Material Characterization

3.1 Thermophysical Properties

To determine whether iron and steel slag are suitable and reliable sensible heat storage materials, one must analyze their key thermo-physical properties, in particular the density, specific heat capacity, and thermal conductivity. Knowing these properties, it is also possible to determine the volumetric heat capacity of the material. After determining the values of these properties for iron and steel slag, they can be compared with the corresponding values for conventional rock bed materials to assess whether they are consistent.

Following this logic, and taking into consideration the values of these properties available in the literature, it was possible to create a materials database containing the thermophysical properties of the rock bed materials of interest to use in this study, just as it is represented in Table 3.1. In this table, the most common packed-bed materials were included, as well as EAF slag, given its central role in this study.

Table 3.1: Thermophysical properties of various rock bed materials

Material	**Density, ρ [kg/m^3]**	**Specific Heat Capacity, C_p [J/(kg.K)]**	**Thermal Conductivity, k [W/(m.K)]**	**Volumetric Heat Capacity, ρC_p ($\times 10^6$) [kJ/(m^3·K)]**	**Reference**
MSWI Fly Ash	2940	1030	1.31	3.0282	[27]
Coal Bottom Ash	1400	650	1.4	0.91	[36]
Swedish Diabase	3007	900	2	2.7063	[37]
HT Concrete	2250	920	1.770	2.07	[38]
Common Brick	1922	837	0.721	1.6087	[39]
EAF Slag	3430	933	1.43	3.2002	[40]

The performance of sensible heat storage materials in packed bed systems is predominantly governed by their thermophysical properties, in particular density, specific heat capacity, and thermal conductivity. The energy storage capacity is directly proportional to the volumetric heat capacity (ρC_p), while the charging and discharging rates are influenced by thermal conductivity and

thermal diffusivity. An optimal material for the rock bed system should therefore exhibit a high volumetric heat capacity combined with sufficient thermal conductivity to ensure efficient heat transfer, although a trade-off exists between storage capacity and thermal responsiveness.

In this way, it is possible to formulate theoretical expectations regarding the behaviour of EAF slag in the TES model used in this study. From the observation of Table 3.1 it is possible to verify that EAF slag has a higher volumetric heat capacity in comparison with the materials listed in the table, which means that it is able to store more energy per unit volume than those materials. On the other hand, EAF slag has a lower thermal conductivity and, therefore, has a higher thermal resistance and takes more time to propagate heat in comparison with materials with a higher thermal conductivity, such as Swedish diabase and high temperature concrete.

3.2 Chemical Stability

To assess the chemical stability of iron and steel slag, it is first necessary to study its chemical composition. Although the composition of iron and steel slags can vary significantly depending on their origin and production process, they generally consist of similar constituent compounds. However, the relative proportions of these components may differ considerably between different slags. Table 3.2 lists the chemical composition ranges for different types of steel slag [41]. According to this table and to another literature reference [42], the steel slag mainly consists of SiO_2, CaO, Fe_2O_3, FeO, Al_2O_3, MgO, MnO and P_2O_5. Blast furnace (iron) slag is richer in silica and alumina, while steel slag (BOF/EAF) has much higher iron and free lime (CaO) content [43].

Table 3.2: Chemical composition of steel slag (%), adapted from [41]

Components	Basic oxygen furnace	Eletric arc furnace (carbon steel)	Eletric arc furnace (alloy/stainless)
SiO_2	8-20	9-20	24-32
Al_2O_3	1-6	2-9	3.0-7.5
FeO	10-35	15-30	1-6
CaO	30-55	35-60	39-45
MgO	5-15	5-15	8-15
MnO	2-8	3-8	0.4-2
TiO_2	0.4-2	N/A [3]	N/A [3]
S	0.05-0.15	0.08-0.2	0.1-0.3
P	0.2-2	0.01-0.25	0.01-0.07

[3] Not available

Once the general chemical composition of iron and steel slags is known, their chemical stability can be further evaluated. A practical approach consists of identifying the constituents present in a higher proportion in the slag and analysing the phase diagrams of the most relevant component

pairs. This analysis enables the identification of possible existing phases across the temperature range of interest and the evaluation of their stability under typical packed bed operating conditions, ranging from ambient temperature to approximately 600 °C.

Figures 3.1 to 3.6 illustrate the phase diagrams of the pairs of components CaO-FeO, SiO_2-CaO, FeO-SiO_2, FeO-Al_2O_3, CaO-Al_2O_3 and SiO_2-Al_2O_3, respectively, which include the most relevant components of steel slags according to [41]. These binary phase diagrams were plotted using the student version of FactSage chemical simulation software [44].

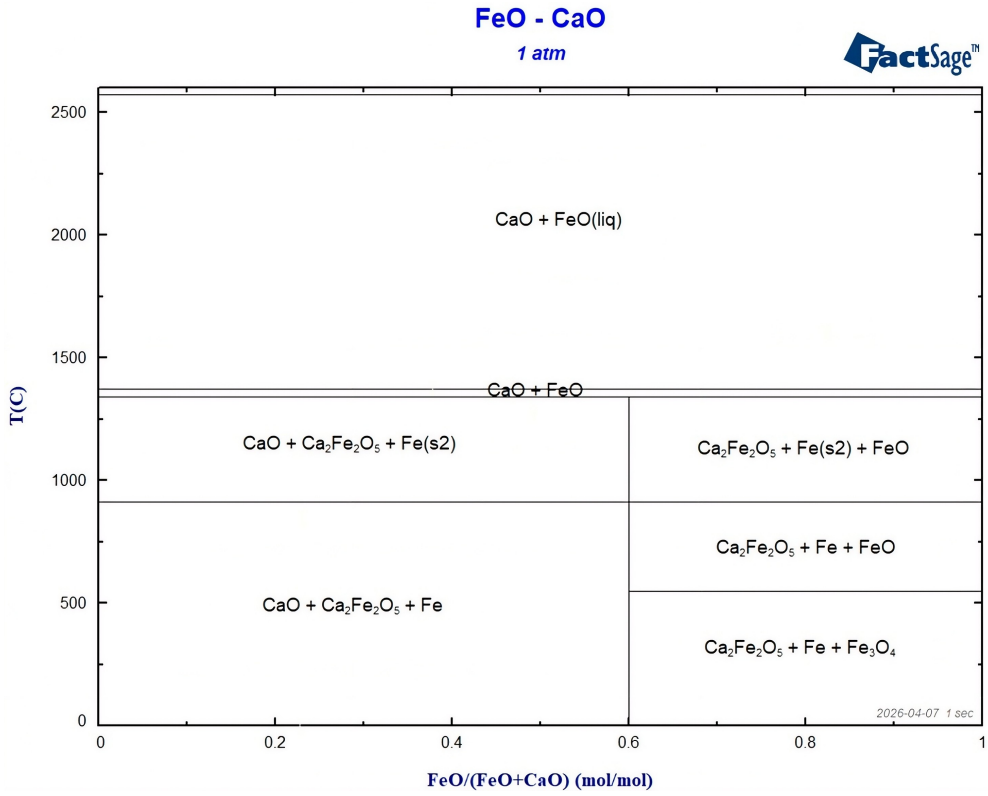

Figure 3.1: Phase diagram of the CaO-FeO system at atmospheric pressure.

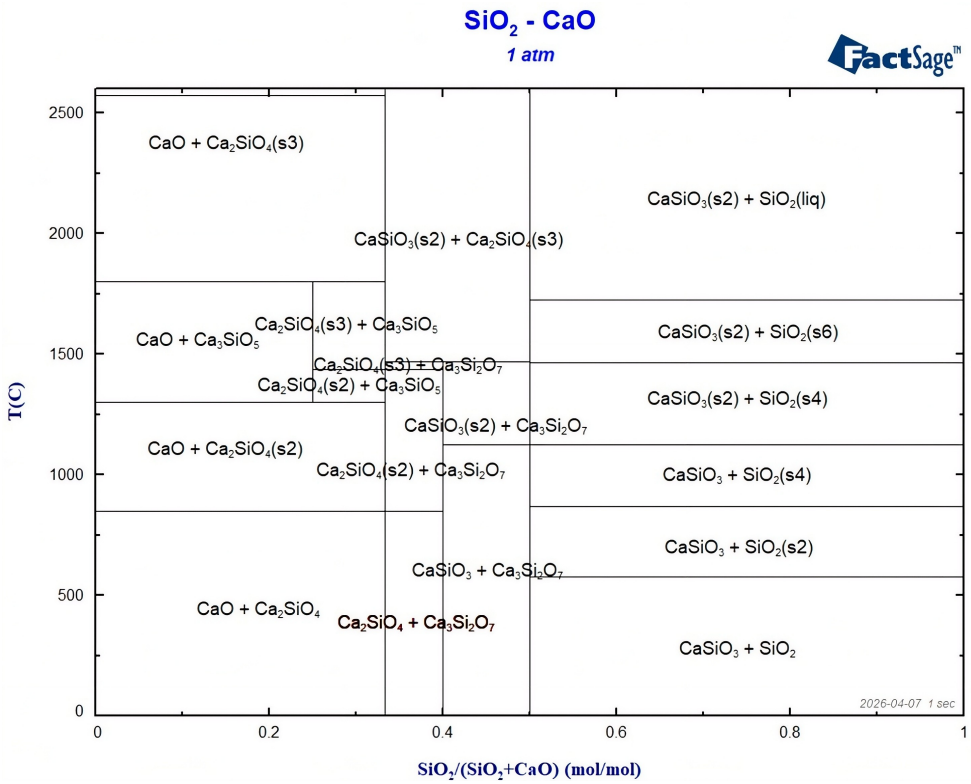

Figure 3.2: Phase diagram of the SiO_2-CaO system at atmospheric pressure.

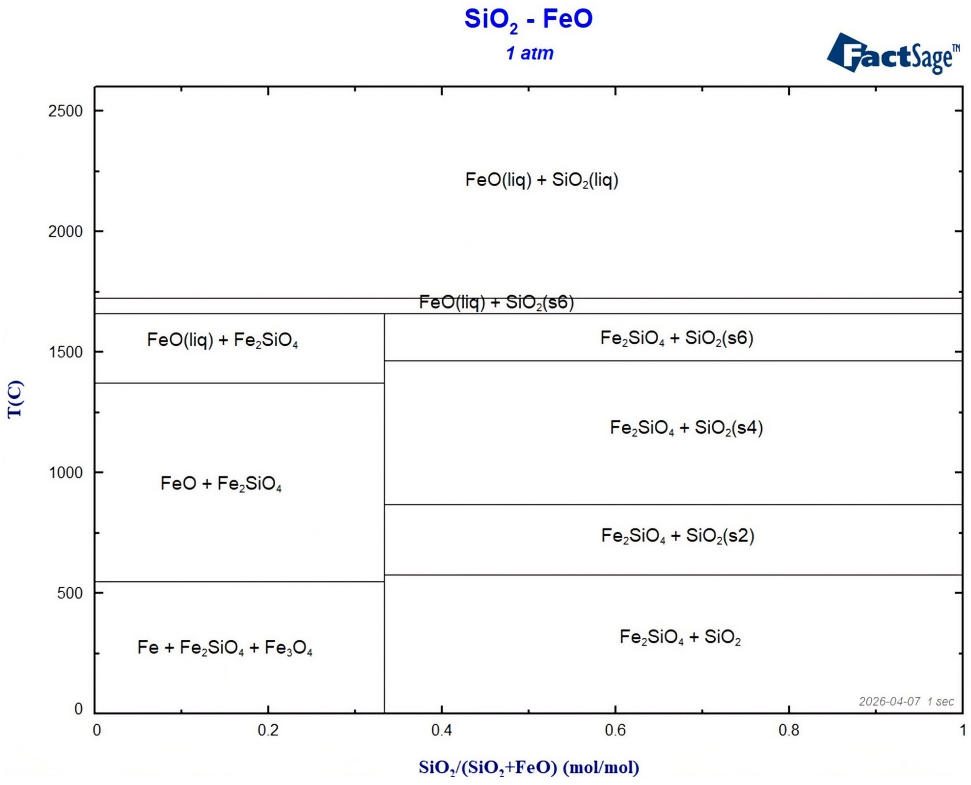

Figure 3.3: Phase diagram of the SiO_2-FeO system at atmospheric pressure.

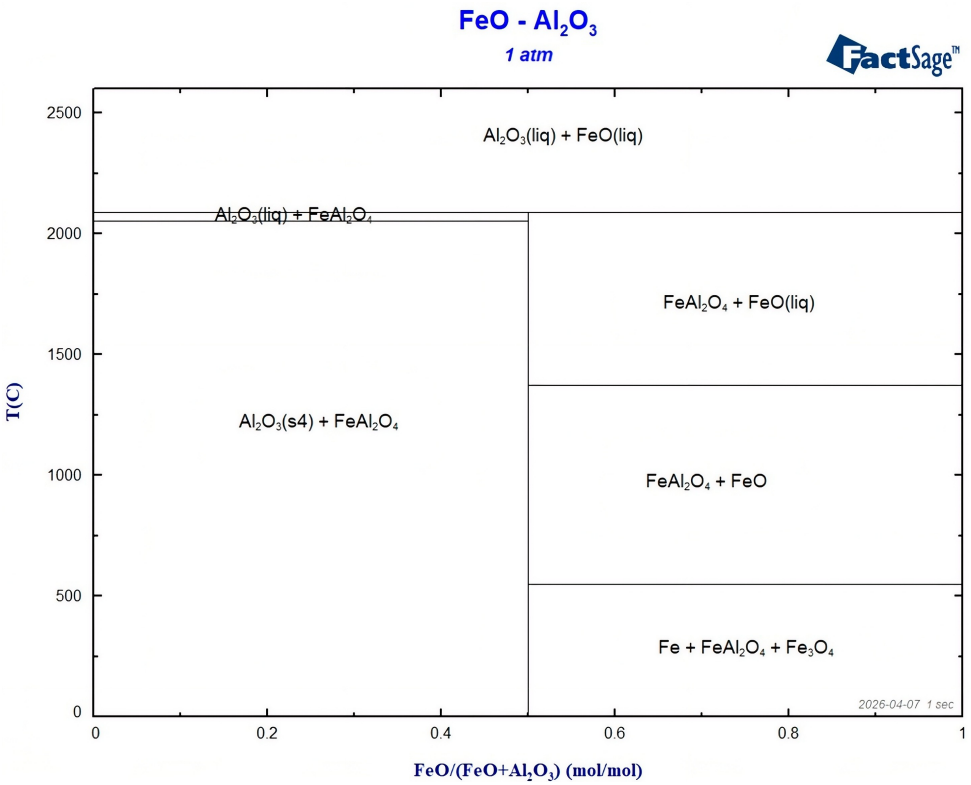

Figure 3.4: Phase diagram of the FeO-Al_2O_3 system at atmospheric pressure.

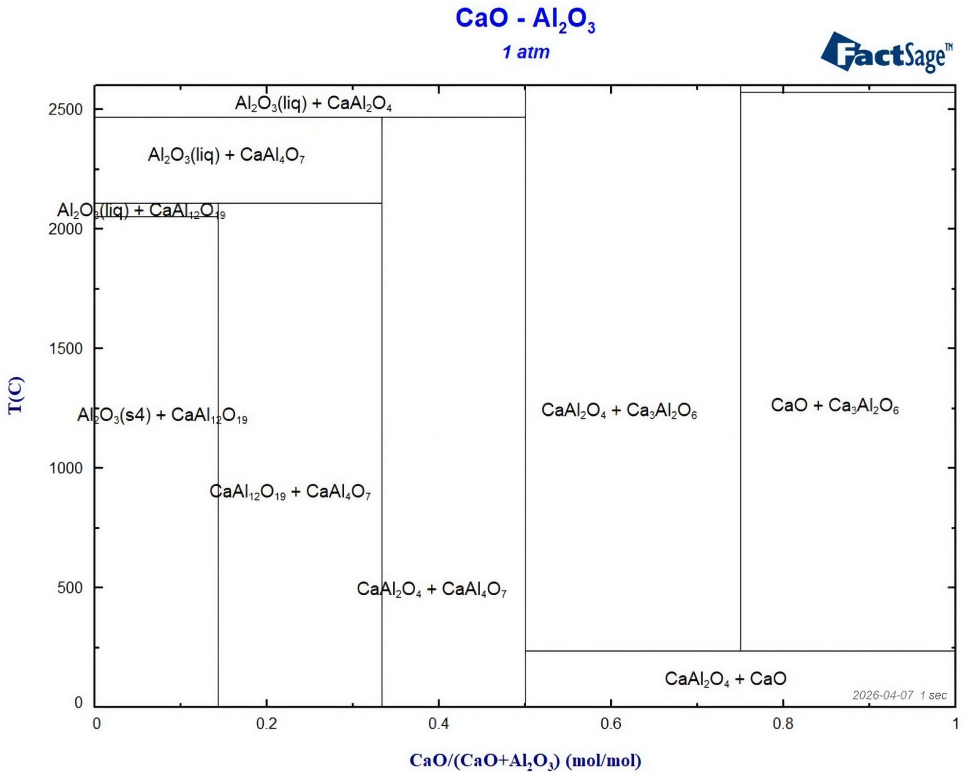

Figure 3.5: Phase diagram of the CaO-Al_2O_3 system at atmospheric pressure.

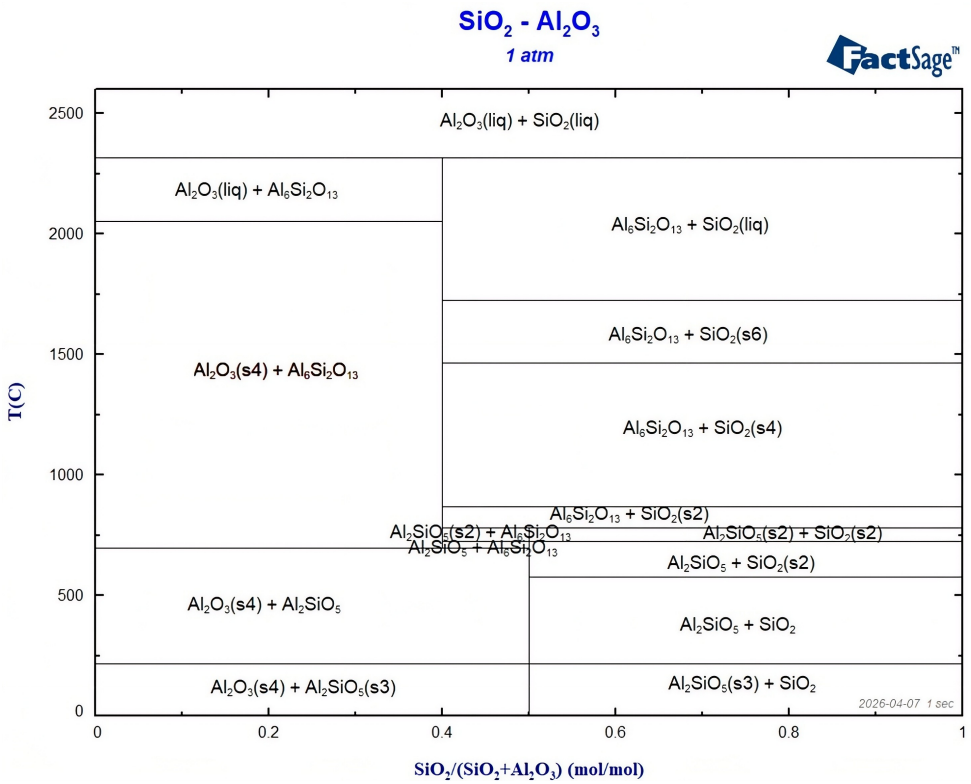

Figure 3.6: Phase diagram of the SiO_2-Al_2O_3 system at atmospheric pressure.

From the observation of the phase diagrams of these key pairs of components, it can be observed that in none of these diagrams is an unstable phase observed up to 600 °C. In addition, all these diagrams show that liquid phases only appear above much higher temperatures (approximately 1400°C). Therefore, it can be concluded that, in a first analysis, there will be no problems regarding the chemical stability during the utilization of iron and steel slags in a rock bed SHTES system.

For the specific case of the EAF slag that will be used as the TES material in the simulations later in this study, the exact material from [40] was considered, as its composition and thermophysical properties were well documented. The composition of the EAF slag used is presented in Table 3.3.

Table 3.3: Composition of the EAF slag used in this study [40]

Compound	(%)
Al_2O_3	13.4
CaO	28.5
Fe_2O_3	24.2
MgO	3.8
MnO	0.5
SiO_2	19.1
TiO_2	2.1

Once the specific composition of the EAF slag that will be used as the TES material is known, it is possible to locate the corresponding regions in the ternary phase diagrams of SiO_2-CaO-Fe_2O_3 and CaO-SiO_2-Al_2O_3, which were taken from the literature and are presented in Figures 3.7 and 3.8.

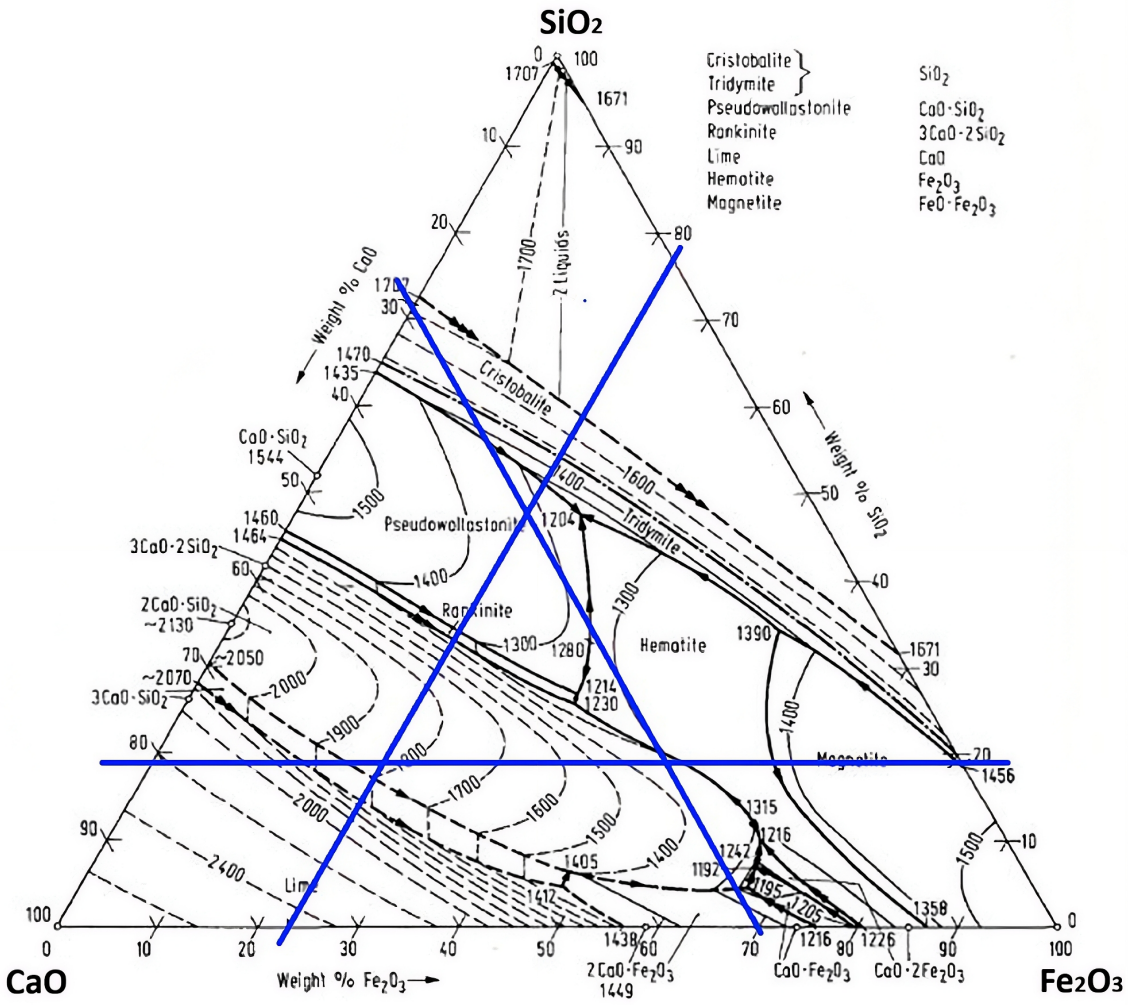

Figure 3.7: Ternary phase diagram of the SiO_2-CaO-Fe_2O_3 system, adapted from [45].

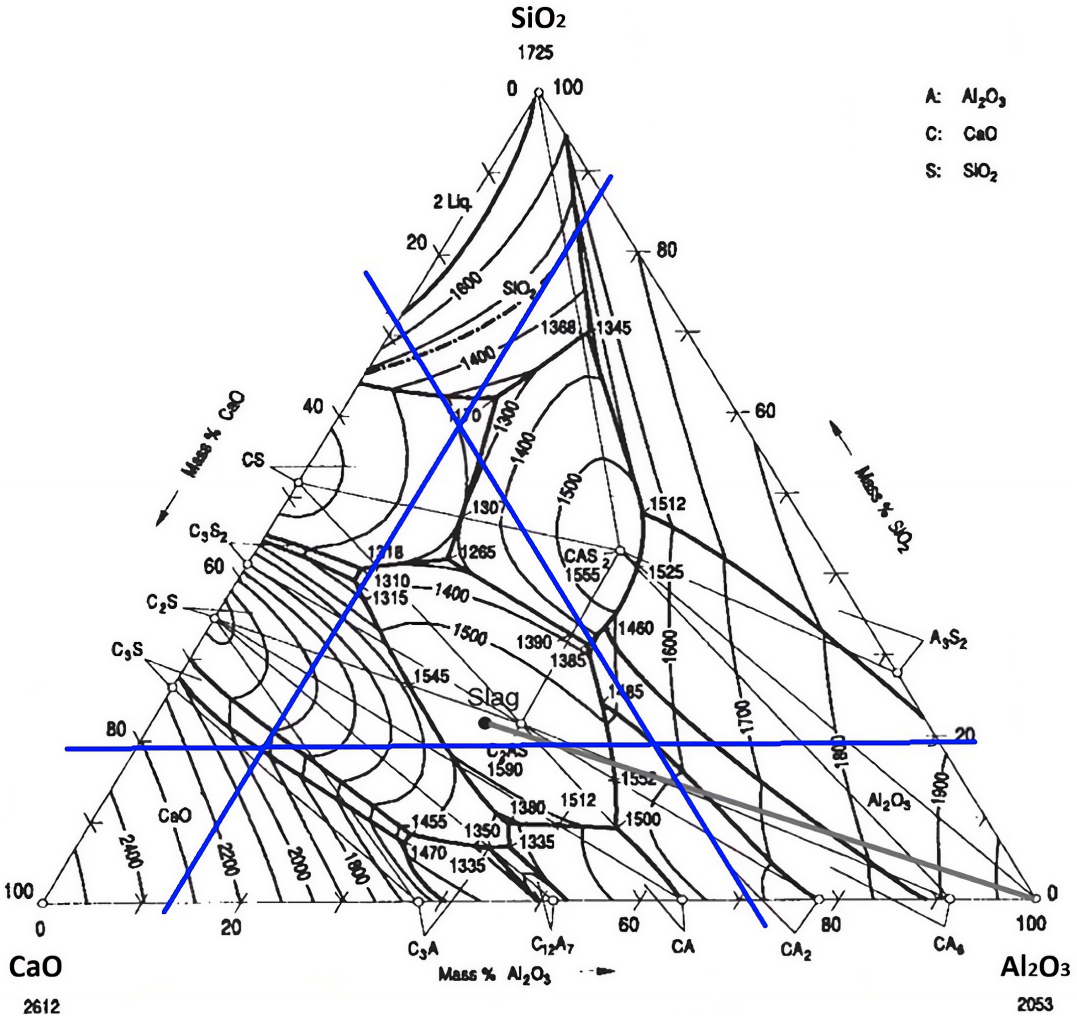

Figure 3.8: Ternary phase diagram of the SiO_2-CaO-Al_2O_3 system, adapted from [46].

First of all, in Figure 3.7, it is possible to observe that the region defined by the drawn lines corresponding to the weight percentage of the components in the diagram is a triangle, instead of a point. This is due to the presence of impurities, such as MgO, MnO and TiO_2, which are also present and, therefore, the sum of the weight percentages of SiO_2, CaO and Fe_2O_3 is less than 100%. Nevertheless, it is still possible to draw key conclusions from this diagram.

On the one hand, the defined region for the slag under analysis sits between 1200°C and 1800°C, which means that the slag is fully liquid around 1500°C. It should be noted that, in reality, the slag's melting point will likely be lower than what the diagram shows because of the presence of impurities (SiO_2, CaO and Fe_2O_3). For a safe TES system, the maximum charging temperature should stay below 1200°C to ensure that the pebbles remain structurally sound and do not start "softening" and, consequently, losing their rigidity and beginning to deform [47]. However, since the maximum charging temperature of the packed-bed system in this study is 617°C, it can therefore be considered that any changes in the properties and performance of the porous medium during operation have negligible effects.

On the other hand, the defined region is located between Pseudowollastonite and Rankinite fields, which means that, upon cooling, the EAF slag will likely crystallize into Calcium-Silicates and Iron Oxides. These are generally stable, high-density minerals, which are excellent for volumetric energy density and energy storage.

Regarding the SiO_2–CaO–Al_2O_3 system shown in Figure 3.8, its analysis is essential for understanding the behaviour of EAF slag, as alumina (Al_2O_3) significantly influences the viscosity and melting characteristics of silicate systems. Similar to the diagram of Figure 3.7 the region defined by the weight percentage of SiO_2, CaO and Al_2O_3 is a triangle, surrounded by the Gehlenite (C_2AS) and the Anorthite (CAS_2) domains. This region sits between 1265°C and 1545°C liquidus temperature isotherms and, despite the presence of impurities, it can be considered that the properties of the slag will remain approximately constant throughout the operation of the packed-bed system. However, the isotherms in this region are very steep and, therefore, small variations in Alumina content could shift the slag's melting point quite rapidly.

At the same time, the presence of Al_2O_3 acts as a stabilising agent by shifting the composition away from the dicalcium silicate (C_2S) phase, which is associated with the disintegration of slag into fine particles [48]. This confirms that the EAF slag selected is chemically robust for thermal cycling.

Finally, FacSage software was used once again to plot the specific heat capacity of the EAF slag used in this study [40] as a function of temperature, as well as the multiple phases diagram of this exact material, which are represented in Figures 3.9 and 3.10.

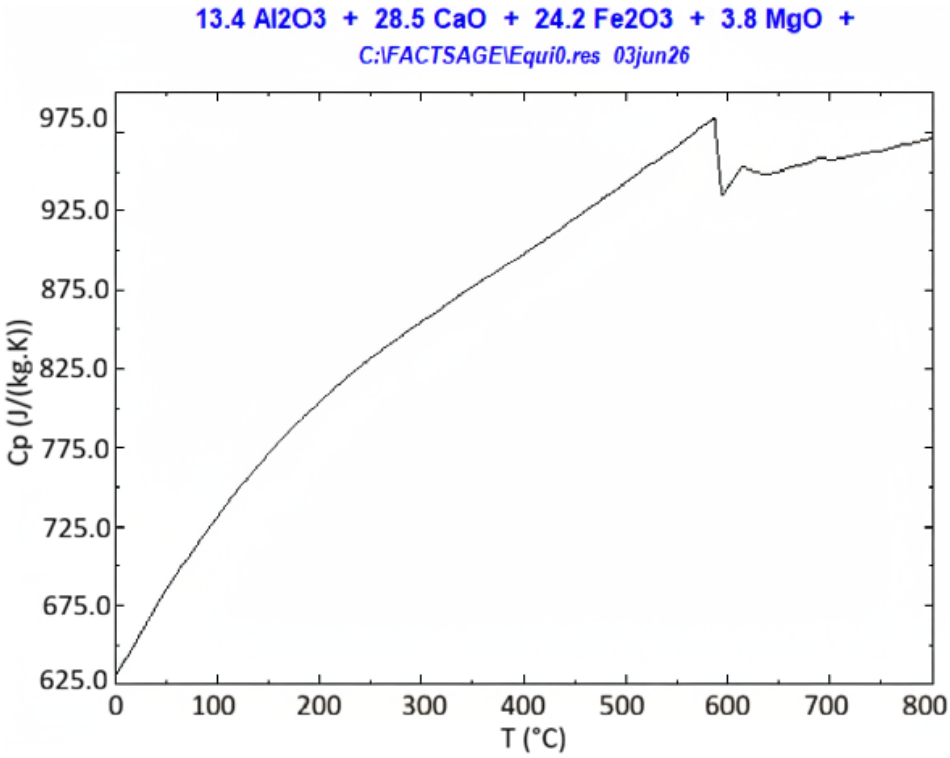

Figure 3.9: Specific heat capacity evolution with temperature of the EAF slag considered in the study.

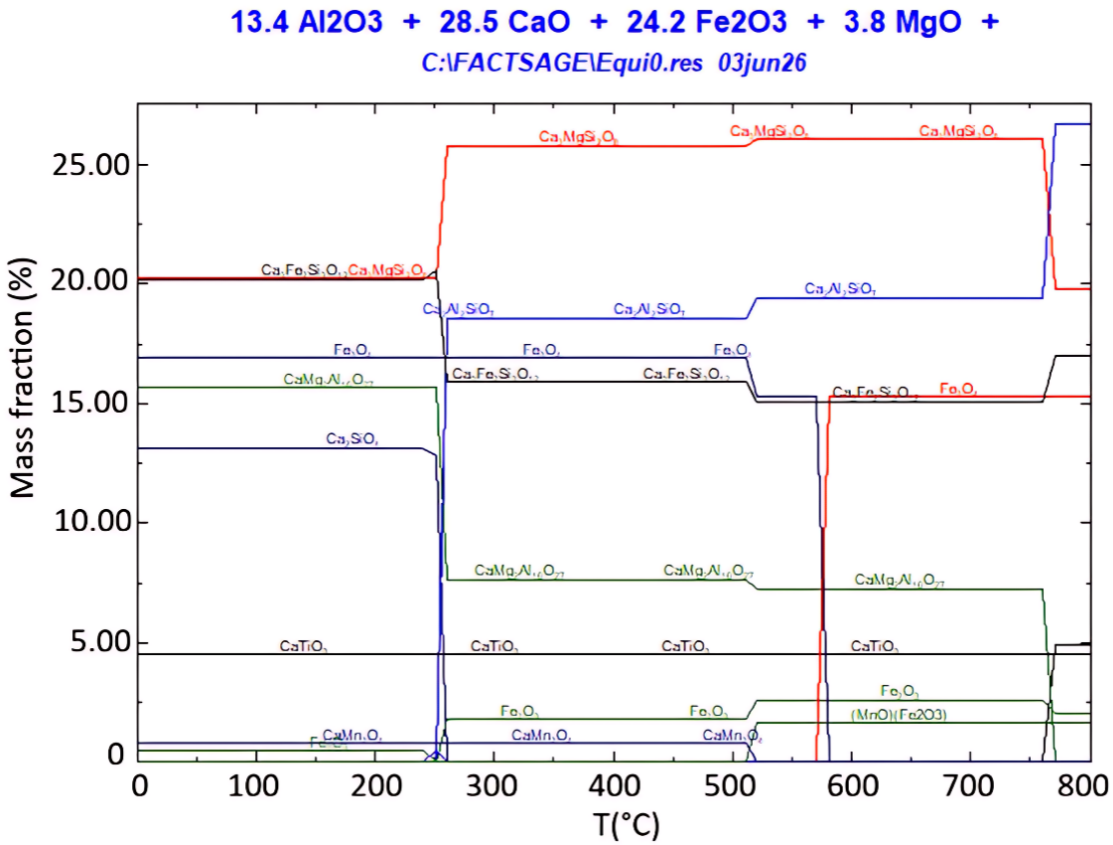

Figure 3.10: Multiple phases diagram of the EAF slag considered in the study.

The equilibrium phase diagram illustrated in Figure 3.10 for the slag with the composition presented in Table 3.3 shows that the material is predominantly composed of calcium-magnesium silicates, calcium aluminosilicates, iron oxides and calcium titanate over the temperature range analysed. Most major phases remain relatively stable between approximately 300 and 750 °C, suggesting good thermodynamic stability within the operating range typically considered for SHTES applications.

However, several phase transitions are observed around 250-300°C and 500-600°C, suggesting redistribution of components among solid phases. Although these transformations do not appear extensive, repeated thermal cycling through these temperature ranges may induce internal stresses due to differences in thermal expansion coefficients between phases, potentially leading to cracking or particle degradation.

Additionally, iron-bearing phases may undergo oxidation-reduction (redox) reactions during thermal cycling, which could result in phase transformations and contribute to long-term degradation of the storage material.

In conclusion, the phase diagram suggests that the slag is a promising candidate for packed-bed sensible thermal energy storage, although experimental assessment of thermal cycling stability and mechanical durability is required to confirm its long-term suitability. While the equilibrium calculations suggest that the slag remains thermodynamically stable at elevated temperatures, repeated

heating and cooling cycles may still lead to mechanical degradation due to phase transformations and thermal expansion mismatch between phases. Consequently, cyclic thermal testing is required to evaluate its long-term structural integrity.

Overall, the thermodynamic assessment performed in this chapter suggests that the selected EAF slag presents the characteristics required for application as a SHTES material in packed-bed systems. The phase diagrams reveal no evidence of phase instability or liquid formation within the intended operating range, while the equilibrium phase assemblage remains largely unchanged between 300 and 750 °C. In this way, although the potential effects of phase transformations, in particular, thermal expansion mismatch and redox reactions during long-term cycling, should be investigated experimentally, the obtained results provide strong evidence of the material's chemical robustness and suitability for high-temperature thermal energy storage applications.

Chapter 4

Numerical Model Development

To evaluate the performance of iron and steel slags as TES materials in packed-bed systems, a 2D large-scale thermal model was developed using COMSOL Multiphysics version 6.4 software [49], due to its capability to solve coupled heat transfer and fluid flow phenomena in porous media. COMSOL Multiphysics, which is based on the Finite Element Method (FEM), has been developed to enable the solution of coupled Partial Differential Equations (PDEs) across multiple interacting physical domains. This is particularly relevant for packed-bed TES, where interactions between the solid storage material and the heat transfer fluid play a critical role. The software enables the implementation of transient simulations, temperature-dependent material properties, and spatially resolved temperature fields, providing a high-fidelity representation of the operation processes that occur in a rock bed system.

4.1 Geometry definition

The first step in developing the thermal model was defining its geometry. To establish a reliable foundation, an existing 2D COMSOL model of a packed-bed system from previous research at DTU Energy and Storage was adopted as a reference framework. However, because the present study demands significantly larger operational capacities, the original dimensions were insufficient. Consequently, several structural modifications were implemented to scale and adapt the baseline geometry to these new design specifications. Furthermore, several geometries were tested using an iterative modeling approach in COMSOL. By optimizing key design specifications, the study sought to achieve enhanced operational performance.

First, a scaling factor of 2 was applied to the reference model in order to increase the dimensions of the model proportionally. In this way, the width and height of the tank containing the TES medium become 382 mm and 201 mm, respectively. In addition, fillets with a radius of 1 mm were added in the four corners that connect the inlet and outlet ducts to the tank, to smooth the geometry. Figure 4.1 illustrates the scaled model, which was the first geometry tested (Geometry 1), with all the relevant dimensions specified, whereas Figure 4.2 illustrates all the components of the model.

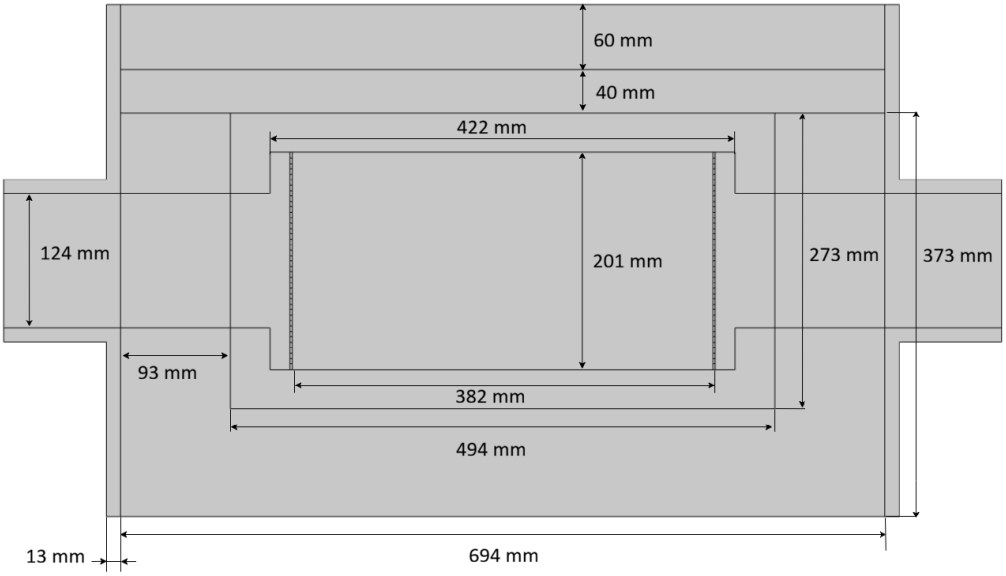

Figure 4.1: Geometric model of the packed bed system with annotated dimensions.

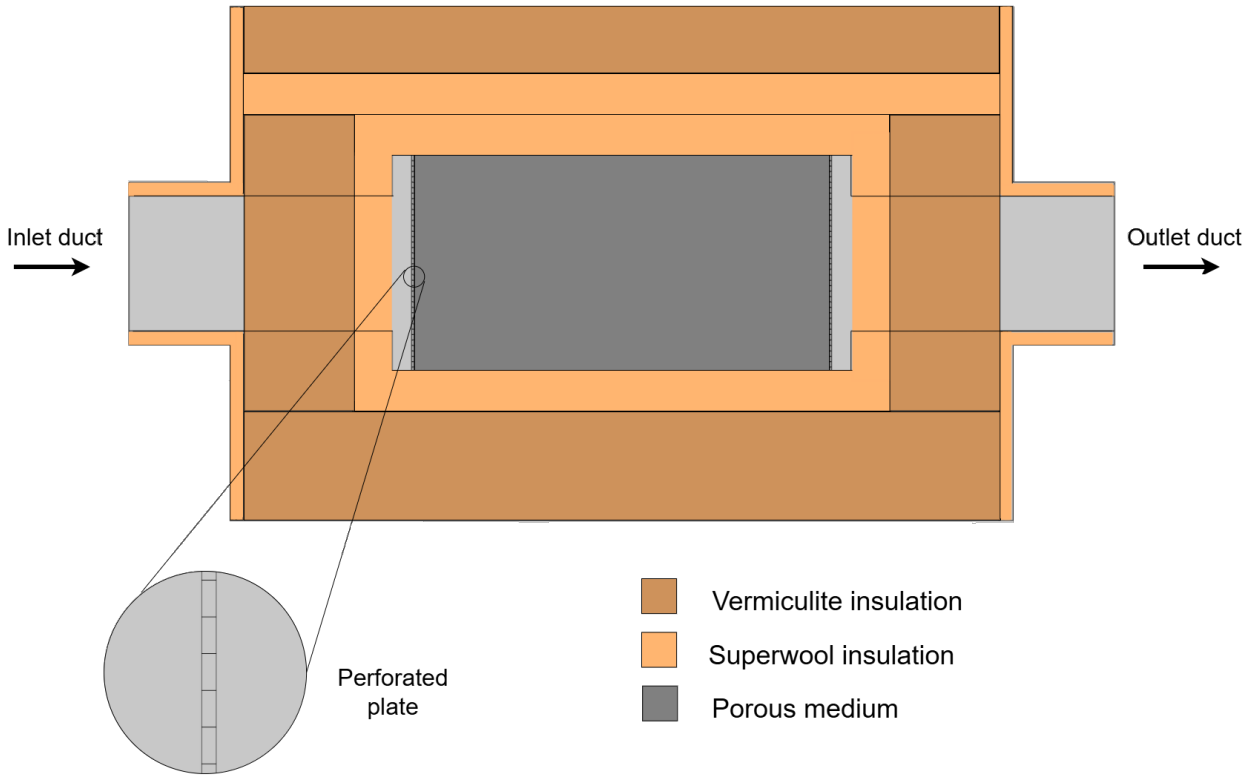

Figure 4.2: Components of the geometric model of the packed-bed system.

Looking at Figure 4.1, the rectangle that occupies the central position is the space where the porous TES material is placed. Charging air is supplied through a cylindrical inlet duct welded to the tank. The ducts are integrated with the tank to ensure consistent thermal and mechanical

continuity at the interfaces. The left and the right side of the tank (inlet and outlet) are perforated to let the air inside the tank. To simplify the geometry, the holes have a distance from each other equal to the diameter of the hole and equal to 2.5 mm.

Due to the significant heat losses that occur during the charging, storing and discharging processes, the tank is enclosed by an efficient multilayer insulation system designed to minimize thermal losses. This insulation assembly consists of an inner layer of superwool wrapped directly around the tank. An additional horizontal layer of the same material is positioned above this primary superwool layer, and a thiner layer of superwool also surrounds the external part of the inlet and outlet ducts, as well as the lateral sides of the whole set. Furthermore, a thicker layer of vermiculite surrounds the lateral sides and bottom of the superwool insulation, with an extra upper layer also placed above the horizontal superwool section.

The second geometry tested was defined using Geometry 1 as a starting point. The modifications included reducing the size of the porous medium to let some air flow to pass below the tank and enter the bed from below through two inlets with a width of 30 mm and a depth (entrance thickness) of 250 mm. A vermiculite insulation barrier was also added to prevent air from escaping through the outlet. Geometry 2 is represented in Figure 4.3.

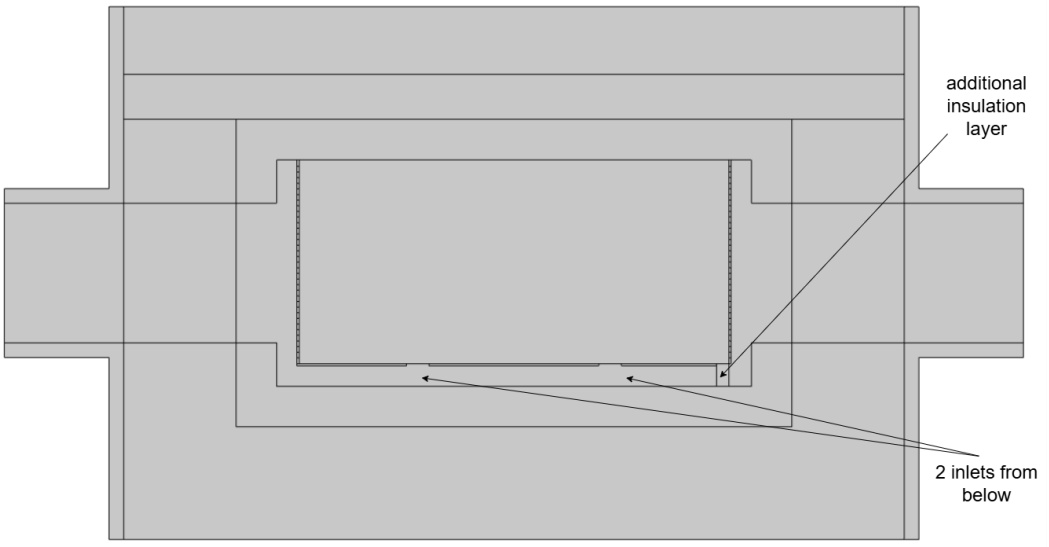

Figure 4.3: Second geometric model of the packed bed system.

Finally, a third geometry was tested, also taking Geometry 1 as a starting point. However, this time, instead of reducing the porous medium to let air inside the bed from below, a second inlet duct was added from below, with a diameter of 40 mm. Figure 4.4 illustrated the third geometrical model.

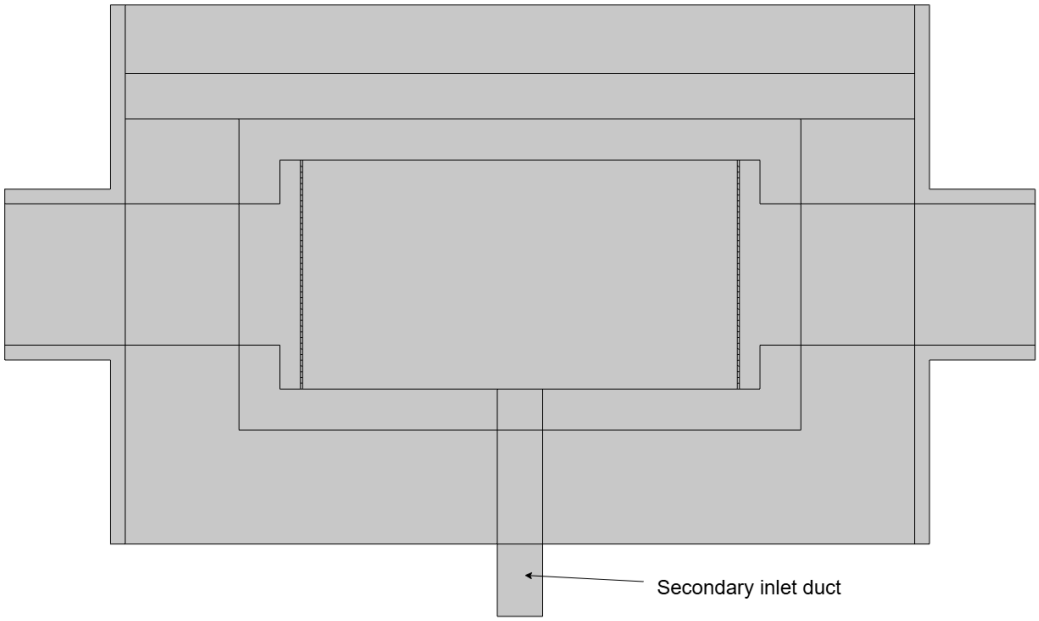

Figure 4.4: Third geometric model of the packed bed system.

4.2 Material properties definition

After defining the geometry, the next step in the development of the thermal model was to assign a material to each component. Whenever possible, the thermo-physical properties were taken directly from COMSOL materials' library. In the other cases, new materials were created and their properties values manually specified.

Regarding the HTF, air was assigned directly from COMSOL and its properties, such as density, viscosity, thermal conductivity, and heat capacity. These properties are defined as temperature and pressure-dependent functions, thereby ensuring realistic fluid behaviour over the full range of operating conditions. These functions are represented in Figures 4.5 and 4.6.

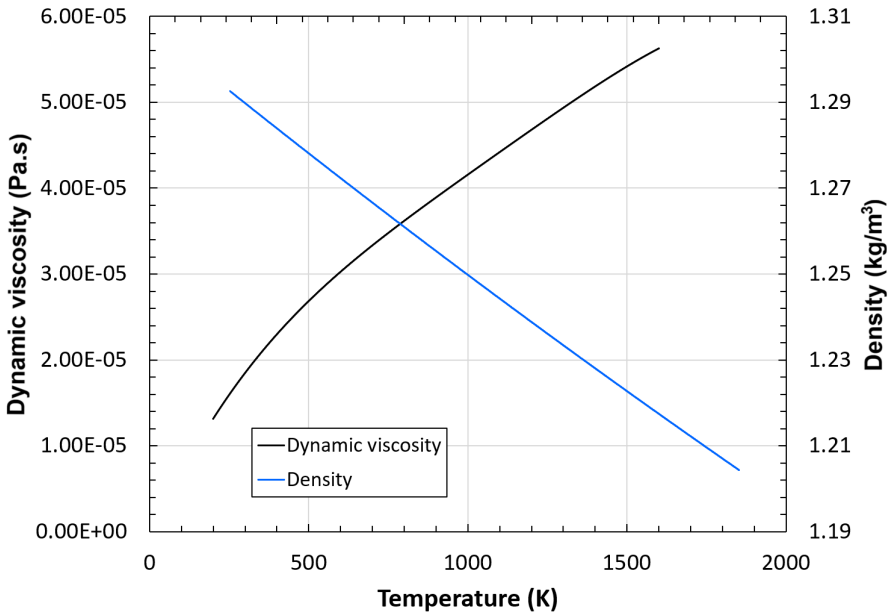

Figure 4.5: Dynamic viscosity and density functions of air.

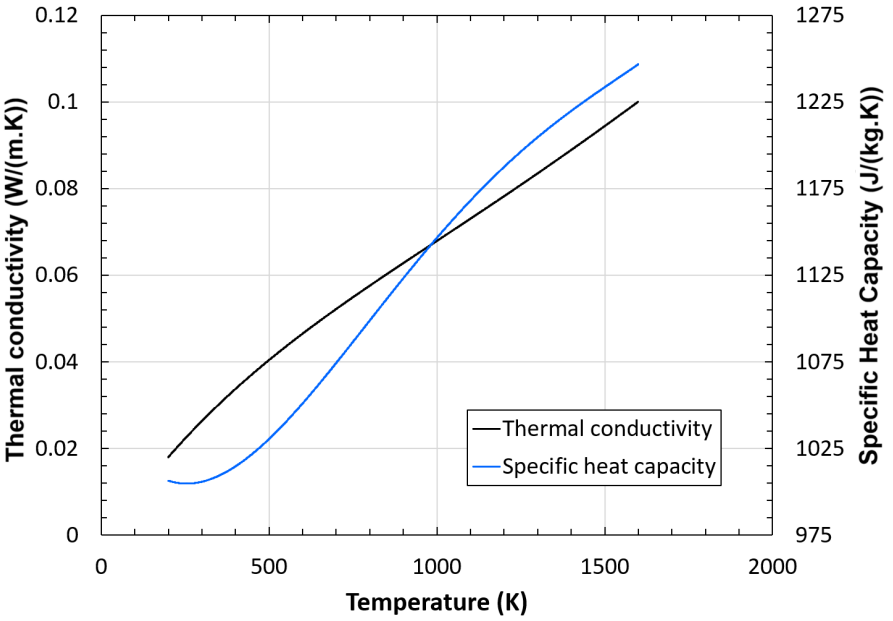

Figure 4.6: Thermal conductivity and specific heat capacity functions of air.

For the structural components, including the inlet and outlet ducts, the external casing of the TES unit, the perforated plates, and the container walls, steel was selected as the construction material. Its thermophysical properties were defined manually in the model and they remain constant throughout the simulations.

Regarding the insulation layers, similarly to steel, superwool and vermiculite thermophysical properties were defined manually in the model and assumed to be constant values. Superwool and vermiculite exhibit low thermal conductivity and low density, characteristics that make them particularly suitable for thermal insulation applications.

Finally, the porous medium was modelled using COMSOL's two-phase porous material formulation. Air was assigned as the fluid phase, while EAF slag was assigned as the pellet phase. The pellets were assumed spherical with a diameter of 15 mm, and the intra-pellet porosity is fixed at 0.001 m. The bed porosity was considered consistent along the packed back and throughout the simulations and was fixed at 0.35.

Table 4.1 presents the input values for the density, specific heat capacity and thermal conductivity of all the materials that integrate the model, with the exception of air. It should be noted that the approximation of these properties as constant is justified, given that their variation under the operating conditions of the packed-bed system is negligible.

Table 4.1: Properties of the materials used in the model

Material	**Density (kg/m^3)**	**Specific Heat Capacity (J/(kg.K))**	**Thermal Conductivity (W/(m.K))**
EAF Slag	3430	933	1.43
Superwool	96	1050	0.16
Vermiculite	80	960	0.064
Steel AISI 4340	7850	475	44.5

4.3 Physics interfaces definition

The next step in the development of the thermal model involved the selection of appropriate physics interfaces capable of accurately representing the underlying phenomena occurring within the packed-bed during operation. A packed-bed system operates based on two coupled processes: the circulation of the HTF through a porous solid medium and the associated heat transfer.

A packed-bed thermal energy storage system is governed by two coupled mechanisms: the flow of the HTF through a porous solid matrix and the associated heat transfer between the fluid and solid phases. Accordingly, the "Free and Porous Media Flow, Brinkman" interface available in COMSOL Multiphysics was employed to describe fluid flow within the porous medium based on the Brinkman equations. In parallel, the "Heat Transfer in Solids and Fluids" interface was used to model heat transfer in both the solid storage material and the fluid phase. Furthermore, the multiphysics coupling "Non-Isothermal Flow" was activated to ensure the simultaneous solution of momentum and energy conservation equations.

4.3.1 Free and porous media flow, Brinkman

In order to account for the fluid flow in the porous medium in the COMSOL Multiphysics software, the momentum equation is applied by Free and Porous Media Flow (Brinkman) physics, as well as the continuity equation, in accordance with Equations 4.1 and 4.2 [50].

$$\frac{\rho_f}{\varepsilon_p}\left(\frac{\partial u}{\partial t}+(u\cdot\nabla)\frac{u}{\varepsilon_p}\right)=-\nabla p+\nabla\cdot\left[\frac{1}{\varepsilon_p}\left\{\mu(\nabla u+(\nabla u)^T)-\frac{2}{3}\mu(\nabla\cdot u)I\right\}\right]-\left(\kappa^{-1}\mu+\frac{Q_m}{\varepsilon_p^2}\right)+F \tag{4.1}$$

$$\frac{\partial(\varepsilon_p\rho_f)}{\partial t}+\nabla\cdot(\rho_f u)=Q_m \tag{4.2}$$

where ρ_f is the density of the fluid (kg/m^3); ε_p is the porosity of the solid medium; u is the velocity vector (m/s); p is the pressure (Pa); μ is the fluid's dynamic viscosity (Pa·s); I is the identity matrix; κ is the permeability of the porous medium (m^2); Q_m is a mass source or sink (kg/(m^3·s)); and F represents any external forces applied on the porous medium, including the gravitational force (N). Note that conservation of mass is assumed, i.e. no mass is created or destroyed inside the domain, therefore the mass source term can be reduced to zero ($Q_m = 0$).

The fluid flow within the porous packed-bed was modeled using the Brinkman formulation, which extends Darcy's law by incorporating viscous shear effects. In COMSOL Multiphysics, the "Free and Porous Media Flow, Brinkman" interface solves the momentum conservation equation in the form of a modified Navier–Stokes equation, including both viscous and permeability-related resistance terms. This allows for a more accurate representation of flow behavior within the porous medium, particularly in regions where viscous effects are non-negligible.

In this way, the first and second terms on the left side of Equation 4.1 refer to the local and convective components of acceleration, respectively. On the other hand, the right side of the equation is a summation of hydrostatic effects, represented by the term $-\nabla p$, the divergence of deviatoric stress $\nabla\cdot\left[\frac{1}{\varepsilon_p}\left\{\mu(\nabla u+(\nabla u)^T)-\frac{2}{3}\mu(\nabla\cdot u)I\right\}\right]$, the resistance from the porous region, represented by $\left(\kappa^{-1}\mu+\frac{Q_m}{\varepsilon_p^2}\right)$, and body forces (such as gravity), represented by the term F.

The permeability of a porous medium, κ, quantifies its ability to allow fluid flow, with higher permeability indicating lower resistance to flow. It is strongly influenced by the geometrical characteristics of the pore structure, including pore size, shape, and connectivity. The permeability of the packed bed was estimated using the Kozeny–Carman equation, which relates the bed porosity and particle diameter to the flow resistance within the porous medium [50]:

$$\kappa=\frac{D_p^2\varepsilon_p^3}{180(1-\varepsilon_p)^2} \tag{4.3}$$

where D_p is the particle diameter.

4.3.2 Heat transfer in solids and fluids

To model the heat transfer in both the solid storage material and the fluid phase inside the rock bed, the energy equation and Fourier's law are applied to the 2D model by "Heat Transfer in Solids and Fluids" physics, as represented by Equations 4.4 and 4.5 [51]:

$$d_z \rho C_p \frac{\partial T}{\partial t} + d_z \rho C_p u \cdot \nabla T + \nabla \cdot q = d_z Q + q_0 + d_z Q_{ted} \tag{4.4}$$

$$q = -d_z k \nabla T \tag{4.5}$$

where d_z is the thickness (or scaling factor in the z-direction); ρ is the density of the fluid (kg/m^3); C_p (is the specific heat capacity (J/(kg·K)); T is the absolute temperature (K); u is the velocity vector (m/s); q is the heat flux vector (W/m^2); Q is the volumetric heat source (W/m^3); q_0 is the external surface heat input (W/m^2); Q_{ted} is the thermoelastic damping heat source (W/m^3); and k is the thermal conductivity (W/(m·K)).

On the left side of the Equation 4.4, the term $d_z \rho C_p \frac{\partial T}{\partial t}$ represents the energy storage achieved through the variation of temperature with time, whereas $d_z \rho C_p u \cdot \nabla T$ represents the convective heat transport and $\nabla \cdot q$ accounts for the heat conduction. The right-hand side of this Equation is the sum of all contributions from heat sources: internal heat generation, boundary heat input, and device-specific heat sources.

4.3.3 Non-isothermal Flow

Finally, the multiphysics "Non-isothermal Flow" solves additional equations to account for additional energy source contributions that appear when fluid flow and heat transfer are coupled, particularly in compressible flow and porous media, as it is the case. These equations are presented from 4.6 to 4.9 [52]:

$$Q_p = \alpha_p T \left(\frac{\partial p_A}{\partial t} + u \cdot \nabla p_A \right) \tag{4.6}$$

$$\alpha_p = -\frac{1}{\rho} \left(\frac{\partial \rho}{\partial T} \right)_P \tag{4.7}$$

$$Q_{vd} = \tau : \nabla u + Q_{porous} \tag{4.8}$$

$$Q_{porous} = \mu u \cdot \kappa^{-1} \cdot u + \rho \beta |u|^3 \tag{4.9}$$

where Q_p is the heating (or cooling) due to pressure changes (W/m^3); T is the absolute temperature (K); p_A is the absolute pressure (Pa); u is the velocity vector (m/s); α_p is the thermal expansion

coefficient (K^{-1}); ρ is the density (kg/m^3); Q_{vd} is the viscous dissipation (W/m^3); τ is the viscous stress tensor (N/m^2); Q_{porous} is the porous medium losses (W/m^3); μ is the fluid's dynamic viscosity (Pa·s); κ is the permeability of the porous medium (m^2); and β is the inertial coefficient.

In Equation 4.6 note that the pressure variations can be due to pressure changing in time or due to pressure changes along flow. The thermal expansion coefficient α_p expresses how much density changes with temperature, to the extent that the larger its value, the more the fluid expands when heated.

In Equation 4.9, Darcy and Forchheimer losses represent the pressure drop of fluids flowing through porous media, combining viscous drag and inertial drag effects, represented by the first and second terms in the equation, respectively. Darcy's law dominates at low velocities, while the Forchheimer correction dominates at high velocities. The total loss is modeled as a sum of these two, crucial for the simulation of flow in porous structures.

4.4 Mesh generation

Determining the optimal mesh density is a fundamental step in FEM simulations, as it requires a strategic balance between element refinement and computational efficiency.

To determine the optimal mesh size for numerical accuracy and convergence, a mesh independence study was performed using Geometry 3, as this was the most complex geometry tested. As boundary conditions, inlet flow rates equal to 500 L/min and 66.67 L/min through the main and secondary inlet ducts, respectively, were employed. Table 4.2 highlights the specification parameters of each of the tested mesh sizes, whereas Figure 4.7 illustrates the variations obtained in the temperature (K) plot as a function of charging time (h) during 20 hours of charging. Figures 4.8 and 4.9 present the relative error associated with each mesh size, taking the Extremely Fine mesh as the reference case, for two different points within the packed bed, whose coordinates are provided in Table 5.3. These mesh sizes are all predefined in the physics-controlled meshes available on COMSOL Multiphysics.

Table 4.2: Specification parameters of each of the tested mesh sizes

Mesh Size	Number of elements	Maximum element size (m)	Minimum element size (m)
Extremely Fine	81444	0.00906	1.61×10^{-5}
Extra Fine	68878	0.0181	6.8×10^{-5}
Finer	25008	0.0335	1.13×10^{-4}
Fine	17396	0.048	2.72×10^{-4}
Coarse	11942	0.0906	0.00181
Coarser	9518	0.118	0.00544
Extra Coarse	6190	0.181	0.0145
Extremely Coarse	5218	0.299	0.0453

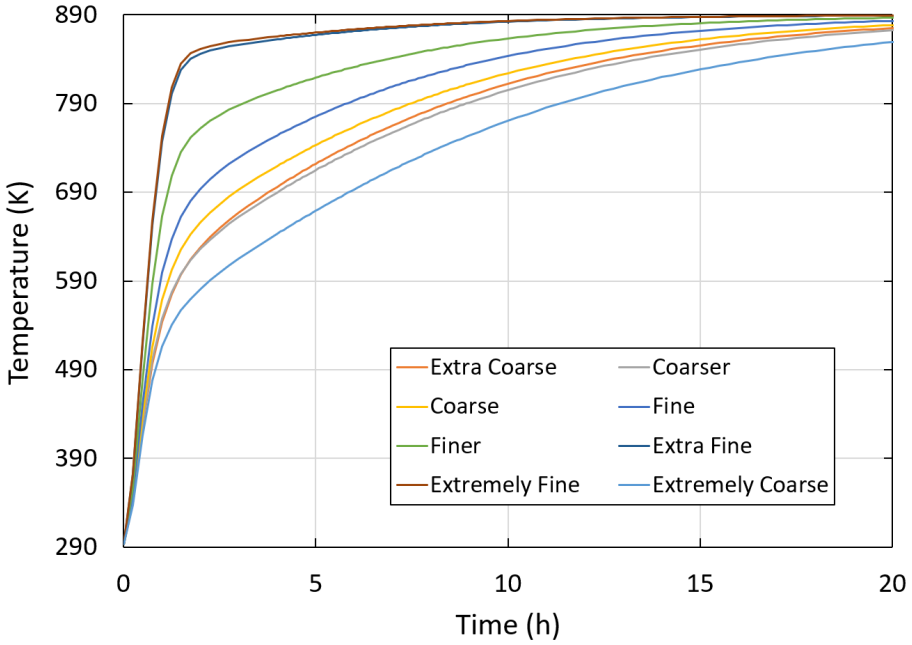

Figure 4.7: Influence of mesh size on the temperature profile at Point 5.

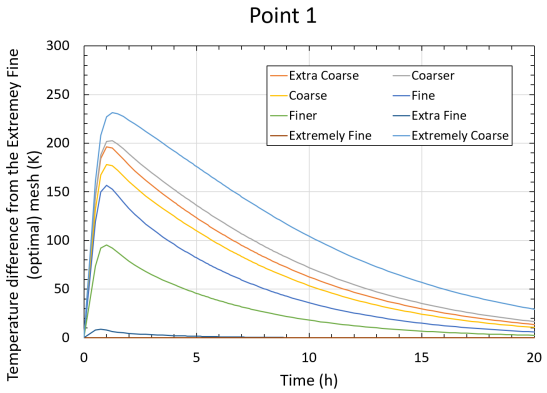

Figure 4.8: Associated error with each mesh size for Point 1.

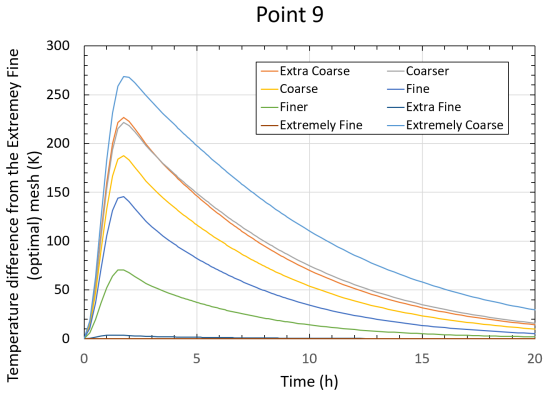

Figure 4.9: Associated error with each mesh size for Point 9.

From the analysis of Figures 4.7 to 4.9 it is evident that the mesh size has a big influence on the packed-bed performance. It is possible to see that, even though all the curves converge close to the final temperature at the end of the 20 hours, a clear difference between each curve and the reference curve (Extremely Fine mesh) can be observed until that time is reached. While Extremely Fine and Extra Fine meshes curves almost overlap and showcase the best results, the Extremely Coarse, Extra Coarse, Coarser and Coarse mesh presented a significant difference from the optimal results, corresponding to the Extremely Fine and Extra Fine curves. In turn, the Finer and Fine mesh curves showcased intermediate results.

Based on the mesh independence study, the Fine mesh was selected to perform the following simulations, as this mesh provides a reasonable degree of numerical accuracy while requiring less computational effort than the Extremely Fine, Extra Fine and Finer meshes. Figure 4.10 illustrates

the Fine mesh size employed to build the mesh for the third geometric model. It can be observed that the finer elements are used in the domains and the boundaries affected by the flow of air, while the other parts, such as the thermal insulation layers, have bigger mesh elements, as their geometry is not so complex.

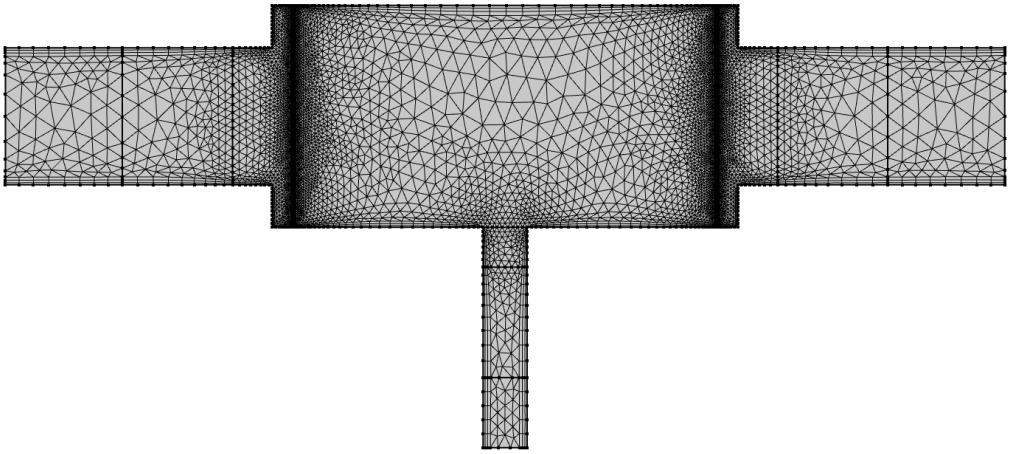

Figure 4.10: Fine mesh used in the simulations using the third geometric model.

After building a mesh with adequate density, the next step in the development of the thermal model is to define the solver configurations and initiate the simulations.

4.5 Solver configuration

To evaluate the performance of the packed-bed TES system, the numerical fluid simulations were restricted to the charging and resting phases. This approach is justified by the thermodynamic and geometric symmetry of the system; the discharging process essentially operates as the fluid dynamic and thermal inverse of the charging phase, utilizing the same porous media properties and flow boundaries. Furthermore, isolating the charging and resting periods allows for a targeted investigation into the two most critical operational constraints: the system's maximum thermal storage capacity and its thermal degradation during standby idling.

In this way, the first two sets of simulations performed for this study aimed to determine the best geometry for the packed-bed and evaluate the influence of varying flow conditions. For both investigations, the charging behavior was modeled using a two-step study. The first step corresponds to the stationary case and was intended to determine the initial conditions to be used in the second step. This second stage simulated the time-dependent charging behavior of the system under realistic operating conditions.

To simulate the resting behaviour of the packed-bed system, a second study was created. In fact, since the boundary conditions had to be changed in order to entirely replicate the conditions verified during a resting period, this could only be done through a new study instead of simply adding a third step to the first study in COMSOL. In this way, it was necessary to disable the air

flow rates coming through and leaving the ducts, as if the ducts were sealed. Additionally, a heat flux boundary condition of external natural convection in the vertical walls in the lateral walls of the system was applied.

4.6 Thermal performance indicators

Some relevant performance parameters that should be evaluated for the system under analysis include the heat losses during the three processes that occur during operation, the overall efficiency of the system and the pressure drop throughout the packed-bed.

Heat losses

Considering only the losses that occur only between the tank and the surrounding area, the heat lost during the charging, resting and discharging processes can be determined through the fundamental equation for heat transfer across a solid surface [53], as shown in equations 4.10, 4.11 and 4.12, respectively. It should be noted that in these equations, the value of the overall heat transfer coefficient is not constant, and will change according to the surface that is being analyzed, the number of insulation layers and depending on the process of operation. This coefficient, for each case, can be determined by adding up all thermal resistances between the hot bed and the ambient air, as indicated in equation 4.13:

$$Q_{lost,charge} = \int_0^{t_{ch}} U\,A_s(T_{bed}(t) - T_{amb})\,dt \tag{4.10}$$

$$Q_{lost,rest} = \int_0^{t_{rest}} U\,A_s(T_{bed}(t) - T_{amb})\,dt \tag{4.11}$$

$$Q_{lost,discharge} = \int_0^{t_{dis}} U\,A_s(T_{bed}(t) - T_{amb})\,dt \tag{4.12}$$

where U is the overall heat transfer coefficient (W/(m^2·K)); A_s is the external surface area (m^2); T_{bed} is the temperature of the bed at each instant t (K); T_{amb} is the reference or ambient temperature outside of the bed (K):

$$U = \left[\frac{1}{h_{in}} + \sum_{i=1}^{n}\frac{\delta_i}{k_i} + \frac{1}{h_{out}}\right]^{-1} \tag{4.13}$$

where h_{in} is the inside convection heat transfer coefficient (W/(m^2·K)); δ_i is the thickness of the insulation layer i (m); k_i is the thermal conductivity of the insulation material i (W/(m·K)); and h_{out} is the outside convection heat transfer coefficient (W/(m^2·K)). It should be noted that h_{in} is not a constant; COMSOL updates it dynamically at every time step because the density and viscosity of the internal air change with temperature. As for h_{out}, since the outside temperature remains constant throughout the operation of the packed-bed, remains a constant value.

Charging, discharging and overall efficiencies

Firstly, the charging process will be analyzed. The heat stored by the porous medium during the charging process is given by equation 4.14 [53]. Even though the bed does not heat up uniformly, to simplify the calculations, a constant specific heat of the porous medium is considered and is equal to the corresponding value for 500°C and an average of the temperature obtained at the end of the charging process is considered:

$$Q_{stored,bed} = m \int_{T_{initial}}^{T_{final,avg}} Cp(T)\,dT \approx m \cdot Cp(500°C) \cdot (T_{final,avg} - T_{initial}) \tag{4.14}$$

with

$$m = \rho \cdot V_{storage}(1 - \varepsilon_p) \tag{4.15}$$

where m is the mass of TES material inside the packed-bed (kg); Cp is the specific heat of the TES material (J/(kg·K); $T_{final,avg}$ and $T_{initial}$ are the average final and the initial temperatures of the pebbles (K); ρ is the density of the TES material (kg/m^3); $V_{storage}$ is the volume of storage material (m^3); and ε_p is the porosity of the storage medium.

The heat supplied by the HTF during the charging process is given by [53]:

$$Q_{supplied,fluid} = \int_0^{t_{ch}} \dot{m}_f \cdot Cp_f(T) \cdot (T_{in,ch} - T_{ref})\,dt \tag{4.16}$$

where t_{ch} is the charging time (s); $\dot{m}_f$ is the mass flow rate of the HTF, in this case air, (kg/s); $Cp_f(T)$ is the specific heat of the HTF, which depends of the temperature (J/(kg·K); $T_{in,ch}$ is the constant high temperature of the air entering the top of the bed (K); and T_{ref} is the reference temperature, which is considered equal to ambient temperature.

Knowing the heat stored by the porous medium and the heat supplied by the HTF, it is then possible to determine the efficiency of the charging process:

$$\eta_{ch} = \frac{Q_{stored,bed}}{Q_{supplied,fluid}} \times 100\% \tag{4.17}$$

Regarding the discharging process, the energy recovered is the energy actually extracted by the cold air being pumped back through the bed that will be later used for a process. This energy can be determined [53] by:

$$Q_{recovered,fluid} = \int_0^{t_{dis}} \dot{m}_f \cdot Cp_f(T) \cdot (T_{out,dis}(t) - T_{in,dis})\,dt \tag{4.18}$$

where t_{dis} is the charging time (s); $\dot{m}_f$ is the mass flow rate of the HTF (kg/s); $Cp_f(T)$ is the specific heat of the HTF, which depends of the temperature (J/(kg·K); $T_{out,dis}(t)$ temperature of the air leaving bed (K) - this value is not constant: at the start of discharge, it will be very close to the maximum charge temperature and, as the bed cools, this temperature will eventually drop; and $T_{in,dis}$ is the temperature of the HTF entering the bed in the beginning of the discharging process, which is equal to ambient temperature.

The energy released by the packed-bed during discharging is given by [53]:

$$Q_{released,bed} = m \int_{T_{start,dis,avg}}^{T_{end,dis,avg}} C_p(T)\, dT \approx m \cdot C_p(500^{\circ}C) \cdot (T_{end,dis,avg} - T_{start,dis,avg}) \tag{4.19}$$

where m is the mass of TES material inside the packed-bed (kg); C_p is the specific heat of the TES material (J/(kg·K)); $T_{end,dis,avg}$ and $T_{start,dis,avg}$ are the average temperatures of the pebbles at the end and at the start of the discharging process (K).

Knowing the heat recovered by the HTF and the heat released by the porous medium, it is then possible to determine the efficiency of the discharging process:

$$\eta_{dis} = \frac{Q_{recovered,fluid}}{Q_{released,bed}} \times 100\% \tag{4.20}$$

Finally, given that both the initial energy input and final output of the TES unit are measured as electricity, the overall system round-trip efficiency can be determined. The fan's electrical consumption ($E_{pumping}$) is directly aggregated into the total charging energy demand [54]:

$$\eta_{overall} = \frac{E_{electricity,discharged}}{E_{electricity,charged} + E_{pumping}} \times 100\% \tag{4.21}$$

Pressure drop

The larger the size of the packed-bed system, the more significant is the pressure drop along the packed-bed. The pressure drop in porous media is the loss of fluid pressure (-ΔP) as it flows through a porous structure, driven by viscous drag at low speeds (linear, Darcy flow) and inertial effects at high speeds (quadratic, Forchheimer flow). It is commonly predicted using the Ergun equation [54]:

$$-\frac{\Delta P}{\Delta L} = \frac{150\,\mu\,(1-\varepsilon_p)^2}{D_p^2\,\varepsilon_p^3} v + \frac{1.75\,\rho\,(1-\varepsilon_p)}{D_p\,\varepsilon_p^3} v^2 \tag{4.22}$$

where ΔL is the length of the porous domain (m); μ is the fluid dynamic viscosity (Pa·s); ε_p is the porosity of the porous medium; D_p is the pellet diameter (m); and v is the fluid velocity (m/s).

4.7 Limitations of the numerical model

While the developed numerical model effectively captures the dominant fluid dynamics and transient thermal behaviors within the packed-bed system, certain assumptions were implemented. This section outlines the primary physical simplifications, geometric constraints, and operational assumptions embedded within the model:

- The numerical model was constrained to a two-dimensional (2D) domain to maintain computational efficiency during geometric optimization iterations. However, in real 3D packed beds, fluid channeling typically occurs near the container walls due to localized increases in

porosity. The 2D model assumes an idealized, uniform cross-sectional flow slice, failing to capture asymmetric flow distribution around the entire perimeter of the tank.

- The "Free and Porous Media Flow, Brinkman" and "Heat Transfer" interfaces model the bed used homogeneous and idealized parameters. In fact, the bed porosity and its derived permeability were assumed completely uniform throughout the spatial domain. Real EAF slag pebbles possess irregular shapes, surface roughness, and variable packing configurations, leading to localized variations in porosity and random preferential flow paths. In addition, the model defines the solid phase as perfect spheres with a fixed diameter of 15 mm, whereas industrial EAF slag is inherently polydisperse, consisting of broken, angular fragments of varying sizes. This shape irregularity affects both the localized interstitial heat transfer coefficient and the true geometric surface area available for fluid-solid convection. Finally, while a minor intra-pellet porosity was defined, the model assumes a uniform temperature throughout each solid particle, neglecting internal thermal gradients. For low thermal conductivity materials like EAF slag, real-world operation would experience internal temperature gradients within individual pebbles, slowing down the overall charging and discharging kinetics compared to numerical predictions.

- The thermophysical properties of the structural steel, insulation layers, and the solid EAF slag were treated as constant values evaluated at average operating temperatures. Although the specific heat capacity (C_p) and composition transitions of the selected EAF slag were analyzed using FactSage, they were implemented as static constants in COMSOL. In reality, C_p increases progressively with temperature, meaning that the slag's actual capacity to store heat changes dynamically with temperature. In reality, as the thermocline layer (the transition zone between hot and cold air) moves through the tank, the material's heat storage behavior changes continuously rather than remaining constant.

- The physical model does not account for the thermal expansion or contraction of the steel shell, insulation, or the slag bed itself. The severe thermal cycles (25°C to over 617°C) would induce mechanical stresses and structural settling of the pebbles, possibly altering the structural porosity over time.

- Auxiliary flow rates injected through the secondary inlet of the packed-bed system were simplified into velocity profiles that derived volumetric flow rates numerically. For this reason, this approach fails to capture the chaotic swirling (turbulence) and localized pressure drops that naturally occur where secondary pipes connect to the main tank.

- The simulation only modeled the charging and resting phases, assuming the discharging phase would behave symmetrically. While this establishes clear system boundaries, it neglects the physical mixing and fluid destabilization caused by buoyancy effects when the hot and cold fluid streams reverse direction in a real tank.

Chapter 5

Simulation Cases Results and Discussion

5.1 Comparison of the results obtained with different geometries

This section describes the geometric optimization process and evaluates the results of three different configurations. It should be highlighted that, for consistency, the specification parameters of the model were kept constant, in particular, the temperature of the heated air at the inlet and the atmospheric pressure condition at the outlet. Furthermore, in all simulations the TES material used was EAF slag, as it is the focus of the study. In all the three geometries tested a physics-controlled mesh was used, with the same element size (fine mesh).

A first attempt to simulate the charging of the packed-bed aimed to achieve the full heating of the bed after 10 and after 20 hours of charge. This was possible using a total flow rate of heated air equal to 1200 L/min: in the case of the third geometric model with two air inlets, a flow rate of 1000 L/min and a flow rate of 200 L/min at the main inlet and secondary inlets, respectively, were used. Due to implementation constraints in COMSOL Multiphysics, the secondary stream was modeled using an inlet velocity condition and the corresponding volumetric flow rate was then derived numerically by integrating the velocity profile across the inlet cross-sectional area. The temperature contours obtained with the three geometries are presented in Figures 5.1 and 5.2, taken after 10 and after 20 hours of charging, respectively.

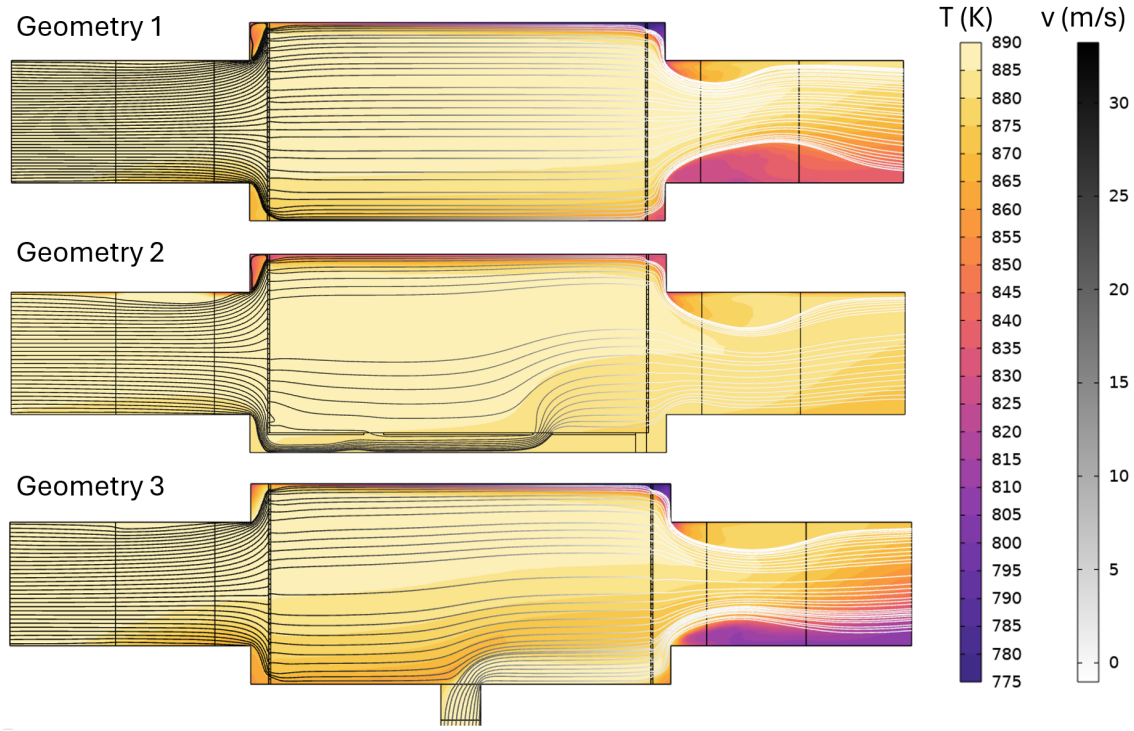

Figure 5.1: Temperature contours (K) and velocity field streamlines (m/s) obtained with the three geometric models after 10 hours of charging, for an inlet air flow rate of 1200 L/min at 890 K.

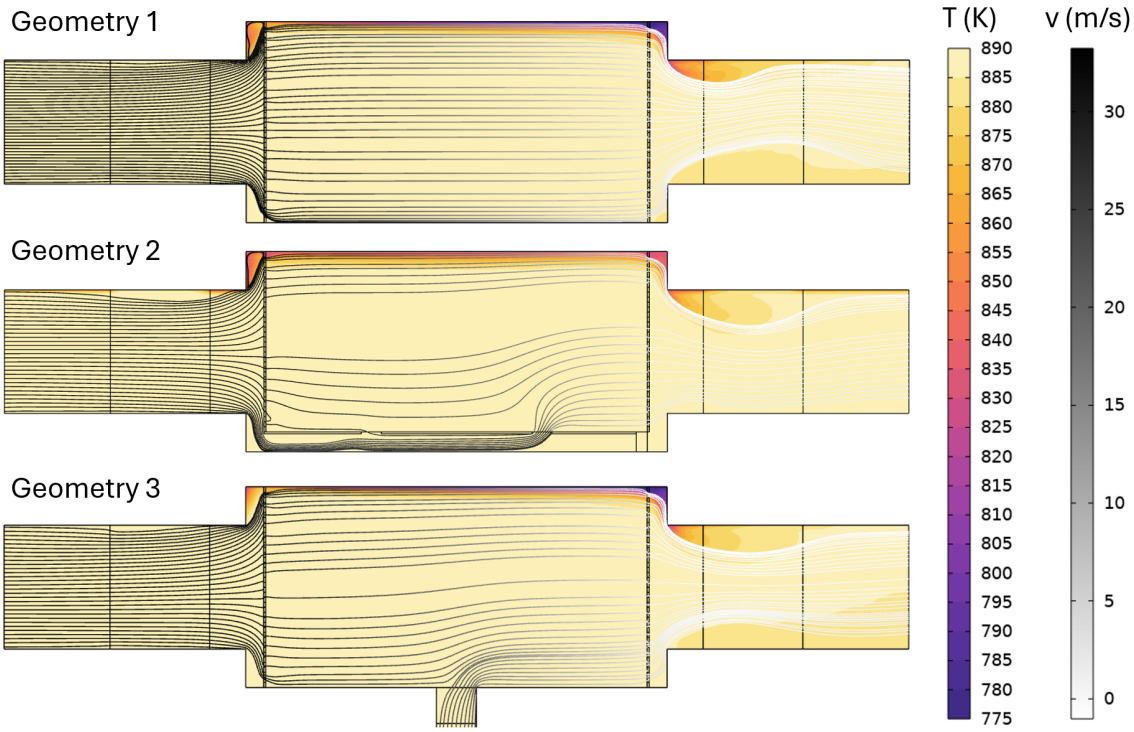

Figure 5.2: Temperature contours (K) and velocity field streamlines (m/s) obtained with the three geometric models after 20 hours of charging, for an inlet air flow rate of 1200 L/min at 890 K.

From the observation of Figures 5.1 and 5.2 it is possible to see that all three geometries present a similar trend. In fact, after 10 hours of charging, it can be verified that the packed bed presents temperatures between 880 and 890 K, except the third geometry, in which temperatures of 870 K can be identified in some regions. In contrast, after 20 hours of charging, all three geometries present a uniform distribution of temperature in the entire extension of the packed bed, achieving the desired temperature of around 890 K. However, while temperature contours effectively illustrate spatial distribution, they do not serve as a standalone metric for quantifying the overall thermal efficiency of the packed bed.

For this reason, the total stored thermal capacity was integrated within COMSOL to quantify performance along with the temperature contours, according to equation 4.14. The resulting profiles for the three design configurations are compared in Figure 5.3 and the values of the stored heat within the bed after 5, 10, 15 and 20 hours of charging are presented in Table 5.1 for a more detailed analysis.

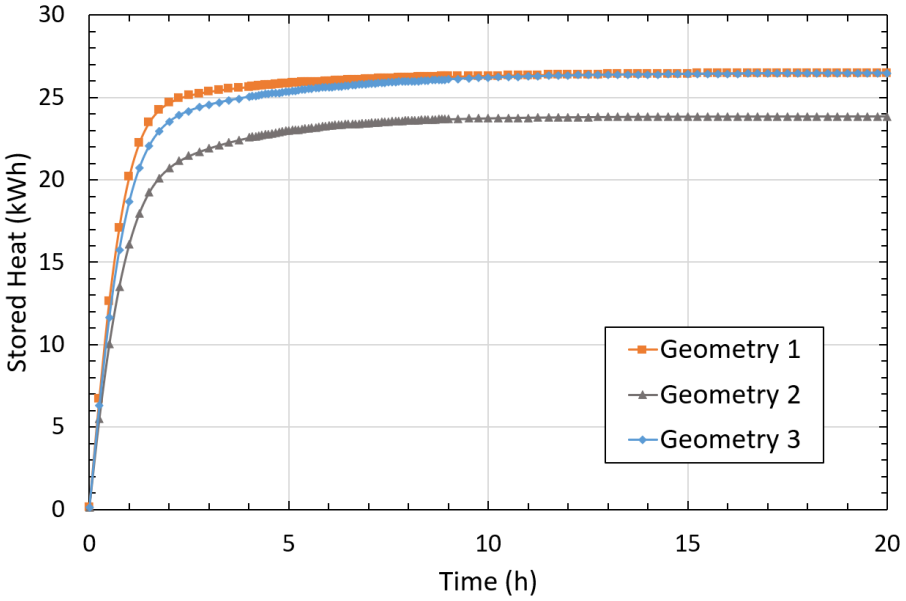

Figure 5.3: Comparison of the heat storage capacity (kWh) throughout time (h) for the three geometries tested.

Table 5.1: Heat Stored after 5, 10, 15 and 20 hours of charging for different geometries tested

	Stored Heat (kWh)		
Time (h)	Geometry 1	Geometry 2	Geometry 3
5	25.85	22.99	25.37
10	26.32	23.75	26.19
15	26.45	23.85	26.42
20	26.49	23.87	26.49

From the analysis of Figure 5.3 it can be seen that in all three geometries tested the storage heat capacity tends to increase with a high pace during the first hours of charging and tends to stabilize from the third hour.

In addition, the plot highlights that even though the second geometry tested presented a desirable spatial distribution of temperature, it was actually the geometry with the worst performance of the three as it is not able to store so much heat. One explanation for these results might be related to the fact that the introduction of air from the inlets below does not make up for the reduction in size of the porous medium and, in fact, led to worse results compared with the first and third geometries tested.

On the other hand, the first and the third geometries exhibit a similar behavior, with very close values during all the charging period. In Table 5.1 it is possible observe that, while during the first 15 hours of charging it is undeniable that the geometry 1 was able to store slightly more heat in comparison with the third geometry, after 20 hours of charging that is no longer true and the third geometry even surpasses the first one.

In order to study the potential of the third geometry, and to verify if it was the geometry that led to the optimal performance of the packed-bed, possible variations of the third geometry tested were also analysed. As a matter of fact, the two variations of the third geometry are identical to this one with the exception of the position of the secondary air inlet, which was positioned at a distance from the axis of the secondary inlet of the original third geometry of 0.06 m and 0.17 m, respectively, to the left. Figure 5.4 illustrates the spatial distribution of temperature alongside the packed bed, after 10 and 20 hours of charging time, for the three variations of the third geometry tested. For simplification, the original version of the third geometry tested was named "3a", while the other two variations were named "3b" and "3c".

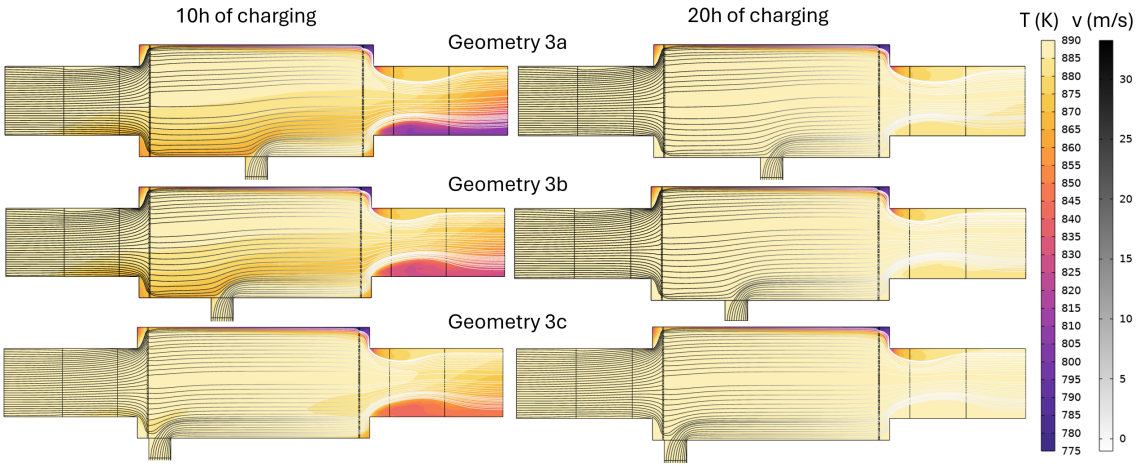

Figure 5.4: Temperature contours (K) and velocity field streamlines (m/s) obtained with the three versions of the third geometry after 10h (left side) and 20h of charging (right side).

From the observation of Figure 5.4, it can be observed that, while Geometries 3a and 3b show very similar temperature distributions after 10 hours of charging, with temperatures from 870 to 890 K within the porous medium, Geometry 3c clearly exhibits a better distribution of

temperature, with almost all of the extension of the porous medium achieving 890 K after the same time of charging. On the other hand, after 20h of charging period all three versions of the third geometry present a uniform temperature distribution achieving 890 K in all regions of the porous medium, similar to what was observed for geometries 1 and 2.

Similar to what was done for geometries 1, 2 and 3, the heat storage capacity was also computed for the other variations of the third geometries and it was possible to plot the heat stored (kWh) throughout charging time (h) for the five geometries. This plot is illustrated in Figure 5.5.

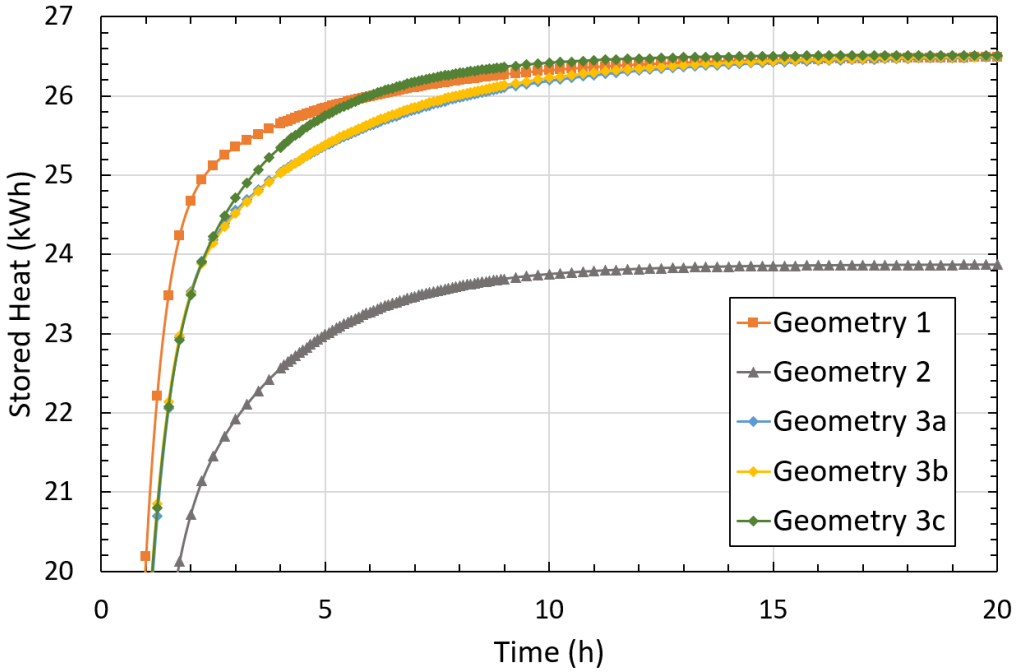

Figure 5.5: Comparison of the heat storage capacity (kWh_{th}) throughout time (h) for the five geometries tested.

From Figure 5.5, it can be observed that, apart from geometry 2, all the other geometries exhibit a similar behaviour and very close values. However, up to 5 hours of charging time, the geometry 1 has the highest heat storage capacity, but after this period geometry 3c is able to store more heat and, therefore, presents the most optimal performance during the charging phase.

Based on these results, it could be verified that geometry 3c demonstrated the best heat distribution and overall efficiency during the charging phase under similar boundary conditions and charge period, achieving a storage capacity of 26.5 kWh_{th} during the charging period and for the inlet conditions considered. Consequently, geometry 3c was selected as the standard model for all subsequent simulations.

5.2 Influence of inlet conditions in the performance of the packed-bed

The second set of simulations aimed to assess the impact of varying inlet conditions on the thermal performance of the packed-bed system. For this purpose, four simulation cases were considered, each corresponding to a different flow rate condition of inlet air. The flow rates adopted for each scenario are summarized in Table 5.2.

Table 5.2: Flow rates employed for each simulation case

	Flow rate through the main inlet (L/min)	Flow rate through the secondary inlet (L/min)	Total flow rate entering (L/min)
Case 1	1000	200	1200
Case 2	750	150	900
Case 3	500	100	600
Case 4	250	50	300

Evolution of the temperature profile across the packed-bed

In order to evaluate if there are significant temperature gradients within the packed-bed system, temperature plots as a function of resting time were also plotted for several points scattered across the packed-bed. Figure 5.6 illustrates the nine auxiliary points created to evaluate the packed-bed performance and Table 5.3 presents their correspondent coordinates.

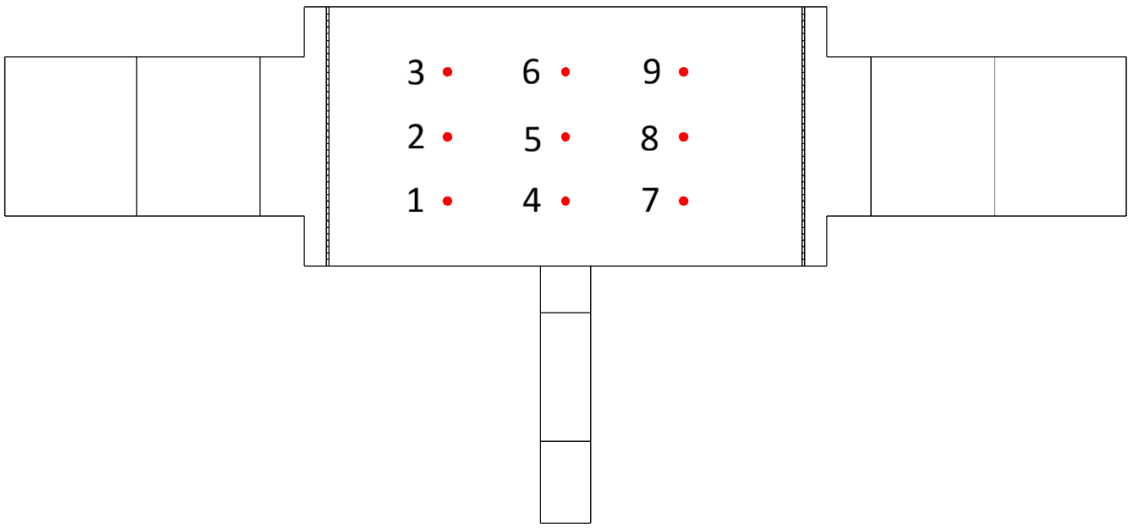

Figure 5.6: Nine auxiliary points positioned across the packed-bed.

Table 5.3: Coordinates of the auxiliary points

Points	Coordinates (m)
1	(-0.0955, -0.05025)
2	(-0.0955, 0)
3	(-0.0955, 0.05025)
4	(0, -0.05025)
5	(0, 0)
6	(0, 0.05025)
7	(0.0955, -0.05025)
8	(0.0955, 0)
9	(0.0955, 0.05025)

Figures 5.7 to 5.10 illustrate the evolution of temperature in different points of the packed-bed was plotted for points 1, 5 and 9 (Table 5.3).

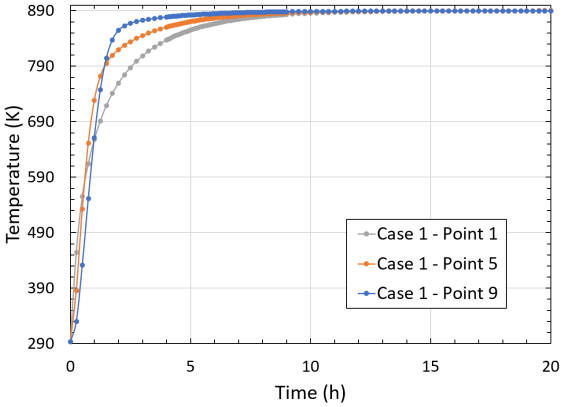

Figure 5.7: Temperature in points 1, 5 and 9 during charging for Case 1.

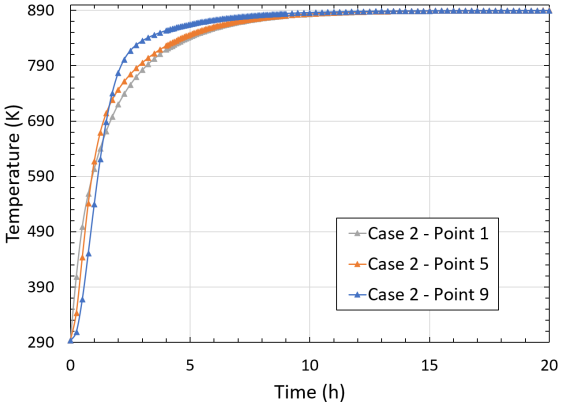

Figure 5.8: Temperature in points 1, 5 and 9 during charging for Case 2.

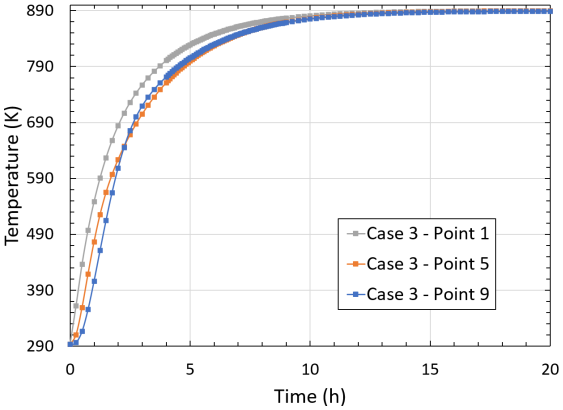

Figure 5.9: Temperature in points 1, 5 and 9 during charging for Case 3.

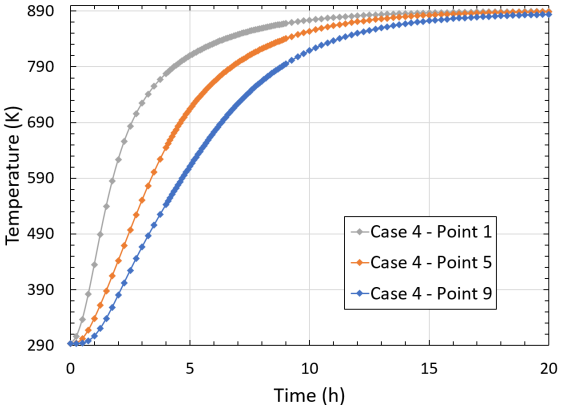

Figure 5.10: Temperature in points 1, 5 and 9 during charging for Case 4.

From Figures 5.7 to 5.10 it is possible to observe that, as expected, for every point evaluated and, therefore, for every point in the porous medium, the higher the total inlet flow rate, the faster the porous medium achieves and tends to the desired temperature.

In addition, it is possible to observe that for higher inlet flow rates, such as Cases 1 and 2, the point 9 exhibits higher temperatures comparing with points 5 and 9, whereas for Case 3 the temperatures verified in point 9 are comprehended between the ones verified in points 1 and 5, and for the lower flow rate, corresponding to Case 4, point 9 exhibits the lowest temperature values, followed by point 5 and finally point 1. This suggests that, for higher flow rates, the points located in the upper part of the bed and even though farthest from the main air inlet heat faster than the points located in the inferior part of the bed and closest to the inlet. At the same time, for lower flow rates, the heated air reaches faster the points closest to the main inlet and the lower part of the bed and takes longer to reach the points farthest from the bed, leading to a higher temperature gradient within the porous medium, as highlighted by Figure 5.10.

In this way, it is possible to conclude that for higher flow rates during the charging period the effects of the primary flow are more dominant, whereas for lower flow rates the effects of the secondary flow appear to be more significant.

Pressure drop

To evaluate the pressure drop across the packed-bed for each of the four charging cases considered, the pressure contour were extracted from COMSOL for each case, as illustrated in Figure 5.11. For each charging simulation, the pressure drop remains practically constant over time. The pressure drops obtained from the numerical simulations were then compared with those calculated through the direct application of the Ergun equation. The results of this comparison are presented in Table 5.4.

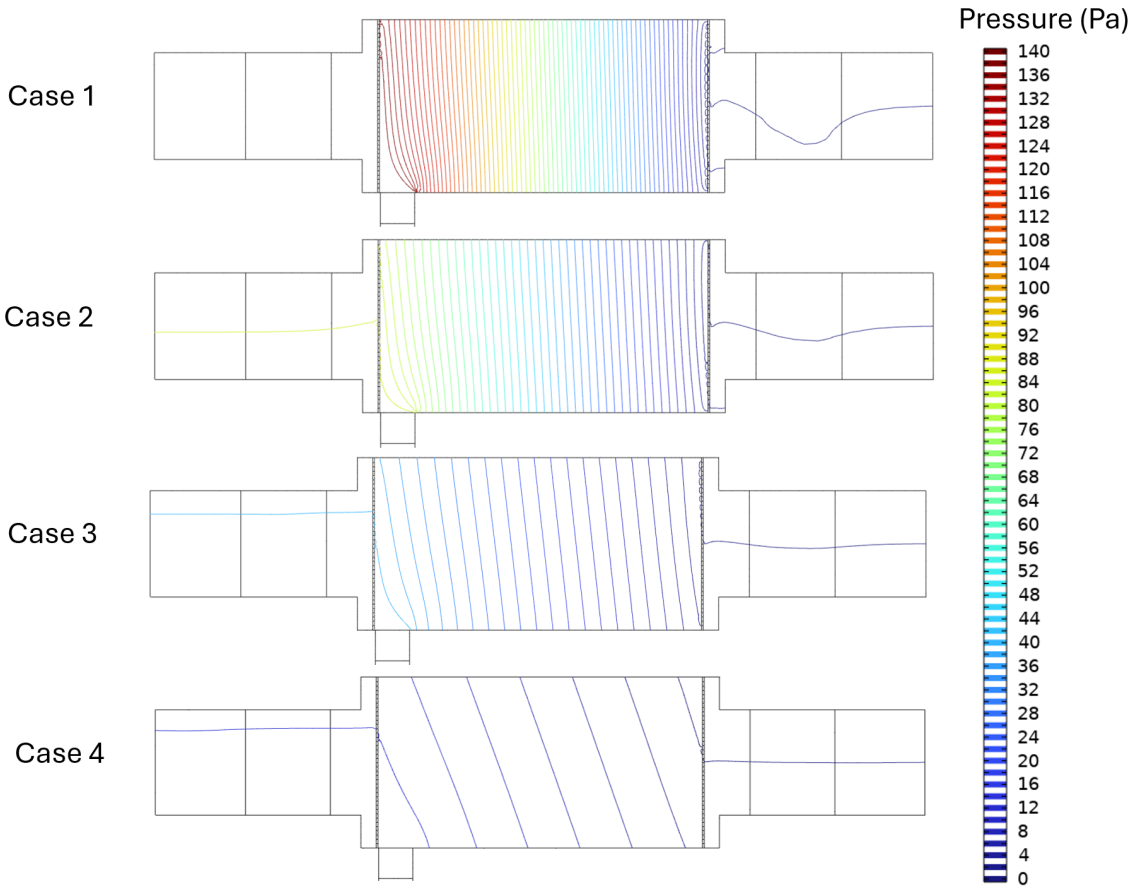

Figure 5.11: Pressure contours for the four charging cases considered.

Table 5.4: Comparison of the pressure drop obtained from the numerical simulations and through the Ergun equation for each charging case

	Pressure drop obtained from the simulations (Pa)	Pressure drop obtained through the Ergun equation (Pa)	Deviation (%)
Case 1	140	121.61	13.14
Case 2	84	75.16	10.52
Case 3	40	41.53	3.83
Case 4	12	11.99	0.08

The comparison of the results presented in Table 5.4 highlights that the pressure drops obtained from the COMSOL simulations and those calculated using the Ergun equation are quite in agreement. Although a maximum deviation of 13.14 % can be observed, they remain within an acceptable range, supporting the reliability of the developed numerical model and contributing to its validation. In fact, these deviations are likely related to the approximations associated with the extraction of pressure values from the contour plots shown in Figure 5.11, as well as to the assumptions adopted in the analytical calculation. In particular, the dynamic viscosity and density of the HTF were assumed to remain constant and were evaluated at a reference temperature of

500 °C, whereas these properties vary throughout the packed-bed due to the temperature gradients during operation.

5.3 Evolution of the temperature contours in the packed-bed during resting phase

In order to study the performance of the packed-bed system during the discharge phase, the temperature contours after 1, 2, 5, 8 and 10 hours of resting time after each charging case investigated previously were analysed. For the four charging cases evaluated identical contours for the resting phase were obtained since, for all of them, after 20 hours of charging the achieved temperature conditions were the same. For this reason, the temperature contours after 1, 2, 5, 8 and 10 hours of resting time are presented in Figure 5.12 only for one case (case 4).

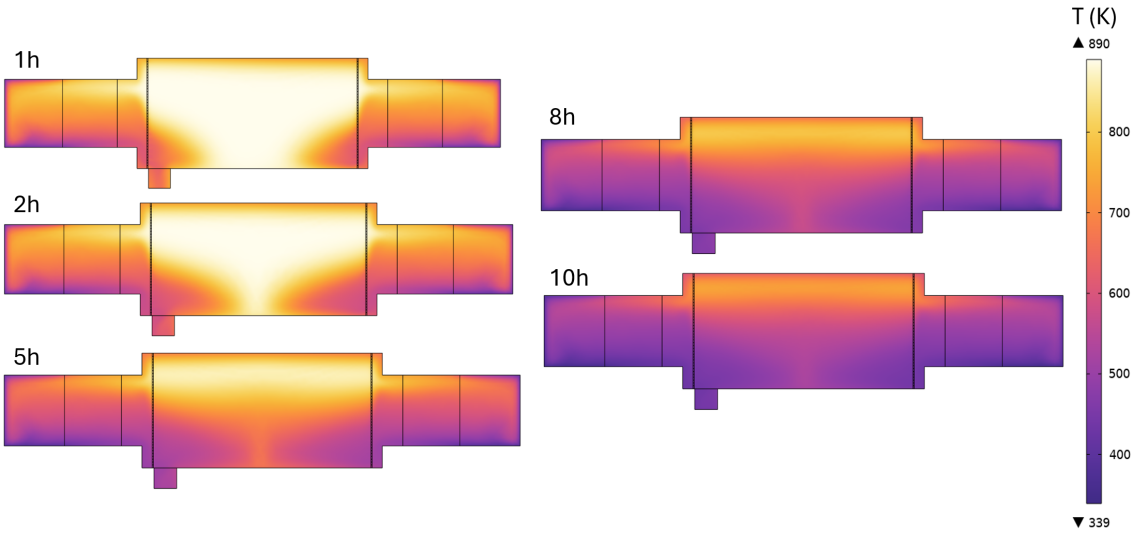

Figure 5.12: Temperature contours (K) during resting period after 1, 2, 5, 8 and 10 hours of charging.

In Figure 5.12 it is possible to observe that, during resting time, heat is lost first at the lower part of the packed-bed, near the lateral walls, and progressively it is lost also in the points located in the upper part of the bed.

To complement the results obtained with the temperature contours, the temperature in each of the 9 points defined earlier was also collected throughout time, during a period of 10 hours of resting, using as inputs the outputs of charging simulations for the cases 1 to 4 studied previously. Since these four charging cases achieved the same temperature conditions after the period of 20 hours of charging, the average temperature in each instant in time in each of the 9 points is plotted in Figure 5.13, whereas the maximum and average standard deviation for each point is presented in Table 5.5.

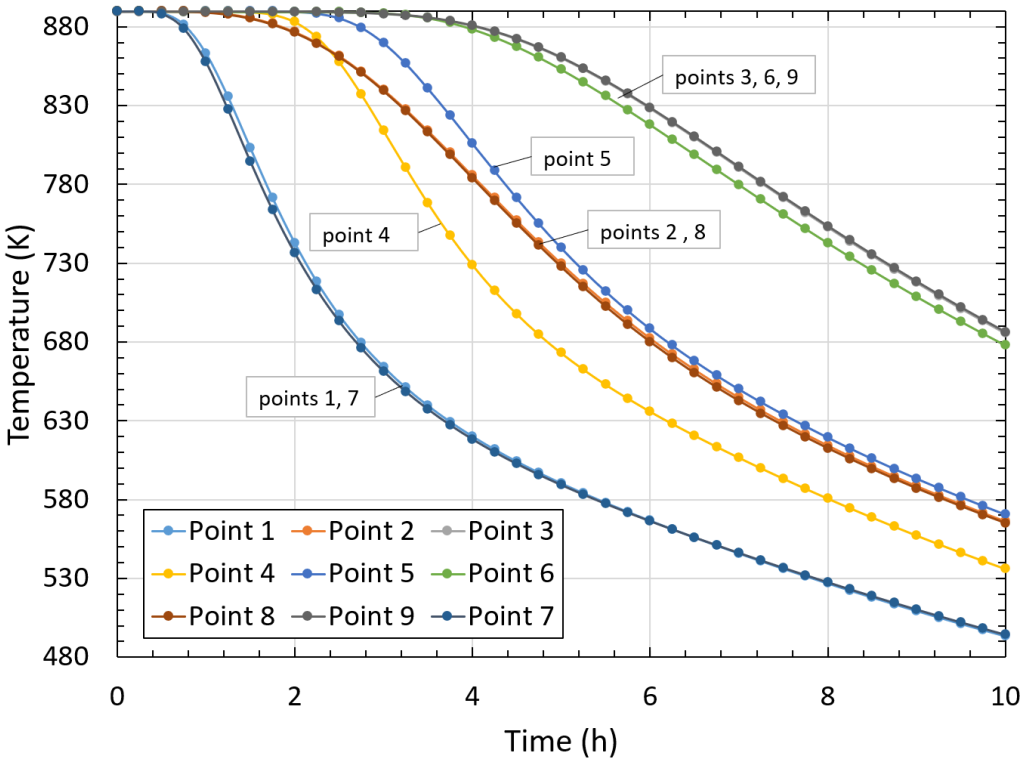

Figure 5.13: Evolution of temperature (K) in 9 different points of the packed-bed during resting period.

Table 5.5: Maximum and average standard deviation verified in each point.

Point	Max. St. Deviation (K)	Avg. St. Deviation (K)
Point 1	2.59	1.16
Point 2	4.31	2.43
Point 3	4.60	2.41
Point 4	7.17	2.89
Point 5	5.63	2.78
Point 6	4.32	2.48
Point 7	6.08	2.30
Point 8	4.50	2.64
Point 9	4.27	2.42

From the analysis of Figure 5.13 it is possible to observe some trends. In fact, independently of the charging case that preceded the resting phase (the deviations from the average are minimal according to Table 5.5), it can be seen that the temperature in each point decreases throughout resting time and, thereby, the performance of the system deteriorates fast despite the high number of insulation layers.

In points 1 and 7 the temperature starts decreasing after 1 hour of resting and continues at a high pace, totalizing a loss of around 400 K during the resting period of 10 hours. At the same

time, points 2, 4, 5 and 8 exhibit a more intermediate temperature evolution, with their temperature starting to decrease after 2 hours of charging, and totalizing a loss of around 300 K during the 10 hours of resting. Finally, in points 3, 6 and 9 is possible to identify the highest temperatures throughout the resting time, only presenting a decrease in temperature after 4 hours of resting and losing in total only 200 K during the 10 hours of resting.

These observations suggest that the heat is better kept at the upper part of the packed-bed, likely due to the high number of insulation layers above the storage medium. On the other hand, the points in the lower part of the bed lose heat at a faster rate, in particular the points closer to the lateral walls, likely due to the heat losses due to forced convection near the vertical walls of the system. Therefore, these results are in accordance with the temperature contours illustrated in Figure 5.12.

Furthermore, the transient behavior of the packed-bed system during the resting phase provides a clear depiction of thermocline degradation and front smearing within the porous domain. At the begining of the resting period, the fluid and solid domains exhibit a highly stratified thermal profile, characterized by a sharp, nearly vertical temperature gradient that distinctly separates the hot and cold zones of the bed. However, as the idling phase progresses in the absence of convective fluid flow, the localized spatial temperature profiles display a distinct structural shift. Driven by internal conduction through the stagnant air and solid EAF slag matrix, alongside axial thermal dispersion mechanisms, heat naturally migrates from the upper high-temperature region to the lower cold region. Consequently, the initial stratified temperature distribution gradually flattens and stretches over time, assuming a smooth, elongated S-shaped curve. This widening of the transition zone constitutes the physical and visual manifestation of front smearing. Quantifying the rate at which this thermal stratification decays during the resting phase is crucial, as it defines the loss of thermal exergy over time. These results demonstrate that prolonged standby periods directly broaden the thermocline layer, which ultimately compromises the exit temperature stability during the subsequent discharging phase.

Chapter 6

Techno-Economical Analysis

6.1 Model formulation and assumptions

To evaluate the feasibility of using EAF slag as an alternative to conventional packed-bed TES materials, a concise Techno-Economic Analysis (TEA) was performed. The evaluation was conducted using MATLAB software [55], adapting established computational frameworks developed at the DTU Energy Department to ensure reliable cost predictions for the specific configuration investigated in this study. The complete base MATLAB script used for this analysis is presented in Appendix A. To analyse the influence of individual parameters on the resulting economic indicators, the original code was modified to enable the evaluation of their variation with respect to the selected parameter.

It should be noted that, in order to compare the relevant economical parameters for different TES materials and since different materials have different storage capacities, a "reverse engineering" approach was adopted. In this way, for a fixed storage capacity, the necessary volume of storage material is computed and many of the variables in the code, necessary to compute economical parameters, depend on the required volume of storage material.

General considerations

To carry out this TEA, some inputs had to be considered. Air property interpolant functions the were imported from a .mat data file [56]. The thermophysical properties of the different TES materials considered in this analysis were taken from Table 3.1, and the respective unitary costs were taken either from the literature or websites and are presented in Table 6.1. The unitary costs of steel and the insulation materials are also presented in the same table.

Table 6.1: Unitary cost of the materials used in the TEA

Material	Unitary cost (USD /m^3)	Reference
EAF slag	118.63	[57]
Swedish diabase	294.75	[3]
Concrete	174.65	[58]
Common brick	250	[59]
Coal bottom ash	45.61	[60]
MSWI fly ash	44.34	[40]
Steel	42354	[61]
Vermiculite	2000	[62]
Superwool	800	[62]

In addition, the packing fraction was considered equal to 0.65, in accordance with the porosity of 0.35 that was also considered in COMSOL simulations. In this way, the effective density of each of the TES materials is equal to the product of the packing fraction for its density.

Regarding the operation of the bed, the minimum and maximum temperatures of the porous medium during the charging phase were considered equal to 20 and 617 °C, respectively. Additionally, it was considered that each cycle of operation of the packed-bed comprehends an 8 h charging period followed by an 10 h discharging period, and an efficiency of 90 % was considered for both processes. Furthermore, it was considered that the packed-bed performs one complete cycle per day and operates during 365 days of the year.

CAPEX

The Capital Expenditure (CAPEX) associated to the packed-bed system was calculated using equation 6.1 [61]:

$$CAPEX = \sum_{i=1}^{N_{mat}} c_i V_i \tag{6.1}$$

where N_{mat} is the number of materials that make up the packed-bed system, c_i are the unitary costs of the materials that make up the system (USD/m^3) and V_i is the volume of each material (m^3).

Therefore, it was necessary to determine the volume of storage material, the volume of each insulation material, the volume of steel and the volume of the foundation.

First of all, the volume of storage was determined using equations 4.14 and 4.15, for a given energy storage capacity.

The volume of steel, vermiculite and superwool insulation were determined using relations with the volume of storage material which were taken from the geometric model in COMSOL Multiphysics. In order to simplify the calculations, the geometric model corresponding to Geometry 1 was employed. These relations are presented in Table 6.2, as well as the density values considered for the calculation of the foundation volume.

Table 6.2: Superwool, vermiculite and steel ratios with the volume of TES and their density (kg/m^3)

Material	$V_{material}/V_{storage}$	Density (kg/m^3)
Superwool	1.173	96
Vermiculite	2.18	80
Steel	0.10	7850

Finally, the foundation of the system was assumed to be a rectangular base made of concrete and, in order to determine its volume, it was necessary to determine the area of this base that would support the loads involved, and multiply it by a certain depth, that was considered to be equal to 0.75 m. The area of the foundation can be determined by:

$$A_{foundation} = P/q_{allow} \tag{6.2}$$

with

$$P = \left(\sum_{i=1}^{N_{mat}} V_i \rho_i \right) \times SF \tag{6.3}$$

where q_{allow} is the allowable soil bearing pressure (kN/m^2) which was considered equal to 100 kN/m^2, N_{mat} is the number of materials that make up the packed-bed system, ρ_i is the density of each material (kg/m^3) , and SF is a safety factor which was considered equal to 2.

OPEX

The yearly Operation and Maintenance Costs (OPEX) associated to this the packed-bed system was calculated using equation 6.4 adapted from [61]. This OPEX is the operational cost evaluated as the sum of the operation and maintenance costs, assumed equal to 2 % of the anual CAPEX [61], and the electricity costs for circulating the HTF through the TES units during both charge and discharge.

$$OPEX = 0.02 \cdot CAPEX_{anual} + E_{pump} c_{el} \times 365 \tag{6.4}$$

With

$$\begin{aligned} E_{pump} &= E_{pump_{ch}} + E_{pump_{disch}} \\ &= \left[\int_0^{t_{ch}} \frac{A N_{TES} G_{ch}(t) \Delta p_{ch}(t)}{\rho_f} dt + \int_0^{t_{disch}} \frac{A N_{TES} G_{disch}(t) \Delta p_{disch}(t)}{\rho_f} dt \right] \frac{1}{\eta_{compr}} \end{aligned} \tag{6.5}$$

Where c_{el} is a fixed electricity cost, which was considered equal to 0.11 USD/kWh$_{el}$; A is the TES cross-sectional area (m^2); N_{TES} is the number of TES units; G_{ch} and G_{disch} are the HTF mass flow rates per unit cross-section area during charge and discharge, respectively (kg/(m^2·s)); Δp_{ch} and

Δp_{disch} are the pressure drops induced by the TES unit during charge and discharge, respectively; ρ_f is the fluid density (kg/m^3); and η_{compr} is the air circulator efficiency, assumed equal to 0.95 [61].

To determine the cross-sectional area of the porous domain, two approaches have been tested, and the obtained results will be discussed later.

In the first approach, the original dimensions of the COMSOL model were taken and a linear scaling factor was applied. However, it should be noted that for these ratios, the automatic depth of the model assigned by COMSOL to 2D models (the default setting is a depth of 1 m) was not considered, and instead it was considered that the depth of the porous domain is equal to its height, so that the cross-sectional area of this domain is a square. The equations employed to calculate the cross-sectional area and the length of the porous domain are presented in equations 6.6 to 6.8:

$$k = \sqrt[3]{\frac{V_{storage_{new}}}{V_{storage_{orig}}}} = \sqrt[3]{\frac{V_{storage_{new}}}{S_{orig} \times S_{orig} \times L_{orig}}} \tag{6.6}$$

$$S_{new} = k \times S_{orig} \tag{6.7}$$

$$L_{new} = k \times L_{orig} \tag{6.8}$$

where k is a linear scaling factor; $V_{storage_{orig}}$ is the volume of the porous medium from the COMSOL model; S_{orig} and L_{orig} are the side and length dimensions of the porous domain taken from the COMSOL model and are equal to 0.201 m and 0.382 m, respectively; and S_{new} and L_{new} are the new side and length dimensions of the porous medium calculated from the obtained required volume of storage.

In the second approach, the cross-sectional area of the porous domain has been fixed to 20 m^2 and the its length was calculated simply dividing the storage volume by the cross-sectional area ($L = V_{storage}/A$).

The mass flow rates per unit cross-section area G_{ch} and G_{disch} can be obtained dividing the mass flow rates of the HTF during charge and discharge, determined using equations 6.9 and 6.10 [61], by the cross-sectional area.

$$\dot{m_{ch}} = \frac{E_{TES}}{\Delta h|_{T_{min}}^{T_{max}} t_{ch} N_{TES} \eta_{ch}} \tag{6.9}$$

$$\dot{m_{disch}} = \frac{E_{TES}}{\Delta h|_{T_{min}}^{T_{max}} t_{disch} N_{TES} \eta_{disch}} \tag{6.10}$$

Where E_{TES} is the TES energy capacity (J); $\Delta h|_{T_{min}}^{T_{max}}$ is the maximum fluid enthalpy change (J/kg); t_{ch} and t_{disch} are the charge and discharge phase duration (s); N_{TES} is the number of TES units, in this case, 1; and η_{ch} and η_{disch} are the preliminary charging and discharging efficiencies.

For an ideal gas and when the specific heat at constant pressure is assumed to be constant over the given temperature range, the following approximation can be made:

$$\Delta h|_{T_{min}}^{T_{max}} = C_{p_f} \cdot (T_{max} - T_{min}) \tag{6.11}$$

where C_{p_f} is the specific heat of the HTF that is considered constant.

Finally, the pressure drop during charging and discharging phases was determined using Ergun's equation:

$$\Delta p_{ch} = \left(\frac{150\,\mu\,(1-\varepsilon_p)^2}{D_p^2\,\varepsilon_p^3} v_{ch} + \frac{1.75\,\rho_f\,(1-\varepsilon_p)}{D_p\,\varepsilon_p^3} v_{ch}^2 \right) L \tag{6.12}$$

$$\Delta p_{disch} = \left(\frac{150\,\mu\,(1-\varepsilon_p)^2}{D_p^2\,\varepsilon_p^3} v_{disch} + \frac{1.75\,\rho_f\,(1-\varepsilon_p)}{D_p\,\varepsilon_p^3} v_{disch}^2 \right) L \tag{6.13}$$

where L is the length of the porous domain (m); μ is the fluid dynamic viscosity calculated through Sutherland's equation and equal to 2.9905e-05 Pa·s; ρ_f is the HTF density, obtained through properties functions available in MATLAB (kg/m^3); ε_p is the porosity of the porous medium, equal to 0.35; D_p is the pellet diameter, considered equal to 0.015 m; and v_{ch} and v_{disch} is the superficial velocity of the fluid during charging and discharging, respectively (m/s), which are obtained dividing the mass flow rates of the HTF during charge and discharge by the cross-sectional area of the porous domain and the density of the HTF.

Total Cost

Knowing the CAPEX and the yearly OPEX associated withe the packed-bed system, it is possible to calculate the total cost:

$$Total\ Cost = CAPEX + \sum_{n=1}^{N_{op}} \frac{OPEX}{(1+r)^n} \tag{6.14}$$

where N_{op} is the TES operational life, considered equal to 20 years; r is the discount rate, considered equal to 7 % (same as [61]).

LCOS

To calculate the LCOS, the equation presented in [61] was used:

$$LCOS = \frac{CAPEX + \sum_{n=1}^{N_{op}} \frac{OPEX}{(1+r)^n}}{\sum_{n=1}^{N_{op}} \frac{E_{NET}}{(1+r)^n}} \tag{6.15}$$

where N_{op} is the TES operational life, considered equal to 20 years; r is the discount rate, considered equal to 7 % (same as [61]); and E_{NET} is the net electricity output recoverable from the TES unit.

Since the packed-bed system itself stores and provides thermal energy, in order to evaluate the net electrical production a conversion efficiency of a typical Rankine cycle, η_{cycle}, considered to

be equal to 38 % [61] has been applied. In this way, the net electricity output recoverable from the TES unit in each cycle can be calculated:

$$E_{NET} = \eta_{cycle} \cdot E_{TES_{out}} \tag{6.16}$$

where $E_{TES_{out}}$ is the direct thermal energy output from the TES unit.

In turn, the thermal energy output of each cycle was calculated through equation 6.17 [61]:

$$E_{TES_{out}} = \int_0^{t_{disch}} AN_{TES} G_{disch}(t) C_{p_f}(t) [T_{f_{out}}(t) - T_{f_{in}}] \, dt \tag{6.17}$$

where A is the TES cross-sectional area; N_{TES} is the number of TES units; G_{disch} is the HTF mass flow rate per unit cross-section area during discharge; C_{p_f} is the specific heat of the HTF; and $T_{f_{out}}$ and $T_{f_{in}}$ are the temperatures of the air leaving and entering the unit during discharge.

It should be noted that, in order to simplify calculations in MATLAB, the specific heat capacity of the HTF was considered to be constant and equal to its value for 500°C, and the temperature of the air leaving the packed-bed during discharge was considered to be constant and equal to 82 % of the maximum temperature verified in the porous medium.

NPV

In order to assess whether future amounts of money are worth more or less than the cost of an investment made in the present for the packed-bed system, the Net Present Value (NPV) was calculated using equation 6.18.

$$NPV = -CAPEX + \sum_{n=1}^{N_{op}} \frac{CF_n}{(1+r)^n} \tag{6.18}$$

where N_{op} is the TES operational life, considered equal to 20 years; r is the discount rate, considered equal to 7 % (same as [61]); and CF_n is the cashflow verified in year n, i.e., the difference between sales and the OPEX costs in that year. For the purpose of the economic calculations it is also assumed that all the electricity output delivered by the packed-bed system is sold at a fixed selling price throughout the years.

Payback period

The number of years required for the project cash flows to offset the initial investment corresponds to the payback period. The simple payback, which disregards the time value of money, can be determined through equation 6.19 [63], where $\overline{CF}$ is the uniform net cash flow.

$$Payback\ Period = \frac{CAPEX}{\overline{CF}} \tag{6.19}$$

Overall efficiency

The TES overall efficiency is calculated through equation 6.20 [61]. This efficiency is defined as the ratio between the energy outflow $E_{TES_{out}}$ and the sum of inlet energy $E_{TES_{in}}$ and energy spent to overcome the HTF pressure drop during both charge $E_{pump_{ch}}$ and discharge phase $E_{pump_{disch}}$:

$$\eta_{th_{ovr}} = \frac{E_{TES_{out}}}{E_{TES_{in}} + E_{pump_{ch}} + E_{pump_{disch}}} \tag{6.20}$$

6.2 Techno-economic results

This section presents the key findings regarding the influence of several technical and economical parameters in the economical performance parameters, in particular, in the LCOS.

Influence of the cross-sectional area of the porous domain

In order to understand, in a first instance, the influence of the approach to calculate the cross-sectional area required for each material to achieve the desired energy storage capacity, the energy storage capacity was varied from 50 to 250 MWh_{th} and the LCOS was computed for each energy storage capacity value and for each material. The results obtained using the first and second approaches for the cross-sectional area of the porous domain, corresponding to scaling the area with the storage volume and fixing the cross-sectional area at 20 m^2, respectively, are plotted in Figures 6.1 and 6.2, respectively. It should be noted that the economic model developed in MATLAB does not account for the scale effect in production.

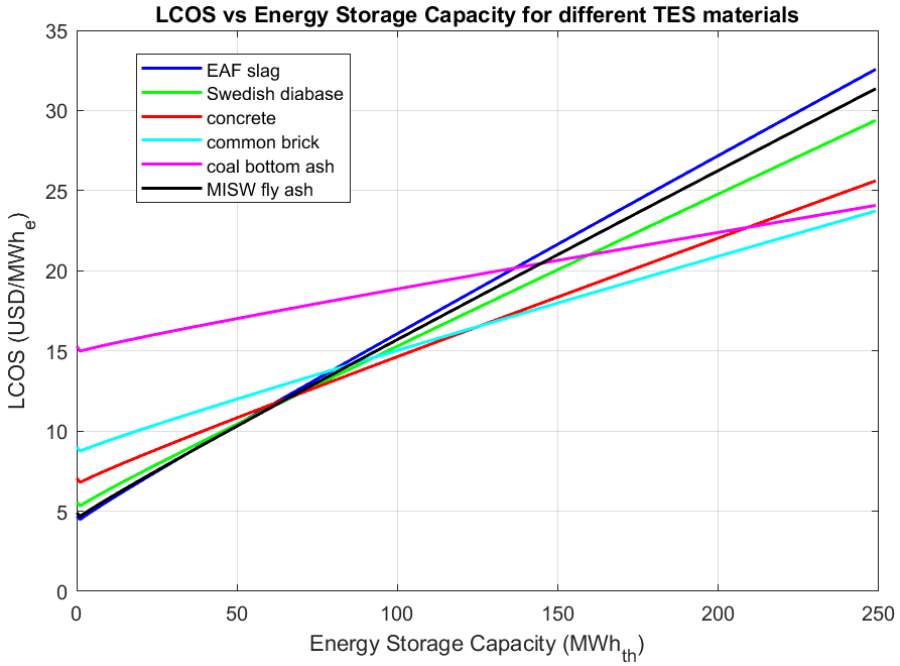

Figure 6.1: LCOS (USD/MWh_e) evolution with the energy storage capacity (MWh_{th}) for different TES materials using the first approach for cross-sectional area calculation.

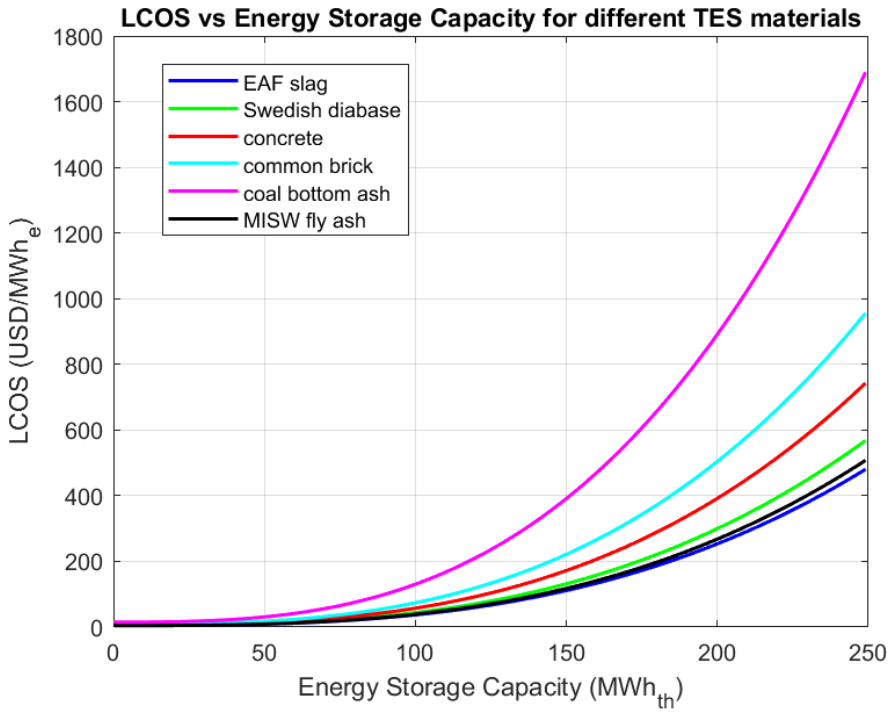

Figure 6.2: LCOS (USD/MWh$_e$) evolution with the energy storage capacity (MWh$_{th}$) for different TES materials using the second approach for cross-sectional area calculation.

The LCOS plots obtained for the two geometric approaches show that the way the cross-sectional area of the porous domain is defined has a decisive impact on the techno-economic performance of the packed-bed system.

In the first approach, since the porous domain preserves geometric similarity (both the side length and the bed length grow proportionally with the cube root of the storage volume), the LCOS values remain within a relatively narrow and realistic range, and the differences between materials are moderate. The trends are smooth, and LCOS increases with energy storage capacity in a way that is consistent with higher investment and operating costs for larger systems. Furthermore, although this approach slightly penalizes materials with higher volumetric heat capacities, such as EAF slag, because their smaller required storage volumes lead to smaller cross-sectional areas and therefore higher superficial velocities, which the Ergun equation strongly penalizes through increased pressure drops, the overall effect remains moderate and does not impose excessively high penalties on any specific material.

In contrast, the second approach fixes the cross-sectional area to a constant value, allowing the length of the porous domain to grow linearly with its volume. This leads to very long packed-beds for materials with low volumetric heat capacity, which according to Ergun equation significantly increases the pressure drop and, consequently, the pumping energy required to circulate the HTF. The LCOS curves in this case reach much higher values and diverge significantly between materials, with materials with lower densities and specific heat capacities showing very high LCOS at higher energy storage capacities. This behaviour suggests that the second approach for the cross-

sectional area calculation is highly sensitive to material properties and can easily generate geometries that are not realistic from an engineering point of view, in particular in terms of pressure drop and mechanical design (and feasibility of construction). For example, for an energy storage capacity of 200 MWh_{th}, the second approach would generate a geometry with a cross-sectional area and a length of the porous medium equal to 20 m^2 and 29 m, respectively, contrasting with much more realistic dimensions, 45.33 m^2 and 12.8 m, respectively, using the first approach.

In conclusion, taking into account the results from both plots, the first approach can be regarded as the more appropriate baseline between the two approaches analysed in this section, as it respects the original COMSOL geometry, maintains geometric similarity and avoids extreme bed lengths, resulting in LCOS values that are more compatible with practical TES designs. The second approach, although less realistic as a design strategy, is still valuable as a sensitivity analysis tool, showing how strongly LCOS can increase if the cross-sectional area is constrained and porous domain length is allowed to grow without realistic engineering limits.

Finally, still referring to Figure 6.1 it can be concluded that, in comparison with the other conventional TES materials, using EAF slag as the storage material in packed-beds is only competitive in large scale applications up to 50 MWh_{th}. This capacity scale matches the diverse high-temperature waste heat recovery and thermal management demands found across a wide spectrum of industrial sectors. In heavy industries, it aligns perfectly with the high-temperature heat (400-1000°C) recovery needs of medium-sized plants, such as in glass manufacturing (e.g., annealing and melting furnaces), ceramic firing, non-ferrous metal casting [64]. Within these boundaries, utilizing a plant's own metallurgical byproducts like steel slag as a solid storage medium provides an ideal circular economy synergy for batch thermal leveling [65]. Furthermore, the upper bound of 50 MWh_{th} matches the waste heat recovery and continuous steam demands found in large-scale food and beverage operations, such as industrial baking, spray drying, and multi-effect evaporation [66], as well as continuous thermal sterilization and distillation loops in pharmaceutical manufacturing [67]. Ultimately, at these capacities, a solid-media packed-bed configuration represents a highly versatile and economically viable pathway for peak-load shifting and industrial decarbonization across both heavy and light manufacturing sectors [68].

Comparison between using one single TES unit and multiple units

To understand if using multiple TES units in parallel instead of one single unit would to store energy would be more profitable, another approach was tested in MATLAB. Instead of fixing the number of TES units to one, in this new approach, for each required energy storage capacity, the required volume of storage was computed and all the dimensions of the porous domain were calculated using the scaling factor of equation 6.6 and the length of the porous domain was fixed to a maximum upper bound, so that when the length of the bed exceeded that upper bound new unit(s) would be employed until the length of the porous domain in all units was within the maximum upper bound. Figures 6.3, 6.4, 6.5 and 6.6 show the evolution of the total required fan power per cycle, yearly OPEX, CAPEX and LCOS with the energy storage capacity, respectively, for the first approach (single unit scaling every dimension of the porous domain) and the third approach

(using multiple TES units and limiting the maximum length of the porous domain to 2 m, 5 m and 10 m). The second approach (fixing the cross-sectional area of the porous domain to 20 m^2) was not included in these plots since the results obtained with these approach strongly deviate from the results obtained using different approaches, and since it was intended to compare the economical advantage of using multiple TES units in comparison with the most optimal results achieved using one single TES unit, which, until this point, was accomplished with the first approach. The computed results for all these approaches can also be seen in detail in the Tables B.1 to B.5 presented in Appendix B.

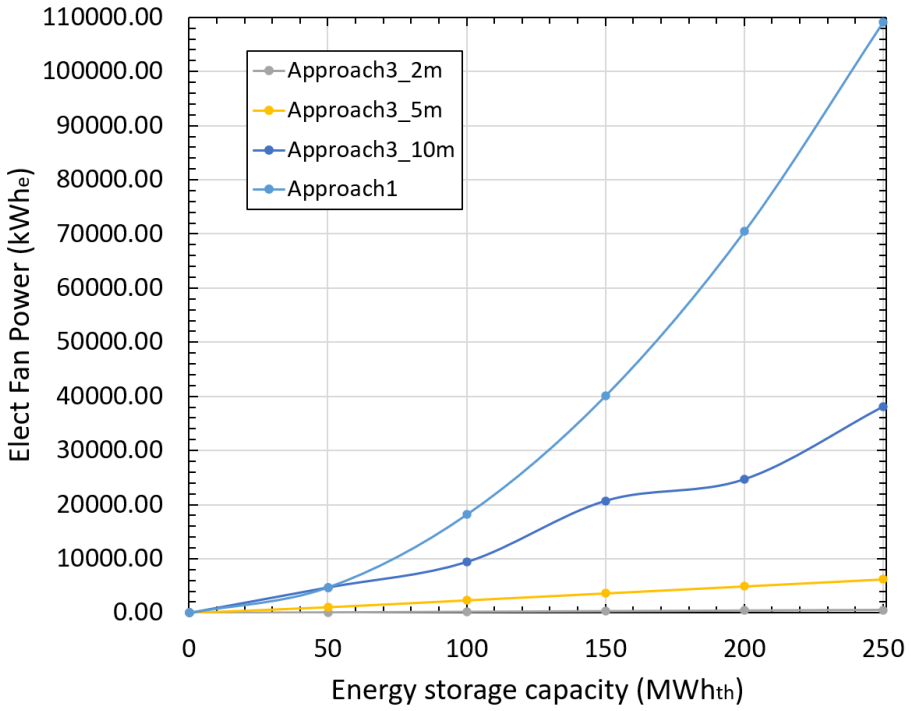

Figure 6.3: Electric fan power consumption (kWh_e) evolution with the energy storage capacity (MWh_{th}) for the first and third approaches.

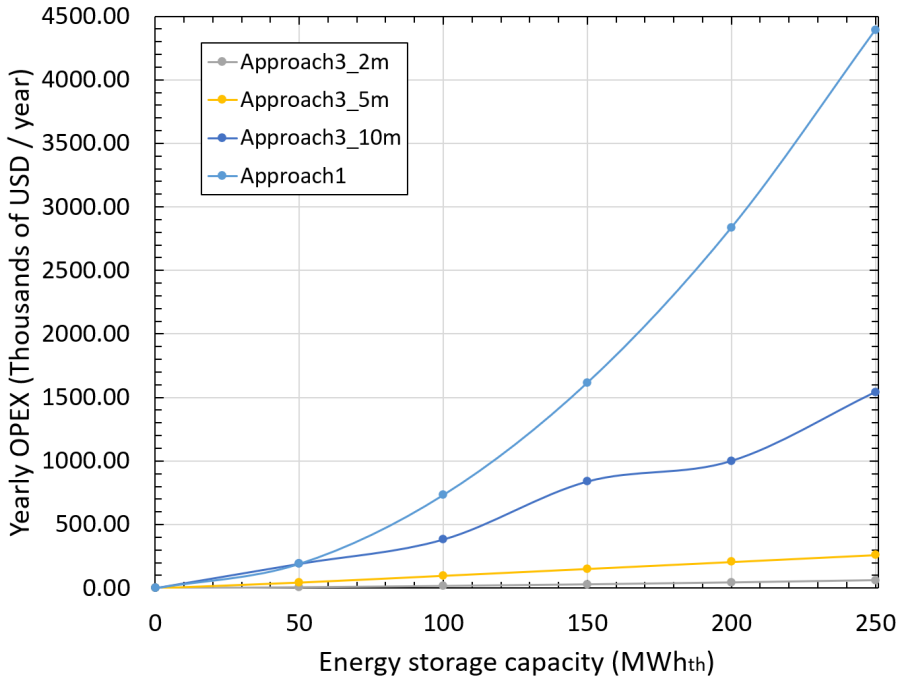

Figure 6.4: Yearly OPEX (Thousands of USD) evolution with the energy storage capacity (MWh_{th}) for the first and third approaches.

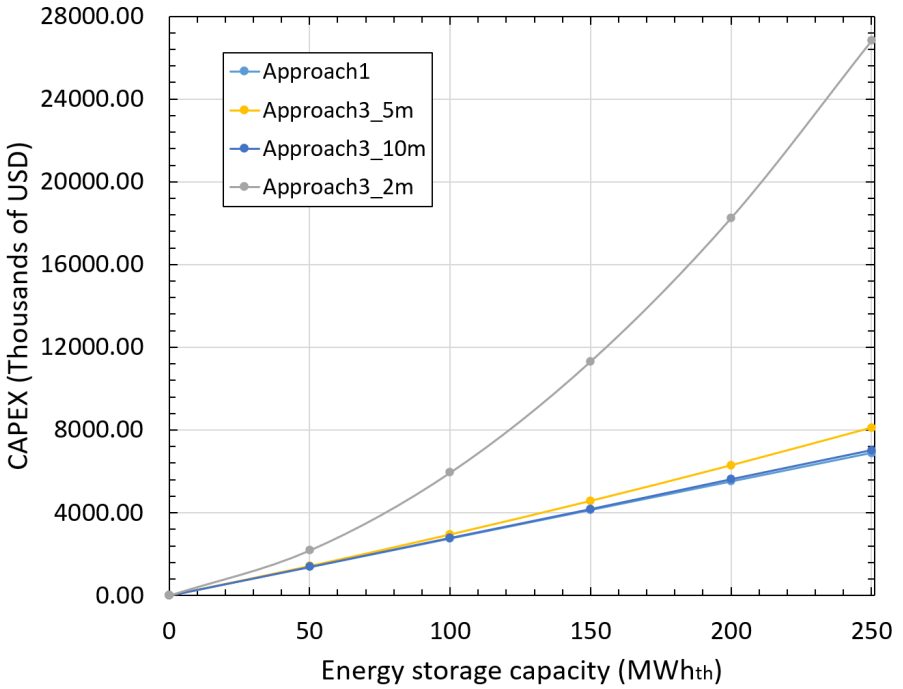

Figure 6.5: CAPEX (Thousands of USD) evolution with the energy storage capacity (MWh_{th}) for the first and third approaches.

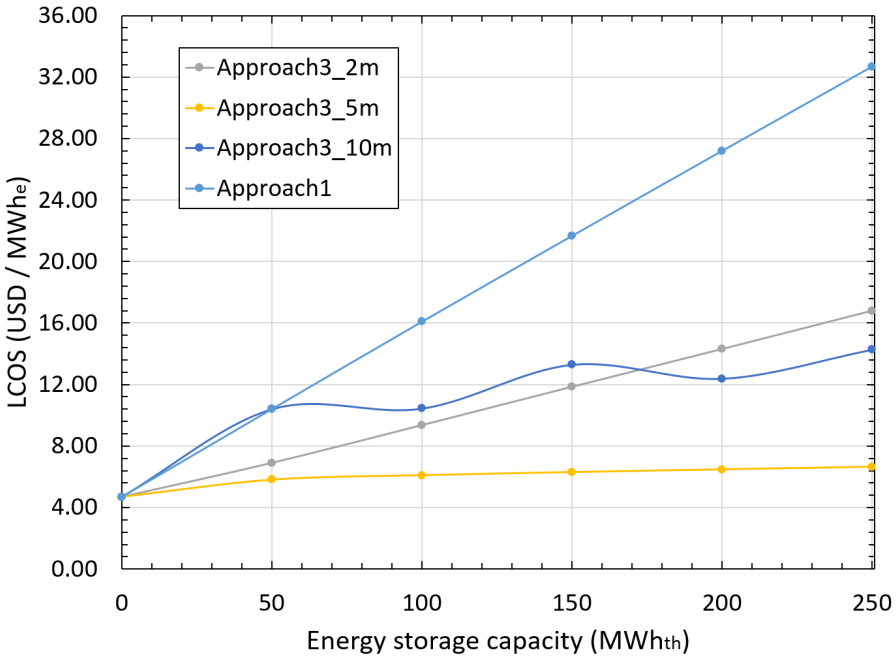

Figure 6.6: LCOS (USD/MWh_e) evolution with the energy storage capacity (MWh_{th}) for the first and third approaches.

Figures 6.3 and 6.4 highlight similar trends: employing multiple TES units reduces significantly reduces the electric fan power consumption and, consequently, operational costs in comparison with employing one single TES unit. In these Figures it can also be seen that the smaller the maximum length of the porous domain and higher the number of TES units used, the lower are the fan power consumption and OPEX since there is a smaller pressure drop to overcome in each unit. On the other hand, from Figure 6.5, it is clear that a smaller maximum bed length, which requires a higher number of TES units, implies a higher CAPEX, since a higher amount of structural and foundation material needs to be employed, and this effect becomes more pronounced as the desired energy storage capacity is higher.

Finally, from 6.6 it can be observed that the combined effects of the OPEX and CAPEX lead to very interesting results. As a matter of fact, from this Figure, it is clear that employing multiple TES units is more profitable than employing a single unit, since for almost every energy storage capacity the LCOS curve corresponding to the first approach was above the curves of all the other cases that employed several TES units. In addition, the approach that employed multiple units and limited the maximum length of the porous domain to 10 m led to an intermediate value for the LCOS, as despite presenting the second lowest CAPEX it presented the second highest OPEX, which significantly affects the LCOS. Conversely, the approach that employed multiple units and limited the maximum length of the porous domain to 2 m led also to an intermediate LCOS value, but this approach presented the highest CAPEX and lowest OPEX making the CAPEX the most penalizing element in the LCOS. In this way, the approach that led to the optimal LCOS and therefore the most economically advantageous option was employing multiple TES units and limiting the maximum porous domain length to 5 m. This approach presents the best trade-off

between bed length and number of TES units and, therefore, is the approach that most efficiently balanced capital and operational costs, leading to a stable LCOS that remained between 4.66 and 6.61 USD/MWh$_e$ throughout the analysed energy storage capacity range.

Furthermore, the LCOS evolution with the energy storage capacity for different TES materials was plotted in MATLAB for the approach employing multiple TES units and limiting the maximum porous domain length. These plots are presented in Figures 6.7, 6.8 and 6.9 when the maximum porous domain length is limited to 2 m, 5 m and 10 m, respectively.

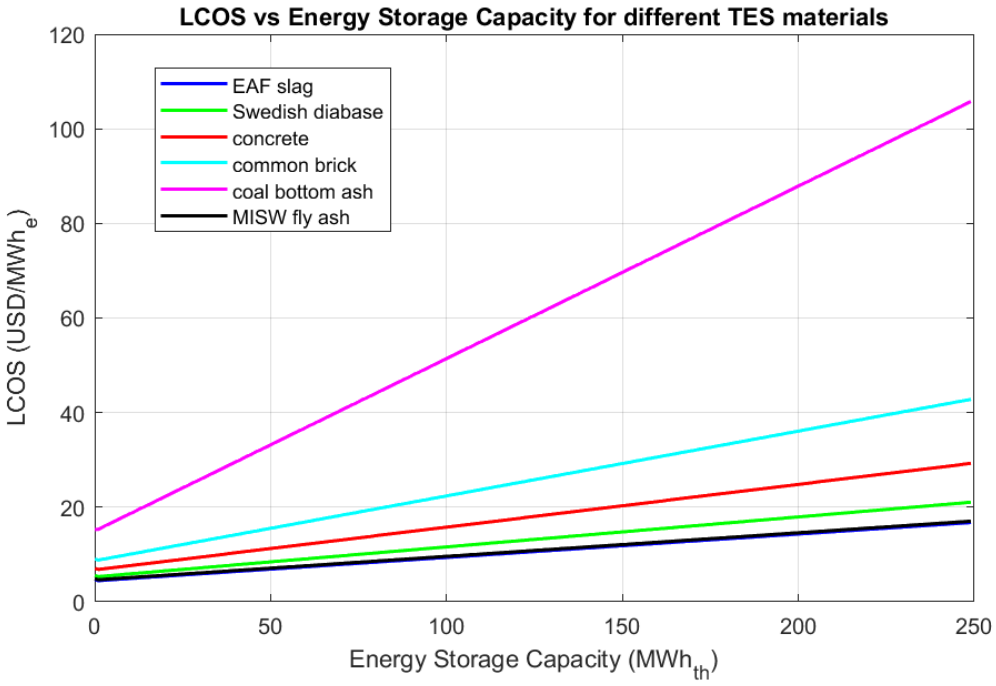

Figure 6.7: LCOS (USD/MWh$_e$) evolution with the energy storage capacity (MWh$_{th}$) for different TES materials using multiple TES units and limiting the length of the porous domain to 2 m.

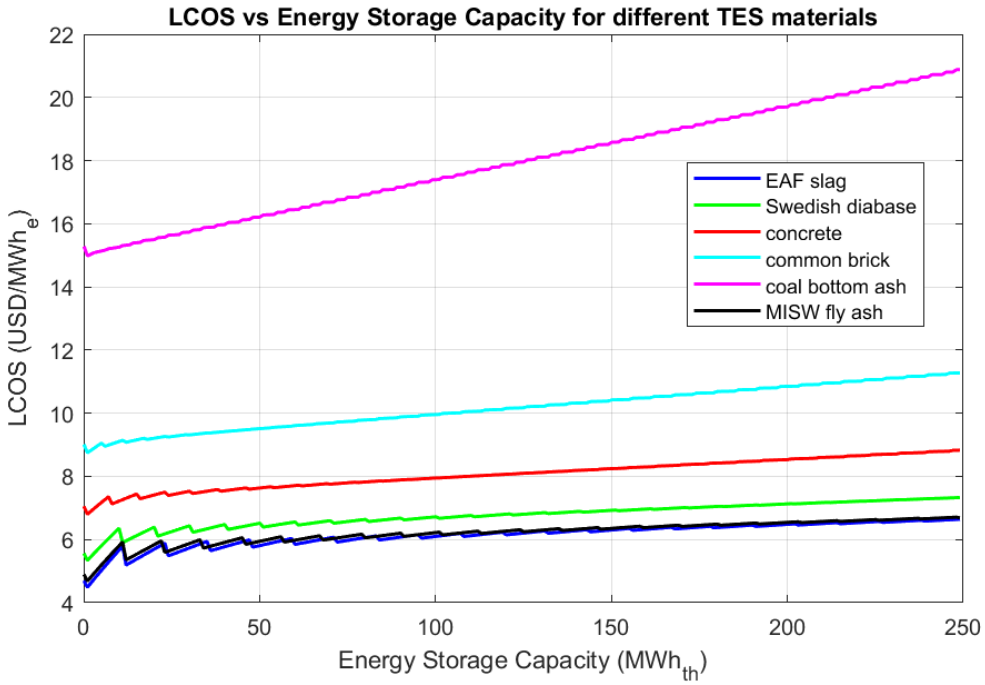

Figure 6.8: LCOS (USD/MWh$_e$) evolution with the energy storage capacity (MWh$_{th}$) for different TES materials using multiple TES units and limiting the length of the porous domain to 5 m.

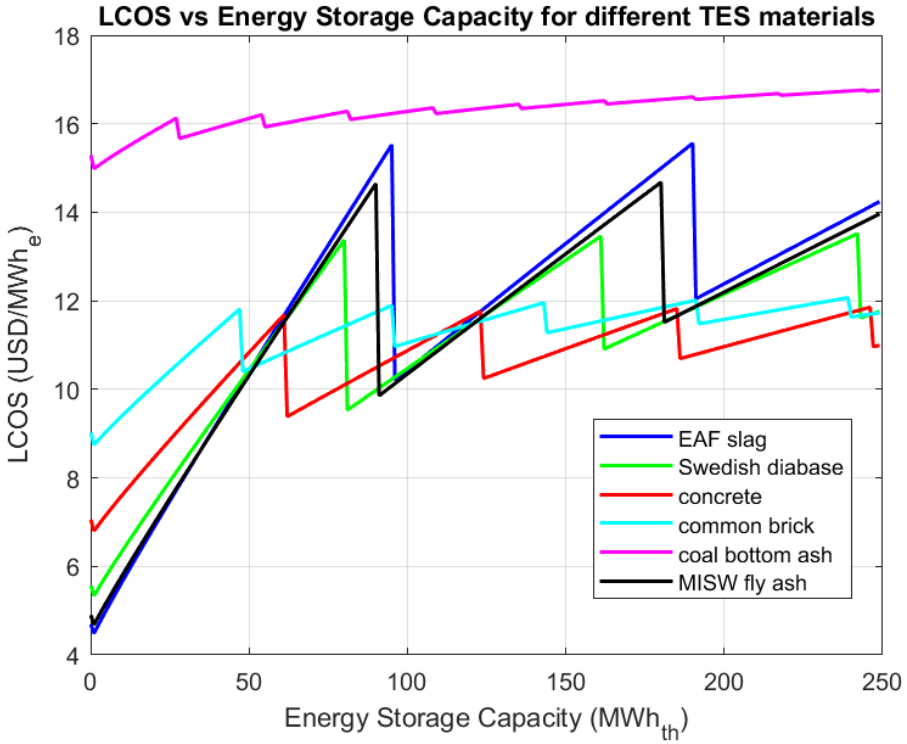

Figure 6.9: LCOS (USD/MWh$_e$) evolution with the energy storage capacity (MWh$_{th}$) for different TES materials using multiple TES units and limiting the length of the porous domain to 10 m.

First, Figures 6.7 and 6.9 reveal that, contrary to the trends observed in Figures 6.1 and 6.2, the LCOS curves are discontinuous and exhibit distinct fluctuations. This sawtooth behavior is attributed to the modular addition of TES units as capacity increases. In the case where the maximum length of the porous domain is limited to 2 m (Figure 6.7), these discrete transitions occur frequently and appear relatively smooth. Conversely, when the number of units increases more slowly, as seen in the case where the porous domain's length is longer, limited to 10 m (Figure 6.9), the individual impact of adding each new TES unit becomes highly pronounced, resulting in sharp, visible drops in LCOS.

In addition, Figures 6.7 to 6.9 highlight that, in all three cases, employing multiple TES units does not penalize materials with higher volumetric heat capacities, such as EAF slag, contrary to what was verified in the approach employing a single TES unit. In fact, from Figure 6.1, it had been concluded that in this approach, employing EAF slag as storage material would only be competitive for energy storage capacities up to 50 MWh_e, and for higher energy storage capacities the LCOS achieved using EAF slag would be higher than the LCOS achieved using other TES materials. However, when using multiple TES units and the maximum porous domain length is limited to 5 m or less, the lowest LCOS was achieved when employing EAF slag rather than any other material. In this way, the approach employing multiple TES units enabled exploiting the full potential of EAF slag and maximizing the benefits of its superior thermophysical properties, in particular for the case that limits the porous domain length to 5 m and which led to the optimal results. For this reason, the following economic analysis emplowed this approach, i.e., employing multiple TES units in parallel and limiting the porous domain length to 5 m.

Influence of the packing fraction of the porous domain

In order to comprehend the influence of the packing fraction of the porous domain in the LCOS and in the OPEX, the packing fraction of EAF slag was varied from 0.55 to 0.74 and the correspondent LCOS and OPEX were calculated. Figures 6.10 and 6.11 illustrate the variation of the LCOS and in the OPEX with the packing fraction, respectively.

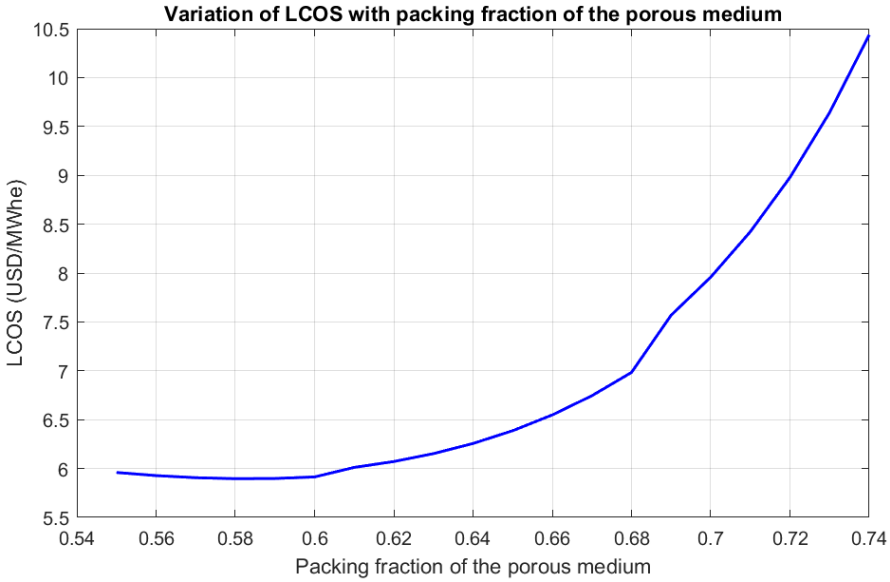

Figure 6.10: LCOS (USD/MWh_e) evolution with the packing fraction of the porous domain.

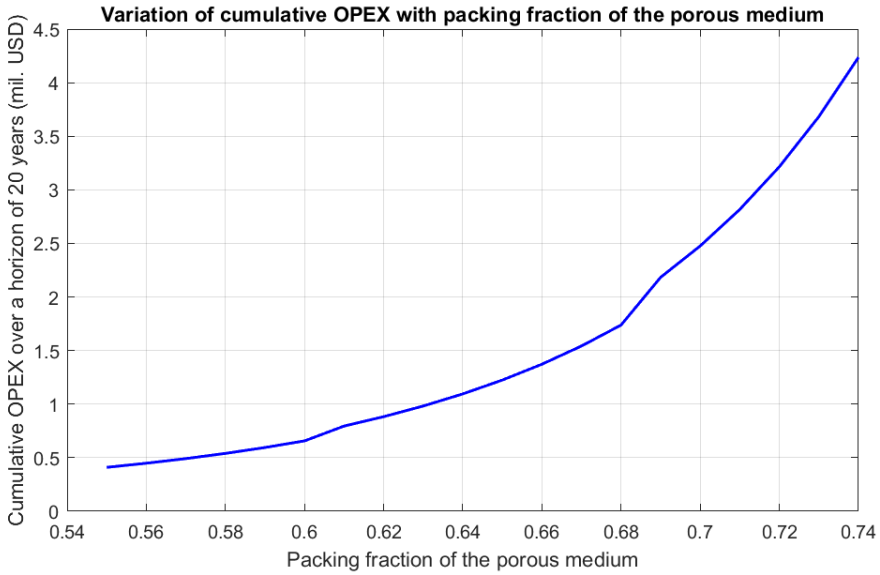

Figure 6.11: OPEX (mil. USD) evolution with the packing fraction of the porous domain.

From the observation of Figures 6.10 and 6.11 it can be seen that both LCOS and OPEX increase with the increase of the packing fraction, which is essentially associated with the reduction in bed porosity. Although a higher packing fraction reduces the storage volume required to achieve the target thermal energy storage capacity, which for simplicity was considered to be 100 MWh_{th}, the corresponding decrease in porosity significantly increases the pressure drop across the packed-bed, as predicted by the Ergun equation. This effect is particularly pronounced due to the inverse cubic dependence of pressure drop on porosity. Consequently, higher pumping power is required to circulate the HTF, leading to increased electricity consumption and operating costs. Since the

annual energy delivered by the system remains largely unchanged, the increase in OPEX directly translates into higher LCOS values. Finally, slight oscillations can be observed in both Figures for packing fractions of around 0.61 and 0.68. These oscillations can be justified with the decrease of the number of TES units verified when the higher packing fractions are used (initally, for packing fractions between 0.55 and 0.61, 10 units are required, for packing fractions between 0.61 and 0.68, 9 units are required, and for higher packing fractions until 0.74, 10 units are required).

Influence of the electricity cost

According to the equations applied to calculate the OPEX and the LCOS it is intuitive to understand that the cost of electricity has a direct impact in these parameters. To understand the magnitude of this impact, the unitary cost of electricity was varied from 0.05 to 0.5 USD/kW$_{el}$ and the correspondent LCOS and OPEX were calculated and plotted in Figures 6.12 and 6.13.

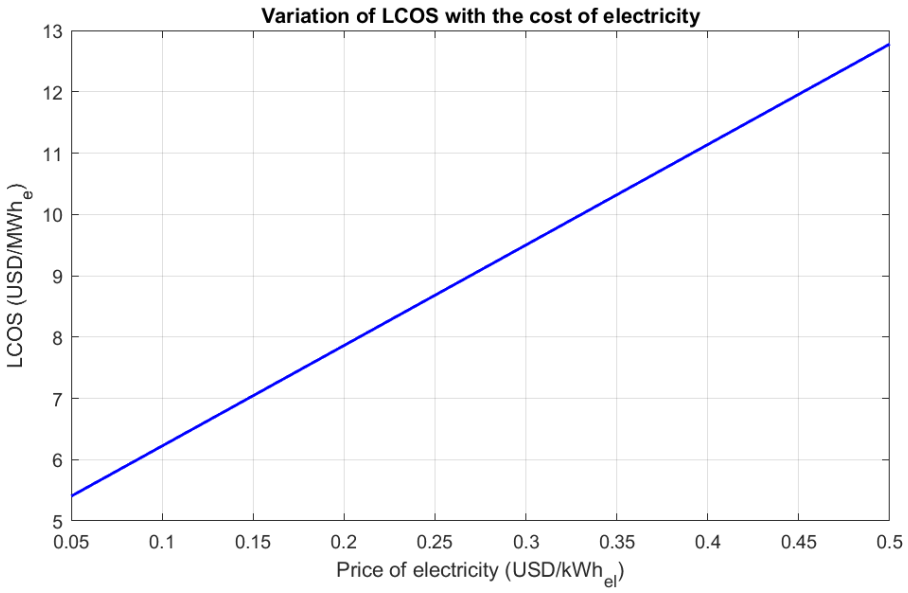

Figure 6.12: LCOS (USD/MWh$_e$) variation with the electricity cost (USD/kW$_{el}$).

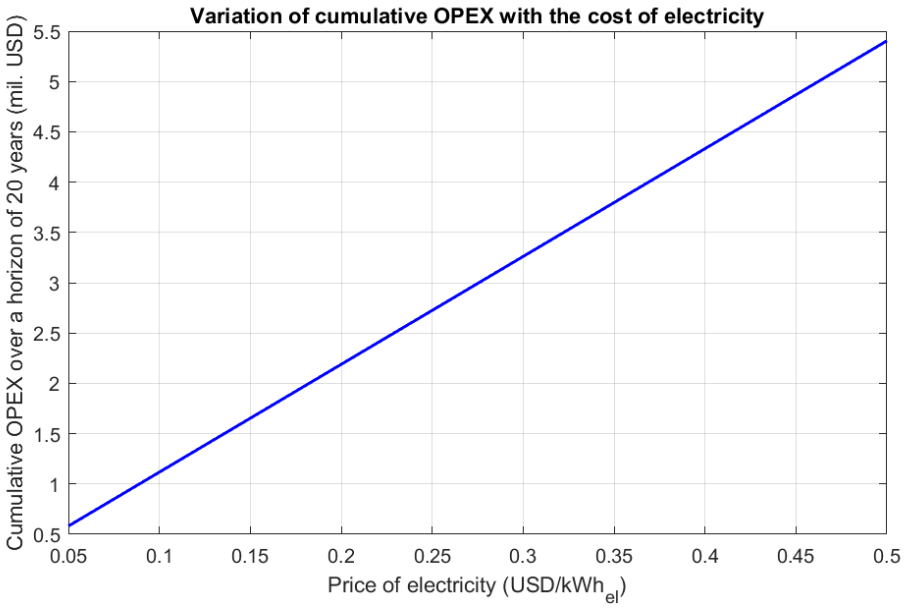

Figure 6.13: OPEX (million USD) variation with the electricity cost (USD/kW$_{el}$).

From the observation of the plots in Figures 6.12 and 6.13, a linear relationship between the unitary cost of electricity and LCOS and OPEX is observed and the slope of each graph is equal to 16.39 and to 10.72, respectively. This means that, for each increase of 0.1 USD/kW$_{el}$ in the unitary cost of electricity the values of the LCOS and OPEX increase approximately 1.64 USD/MWh$_{e}$ and 1.07 million USD, respectively. This observation highlights that the unitary electricity cost has a major impact in the economical viability of a packed-bed system project.

Influence of the selling price

In order to understand how much higher than the base production cost (LCOS) must the electricity recovered be priced to make the TES project using EAF slag financially feasible, the percentual increase relative to the LCOS was varied from 10 to 600 % and the respective NPV value was calculated. For this analysis, a packing fraction of 0.65 was considered, a unitary cost of electricity of 0.11 USD/kW$_{el}$ was considered, and an energy storage capacity of 100 MWh$_{th}$ was considered. The variation of the NPV with the percentual increase relative to the LCOS is illustrated in Figure 6.14. Figure 6.14 illustrates the resulting variation of the NPV. The plot suggests that to ensure a financially feasible project (NPV$\geq$ 0), the selling price of the recovered electricity must reflect an increase of at least 450% relative to the LCOS (corresponding to a selling price 5.5 times the base LCOS).

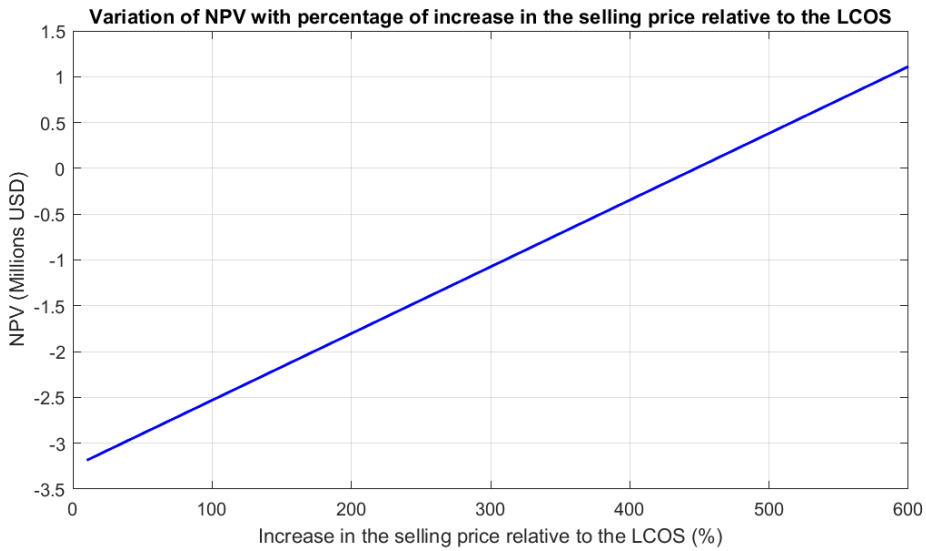

Figure 6.14: NPV (million USD) variation with the increase relative to the base production cost LCOS (%).

Techno-economic performance assessment and benchmarking

To assess the economic performance of the proposed thermal energy storage system using EAF slag as the TES material, several key techno-economic indicators were determined. The input parameters used for this analysis are equal to those specified in the "Model formulation and assumptions" section, and the first approach for the cross-sectional area and length of the porous domain was employed. Tables 6.3 and 6.4 present the technical and economical parameters calculated, respectively.

For the calculation of the water flow rate circulating in the heat exchanger of the conventional Rankine cycle considered to convert the thermal output into mechanical work, and then, into an electricity output, it was considered that the heat discharged by all TES units is gathered into a single, centralized heat exchanger connected to a single Rankine cycle and that the water circulating is heated from 0°C to 150°C.

Table 6.3: Technical parameters obtained for the TES system using EAF slag

Technical Parameters	Result	Unit
Superficial velocity during charge	0.83	m/s
Superficial velocity during discharge	0.66	m/s
Mass flow rate during charge	2.33	kg/s
Mass flow rate during discharge	1.86	kg/s
Pressure drop during charge	3332.61	Pa
Pressure drop during discharge	2260.45	Pa
Pumping energy for air circulation	2325.51	kWh
Water mass flow rate circulating in the heat exchanger	0.68	kg/s

Table 6.4: Economical parameters obtained for the TES system using EAF slag

Economical Parameters	Result	Unit
CAPEX	2951.84	thousands USD
Annual OPEX	97.71	thousands USD
Cumulative OPEX over an horizon of 20 years	1.04	millions USD
Total CAPEX + Cumulative OPEX	3.99	millions USD
LCOS	6.10	USD/MWh_e
NPV	18414	USD
Payback Period	10.53	years

Taking into account the results presented in Tables 6.3 and 6.4 it can be said that these are quite reasonable and within expected ranges from the literature using equivalent storage technologies.

A closer examination of the LCOS reveals that the design values reported by [61], for a packed-bed system using igneous acid rocks as storage material, range from 3 to 70 USD/MWh_e for a large-scale TES capacity of 4080 MWh_{th}, depending on the optimized aspect ratios and overall thermal efficiency. The packed-bed TES system employing EAF slag developed in the present work achieved an LCOS of 6.10 USD/MWh_e for a much smaller storage capacity of 100 MWh_{th}. Despite the significant difference in storage scale, where larger systems typically benefit from substantial economies of scale regarding containment and insulation costs, the obtained LCOS lies well within the the range reported by [61]. This suggests highly competitive economic performance, driven by the low cost and high volumetric heat capacity of the industrial slag byproduct. This comparison is particularly relevant, as [61] employs a highly integrated techno-economic optimization framework for high-temperature packed-bed thermal energy storage systems, providing one of the most appropriate benchmarks for the present study.

At the same time, in [69] a two-tank and a packed-bed TES system coupled with an Organic Rankine Cycle (ORC) power block for cogeneration are evaluated, using different rocks and different HTF, and the minimum Levelized Cost of Electricity (LCOE) values obtained range from 0.103 €/kWh_e and 0.146 €/kWh_e for a power output of the CSP plant of 100 kW_{th}. It should be noted that their analysis focused on the LCOE for the entire facility (including solar collectors, piping, and the power block)where the storage subsystem alone represents approximately 11.5% of the total plant capital expenses. Conversely, the model developed in the present work strictly isolates the Levelized Cost of Storage (LCOS), considering only the cost of the storage tanks, storage material, insulation, and fan power, assuming external heat is supplied at an upscaled capacity of 100 MWhth. This yielded an optimized LCOS of just 6.10 USD/MWhe (equivalent to 0.00529 €/kWhe). While a direct comparison with the total system LCOE is fundamentally limited, converting the literature's storage capital share implies a proportional storage cost contribution of roughly 13.65 USD/MWhe within their plant economics. The fact that the isolated LCOS obtained in this study is roughly 55% lower highlights not only the economic benefits of upscaling to a 100 MWh_{th} thermal capacity but also validates that the EAF slag packed bed per-

forms as a highly cost-effective subsystem that minimizes the financial weight of energy storage in large-scale commercial power plants.

In [70], the LCOS of several energy storage technologies was evaluated for a short-term grid application with a 100 MW power and a 400 MWh_{th} capacity. The results from [70] revealed that mature mechanical options present the most competitive levelized costs, with PHES and CAES ranging from 58 to 100 USD/MWh_e and from 81 to 140 USD/MWh_e, respectively, whereas chemical battery systems, such as LIB, exhibited higher costs, hovering around or above 260 USD/MWh_e. In comparison, the optimized packed-bed TES model utilizing EAF slag developed in the present work achieved a lower LCOS of 6.10 USD/MWh_e for a 100 MWh_{th} storage capacity. It is important to note that the literature system evaluates a larger capacity (400 MWh_{th}), which naturally benefits from macro-scale economies of scale regarding shared grid infrastructure. Remarkably, despite the smaller capacity of the present model, its LCOS outperforms the ranges of PHES and CAES reported by [70], likely due to the low raw material cost of the industrial EAF slag byproduct.

Finally, a comparison was made with the hydrogen-based storage system studied by [71]. Their work analyzed a large-scale seasonal storage scheme designed to capture an annual renewable surplus of 16.17 TWh, where electricity is converted to hydrogen via a 7 GW Proton Exchange Membrane (PEM) electrolyzer, stored long-term in geological salt caverns, and reconverted to electricity using a 2.23 GW gas turbine or a 1.86 GW fuel cell network. Due to the significant capital costs of geological storage and low round-trip conversion efficiencies, the LCOS reported by [71] ranged between 240 and 320 USD/MWhe. By comparison, the optimized EAF slag TES model in the present work achieved a significantly lower LCOS of 6.10 USD/MWhe for a 100 MWh_{th} capacity. Although hydrogen systems target massive, seasonal energy storage applications operating in the TWh-scale, this stark cost difference highlights that for short to medium-term grid balancing requirements, optimized thermal to electric packed-beds can deliver power back to the grid at a fraction of the levelized cost of a hydrogen economy pathway.

6.3 Limitations of the TEA

While the developed model successfully demonstrates the economic viability of an optimized EAF slag packed-bed system, several limitations and simplifying assumptions must be acknowledged concerning the scope of this study:

- The calculated CAPEX and OPEX depend heavily on localized material quotes (such as structural steel, insulation, and the TES materials) and electricity costs for fluid pumping. In reality, these resources are subject to significant price fluctuations driven by geographic location, inflation, and market supply chains.

- The model assumes a fixed electricity purchasing price for charging and a constant selling price for discharging throughout the project's lifetime. Real-world energy markets operate on highly dynamic arbitrage schemes where pricing fluctuates hourly.

- Regarding benchmarking comparisons with literature, direct comparisons with historical literature are bounded by global inflation. Comparing current material and construction prices against historical data from older studies introduces a natural economic bias, as a dollar spent today carries lower purchasing power than it did in previous decade(s).
- For simplicity, in the TEA conducted an efficiency was considered during the resting phase. In reality, transient fluid simulations performed in COMSOL show that the temperature within the tank drops progressively during standby periods. Therefore, assuming a constant air discharge temperature fixed at 82% of the maximum porous medium temperature serves as a practical baseline but disregards transient real behavior.
- For computational simplicity, the economic model uses constant integrated average fluid properties for both the charging and discharging phases. However, in operation, charging air enters hot and exits cold, whereas discharging air enters cold and exits hot. This simplification can therefore impact real-time mass flow rates, pressure drop and fan power requirements.
- Geometrical optimization in the TEA revealed that a fixed cross-sectional area yields unfeasible axial lengths and massive pressure drops at high energy storage capacities. While the optimized approach solves this by expanding the cross-sectional flow area (200-480 m^2), implementing such a large packed-bed in practice introduces civil engineering challenges regarding structural foundations and flow distribution.
- A scale mismatch exists between the numerical model developed for the simulations and the economic model. While the finite element models in COMSOL Multiphysics were upscaled to analyze fluid dynamics, the economic analysis evaluates a significantly larger commercial-scale facility (100 MWh_{th}). Extrapolating behavior across these different scales introduces minor boundary layer uncertainties.
- The model assumes that the physical properties of the EAF slag remain constant over the project lifetime. In reality, repeated thermal cycling up to high temperatures can cause mechanical degradation, cracking, or dust generation (siltation) within the slag pellets, which may gradually increase the bed's pressure drop and lower performance over its lifetime.
- Finally, the analysis assumes ideal insulation performance throughout the packed-bed's operational lifespan, neglecting possible thermal degradation over time.

Chapter 7

Conclusions and Future Work

7.1 Conclusions

This dissertation had as a primary objective the evaluation of the techno-economic viability of using iron and steel slag as a sustainable, low-cost solid medium for high temperature packed-bed TES systems. By coupling transient fluid dynamic analysis with an integrated economic optimization framework, this work successfully demonstrated that this industrial byproduct can serve as a highly competitive alternative to conventional packed-bed TES materials.

Restricting the transient simulations to the charging and resting phases proved sufficient to completely establish the system's performance boundaries. Regarding geometric optimization, while all the evaluated configurations eventually achieved a uniform target temperature profile (890 K) by the end of the 20 hour charging period, Geometry 3c demonstrated superior transient behavior by developing a significantly higher cumulative thermal energy storage capacity after the first 5 hours, achieving an energy storage capacity of 26.5 kWh_{th}

Using the selected Geometry 3c layout, investigating different inlet flow conditions revealed that higher flow rates lead to increased pressure drops (when employing a total flow rate of 1200 L/min and 300 L/min the pressure drop verified was 140 Pa and 12 Pa, respectively). When up-scaled beyond the boundaries of the present computational model, these elevated pressure drops could result in excessively high fan power requirements. Furthermore, comparing numerical pressure drops against analytical predictions using the Ergun equation validated the high accuracy of the model, matching almost perfectly. The minor differences were successfully attributed to to the simulation's ability to capture real-time temperature gradients rather than assuming static, temperature-independent fluid properties.

Evaluating the system over a 10 hour resting period showed that natural external convection along the tank walls causes non-uniform heat loss that progresses from the bottom of the tank upward. The lower sections degraded the fastest, dropping by up to 400 K, while the upper sections maintained their thermal energy exceptionally well, dropping by only 200 K and delaying degradation for the first 4 hours due to the high efficiency of the top insulation layer. Ultimately, these resting phase simulations effectively captured the physical limits of thermocline degradation

and front smearing driven by internal conduction and axial thermal dispersion, providing the exact thermodynamic boundaries required for subsequent economic optimization.

The techno-economical analysis in MATLAB revealed a critical trade-off between geometry and fan power. Forcing high volumetric flow rates through constrained, narrow geometries yields unfeasible axial lengths and drastic pressure drops. By implementing a geometric optimization framework that expands the cross-sectional area (ranging from 200 to 480 m^2 depending on the target capacity), the design effectively minimized fluid resistance. This kept fan electricity consumption remarkably low, ensuring that the system's internal pumping requirements do not compromise its net round-trip performance.

Regarding the structural configuration of the storage system, the comparison between utilizing a single TES unit versus a multiple-unit framework demonstrated that the latter offers superior operational feasibility for large-scale grid applications. While a single, larger packed-bed unit presents a slightly lower initial containment cost, it introduces severe pressure drops across extended porous domains. Furthermore, upscaling introduces geometric challenges where the surface area-to-volume ratio drops, leading to longer thermal response times, greater energy losses to the environment, and uneven temperature distributions. Conversely, implementing a modular configuration composed of multiple parallel units not only mitigates these penalties but also introduces critical operational redundancy. This modularity allows the system to undergo partial charging or maintenance without full plant downtime, proving that a multi-tank layout strikes the optimal balance between thermodynamic reliability and structural scalability. Ultimately, by adopting this multi-unit TES architecture and limiting the maximum porous domain length to 5 m, the system achieved an optimized LCOS of 6.10 USD/MWh_e for the target 100 MWh_{th} grid-scale asset.

When compared against established literature, the developed system demonstrated superior economic performance. Its LCOS lies well within the 3 - 70 USD/MWh_e baseline of massive thermal storage systems (such as the 4080 MWh asset by [61]), despite the system developed operating at a much smaller scale (100 MWh) without the full benefit of macro economies of scale. Furthermore, the EAF slag system comfortably undercuts chemical batteries and outpaces mature mechanical options like Pumped Hydro (PHES, 58 - 100 USD/MWh_e) and Compressed Air Energy Storage (CAES, 81 - 140 USD/MWh_e) [70]. Finally, it operates at a small fraction of the cost of long-term seasonal hydrogen schemes (240 - 320 USD/MWh_e) [71], proving its dominance for short-to-medium-term grid balancing.

Beyond the immediate techno-economic advantages identified in this work, the long-term viability of utilizing iron and steel slag as a thermal storage material is strongly reinforced by global industrial trends. As the global human population continues to grow, infrastructural and industrial demands dictate a corresponding, inevitable expansion in global steel production. Under a traditional linear economy model, this growth would exponentially exacerbate industrial waste management challenges, resulting in massive quantities of slag destined for landfills. However, integrating this industrial byproduct into high temperature packed-bed TES units directly drives a closed-loop circular economy. By transforming a widespread industrial waste stream into a valu-

able commodity for grid stabilization, this approach mitigates a critical environmental liability. Furthermore, as the regional supply of iron and steel slags scales alongside future steel production, market availability will inevitably increase. This supply expansion is projected to drive raw material acquisition costs downward, rendering the LCOS of slag based packed-beds even more economically competitive in future decades compared to resource-constrained alternatives.

In summary, this dissertation validates that replacing commercial storage mediums with industrial EAF slag byproducts, combined with careful geometric structuring, offers a highly viable, circular economy pathway towards very low cost daily grid stabilization and industrial waste heat recovery.

7.2 Future work

While this study provides a comprehensive assessment of EAF slag packed-bed systems, several opportunities remain for further academic and industrial research.

First of all, future work should extend the numerical simulations to include a full transient discharging cycle coupled directly to a power block model, such as, for instance, a steam turbine. This would allow for the dynamic evaluation of the power block's efficiency as the exiting air temperature begins to decrease due to thermocline front degradation.

The economic framework could be improved by replacing the static electricity pricing assumption with a real-world, dynamic price arbitrage model. Simulating hourly spot-market price fluctuations would capture the system's true economic performance when charging during surplus hours (low or even negative pricing) and discharging during peak grid demand (high pricing).

Experimental cyclic thermal testing of local EAF slag samples is recommended to evaluate long-term material integrity. Research should focus on whether repeated thermal cycling up to high temperatures triggers mechanical cracking, dusting (siltation), or chemical degradation, which could alter bed porosity and increase pressure drops over a 20 to 30 year operational lifespan.

Given that the optimized cross-sectional areas are quite large (200-480 m^2), future studies should focus on the civil and structural engineering design of the containment tank. This includes exploring practical foundation designs and modeling flow distributors (diffusers) to guarantee uniform air distribution and prevent fluid channeling through the massive porous domain.

References

[1] Jing Qiu et al. “Challenges and pathways of low-carbon oriented energy transition and power system planning strategy: a review”. In: *IEEE Transactions on Network Science and Engineering* 11.6 (2023), pp. 5396–5416.

[2] Joeri Rogelj et al. “Scenarios towards limiting global mean temperature increase below 1.5 °C”. In: *Nature Climate Change* 8 (Mar. 2018).

[3] K. Knobloch et al. “A partially underground rock bed thermal energy storage with a novel air flow configuration”. In: *Applied Energy* 315 (June 2022).

[4] European Commission, Copernicus, and ECMWF. *European State of the Climate - 2023 - Renewable energy resources*. Implemented by ECMWF as part of The Copernicus Programme. 2023. URL: https://climate.copernicus.eu/esotc/2023/renewable-energy-resources (visited on 03/06/2026).

[5] Rena Kuwahata, Javier Jorquera Copier, and Pablo Hevia-Koch. *Integrating Solar and Wind - Global experience and emerging challenges*. Tech. rep. International Energy Agency, 2024.

[6] Wood Mackenzie. *Global energy storage capacity to grow at CAGR of 31% to 2030*. Wood Mackenzie. 2020. URL: https://www.woodmac.com/press-releases/global-energy-storage-capacity-to-grow-at-cagr-of-31-to-2030/ (visited on 03/06/2026).

[7] S. Koohi-Fayegh and M. A. Rosen. “A review of energy storage types, applications and recent developments”. In: *Journal of Energy Storage* 27 (Feb. 2020).

[8] A. Gutierrez et al. “Industrial Waste Materials and By-products as Thermal Energy Storage (TES) Materials: A Review”. In: *AIP Conference Proceedings* (May 2016).

[9] World Steel Association. *Steel Industry Co-Products*. Fact sheet. 2021. URL: https://worldsteel.org/wp-content/uploads/Fact-sheet-Steel-industry-co-products.pdf (visited on 02/23/2026).

[10] Ghent University. *Searching: what is the snowball search method?* URL: https://onderzoektips.ugent.be/en/tips/00002030/ (visited on 04/02/2026).

[11] Leyla Amiri et al. “Progress on rock thermal energy storage (RTES): A state of the art review”. In: *Energy Science & Engineering* (Dec. 2024).

[12] M. Victoria et al. “The role of energy storage towards net-zero emissions in the European electricity system”. In: *Energy Conversion and Management* 27 (Feb. 2025).

[13] Johanna Gustavsson. “Energy Storage Technology Comparison - A knowledge guide to simplify selection of energy storage technology”. MA thesis. KTH School of Industrial Engineering and Management, 2016.

[14] Krishna J. Khatod, Vikrant P. Katekar, and Sandip S. Deshmukh. "An evaluation for the optimal sensible heat storage material for maximizing solar still productivity: A state-of-the-art review". In: *Journal of Energy Storage* 50 (June 2022).

[15] Md. Parvez Islam and Tetsuo Morimoto. "Advances in low to medium temperature non-concentrating solar thermal technology". In: *Renewable and Sustainable Energy Reviews* 82 (2018).

[16] Susane Kraemer. *Over 90% efficient energy storage improved by flowing heat round two pebble layers*. Solarpaces. 2024. URL: https://www.solarpaces.org/90-efficient-thermal-energy-storage-heat-round-pebble-layers-kth/ (visited on 03/02/2026).

[17] Khadija El Alami, Mohamed Asbik, and Hassan Agalit. "Identification of natural rocks as storage materials in thermal energy storage (TES) system of concentrated solar power (CSP) plants – A review". In: *Solar Energy Materials and Solar Cells* 217 (2020).

[18] Siemens Gamesa Renewable Energy. *World first: Siemens Gamesa begins operation of its innovative electrothermal energy storage system*. 2019. URL: https://www.siemensgamesa.com/global/en/home/press-releases/190612-siemens-gamesa-inauguration-energy-system-thermal.html (visited on 04/25/2026).

[19] Kun Du et al. "A review of the applications of phase change materials in cooling, heating and power generation in different temperature ranges". In: *Applied Energy* 220 (June 2018).

[20] Thermtest Instruments. *Understanding Phase Change Materials (PCM)*. Thermtest Instruments. 2024. URL: https://thermtest.com/phase-change-material-pcm (visited on 03/02/2026).

[21] Navid Aslfattahi et al. "Experimental investigation of energy storage properties and thermal conductivity of a novel organic phase change material/MXene as A new class of nanocomposites". In: *Journal of Energy Storage* 27 (Feb. 2020).

[22] P. Pardo et al. "A review on high temperature thermochemical heat energy storage". In: *Renewable and Sustainable Energy Reviews* 32 (Apr. 2014).

[23] Markus Hänchen, Sarah Brückner, and Alberto Steinfeld. "High-temperature thermal storage using a packed bed of rocks – Heat transfer analysis and experimental validation". In: *Applied Thermal Energy* 31 (July 2011).

[24] Iron Bull Manufacturing. *Challenges and Opportunities for Recycling Industrial Waste*. Iron Bull Manufacturing. 2026. URL: https://ibullmfg.com/blog/challenges-opportunities-recycling-industrial-waste/ (visited on 03/09/2026).

[25] A. Faika et al. "Thermal storage material from inertized wastes: Evolution of structural and radiative properties with temperature". In: *Solar Energy* 86 (Jan. 2012).

[26] D. Spasiano and F. Pirozzi. "Treatments of asbestos containing wastes". In: *Journal of Environmental Management* 204 (Dec. 2017).

[27] Antoine Meffre et al. "High-Temperature Sensible Heat-Based Thermal Energy Storage Materials Made of Vitrified MSWI Fly Ashes". In: *Waste Biomass Valor* (July 2015).

[28] A. Annie Giovanna et al. "Utilizing steel slag in sustainable construction materials: A comprehensive review". In: *Next Research* 8 (June 2026).

[29] Shuoyu Wang et al. "Enhancement of conventional concrete mix designs for sensible thermal energy storage applications". In: *Journal of Energy Storage* 61 (May 2023).

[30] FersiSolar. *Ceramics thermal energy storage*. FersiSolar. 2026. URL: https://fersisolar.com/en/ceramics-thermal-energy-storage/ (visited on 03/10/2026).

[31] Manglesh Kumar Gupta et al. "Experimental analysis of clay bricks incorporated with phase change material for enhanced thermal energy storage in buildings". In: *Journal of Energy Storage* 64 (Aug. 2023).

[32] GMK Center - Vadim Kolisnichenko. *EU recycled 92% of steel slag in 2024 - EUROSLAG*. 2024. URL: https://gmk.center/en/news/eu-recycled-92-of-steel-slag-in-2024-euroslag/ (visited on 04/02/2026).

[33] I. Ortega et al. "Thermo-physical properties of a steel-making by-product to be used as thermal energy storage material in a packed-bed system". In: *Energy Procedia* 69 (2015).

[34] Iñigo Ortega-Fernández et al. "Experimental Validation of Steel Slag as Thermal Energy Storage Material in a 400 kWht Prototype". In: *AIP Conference Proceedings* 2126 (July 2019).

[35] Jürgen Haunstetter, Michael Krüger, and Stefan Zunft. "Slag as an Inventory Material for Heat Storage in a Concentrated Solar Tower Power Plant: Experimental Studies on Design and Performance of the Thermal Energy Storage". In: *AIP Conference Proceedings* 2126 (July 2019).

[36] Wannapol Sadakorn et al. "Thermal performance and urban simulation study of climate-responsive bottom ash – Cement blocks". In: *Construction and Building Materials* 491 (2025).

[37] Fabrizio Marongiu, Stefano Soprani, and Kurt Engelbrecht. "Modeling of high temperature thermal energy storage in rock beds – Experimental comparison and parametric study". In: *Applied Thermal Engineering* 163 (2019).

[38] Doerte Laing et al. "Solid media thermal storage for parabolic trough power plants". In: *Solar Energy* 80 (Aug. 2006).

[39] IESVE Software. *Table 6 Thermal Conductivity, Specific Heat Capacity and Density*. IESVE Software. 2026. URL: https://help.iesve.com/ve2021/table_6_thermal_conductivity__specific_heat_capacity_and_density.htm (visited on 03/29/2026).

[40] Iñigo Ortega-Fernández et al. "Thermophysical characterization of a by-product from the steel industry to be used as a sustainable and low-cost thermal energy storage material". In: *Energy* 89 (2015).

[41] Yan Liang, Wei Li, and Xinghua Wang. "Influence of Water Content on Mechanical Properties of Improved Clayey Soil Using Steel Slag". In: *Geotechnical and Geological Engineering* (Oct. 2012).

[42] Huang Yi et al. "An overview of utilization of steel slag". In: *Procedia Environmental Sciences* 16 (2012).

[43] Kazuhiro Horii et al. *Overview of Iron/Steel Slag Application and Development of New Utilization Technologies*. Tech. rep. NIPPON STEEL & SUMITOMO METAL, 2015.

[44] C.W. Bale et al. *FactSage Thermochemical Software and Databases*. Version 8.4. 2025. DOI: 10.1016/j.calphad.2016.05.002.

[45] Peter C. Hayes, Chen Jiang, and Evgueni Jak. "PHASE EQUILIBRIA STUDY OF THE CaO-Fe_2O_3-SiO_2 SYSTEM IN AIR TO SUPPORT IRON SINTERING PROCESS OPTIMISATION". In: *Advances in Molten Slags, Fluxes, and Salts: Proceedings of The 10th International Conference on Molten Slags, Fluxes and Salts (MOLTEN16)* (2016).

[46] Qifeng SHU et al. "Effect of Na_2O on Dissolution Rate of Alumina in CaO-Al_2O_3-MgO-SiO_2 Slag". In: *ISIJ International* 55 (2015).

[47] Mikko ILJANA et al. "Evaluating the Reduction-Softening Behaviour of Blast Furnace Burden with an Advanced Test". In: *ISIJ International* 56 (2016).

[48] L. M. Juckes. *Dicalcium silicate in blast-furnace slag: a critical review of the implications for aggregate stability*. 2002. URL: Sage%20Journals%20-%20Mineral%20Processing%20and%20Extractive%20Metallurgy:%20Transactions%20of%20the%20Institutions%20of%20Mining%20and%20Metallurgy (visited on 04/25/2026).

[49] COMSOL Inc. *COMSOL Multiphysics*. Version 6.4. Stockholm, Sweden, 2025. URL: https://www.comsol.com.

[50] COMSOL AB. *Porous Media Flow Module User's Guide, Version 6.3*. 2024. URL: https://doc.comsol.com/6.3/doc/com.comsol.help.porous/PorousMediaFlowModuleUsersGuide.pdf (visited on 04/02/2026).

[51] COMSOL AB. *Heat Transfer Module User's Guide, Version 6.4*. 2025. URL: https://doc.comsol.com/6.4/doc/com.comsol.help.heat/HeatTransferModuleUsersGuide.pdf (visited on 04/02/2026).

[52] COMSOL AB. *Theory for the Nonisothermal Flow and Conjugate Heat Transfer Interfaces*. 2024. URL: https://doc.comsol.com/6.3/doc/com.comsol.help.heat/heat_ug_theory.07.081.html (visited on 04/02/2026).

[53] Frank P. Incropera. *Fundamentals of heat and mass transfer*. 6th. John Wiley & Sons, 2007. ISBN: 978-0470-50197-9.

[54] Iñigo Ortega-Fernández et al. "Parametric analysis of a packed bed thermal energy storage system". In: *AIP Conference Proceedings* 1850 (2017).

[55] The MathWorks Inc. *MATLAB*. Version R2024a. Natick, Massachusetts, 2024. URL: https://www.mathworks.com.

[56] Bei Yang et al. "Study on standby process of an air-based solid packed bed for flexible high-temperature heat storage: Experimental results and modelling". In: *Applied Energy* 238 (Mar. 2019).

[57] *Europe granulated slag from iron or steel manufacturong market analysis forecast size trends and insights*. URL: https://www.indexbox.io/store/europe-granulated-slag-from-iron-or-steel-manufacturing-market-analysis-forecast-size-trends-and-insights/ (visited on 05/25/2026).

[58] *How much does concrete cost per m3 in the UK - complete price breakdown*. URL: https://www.2brothers.uk/news/how-much-does-concrete-cost-per-m3-in-the-uk-complete-price-breakdown (visited on 05/25/2026).

[59] *Bricks.london*. URL: https://bricks.london/bricks/standard-clay-bricks/ (visited on 05/25/2026).

[60] Van-Dung Nguyen et al. "Sustainable Use of Coal Combustion Bottom Ash as A Fine Aggregate in Normal-Strength Concrete Production". In: *Journal of Science and Transport Technology* 5 (2025).

[61] Silvia Trevisan et al. “Packed bed thermal energy storage: A novel design methodology including quasi-dynamic boundary conditions and techno-economic optimization”. In: *Journal of Energy Storage* 36 (2021).

[62] *Amazon*. URL: amazon.com (visited on 05/25/2026).

[63] Rosalie T. Ruegg and Stephen R. Petersen. *Recommended Practice for Measuring Simple and Discounted Payback for Investments in Buildings and Building Systems*. Tech. rep. National Institute of Standards and Technology (NIST), 1995.

[64] Patricia Royo et al. “High-temperature PCM-based thermal energy storage for industrial furnaces installed in energy-intensive industries”. In: *Energy* 173 (Apr. 2019).

[65] Iñigo Ortega-Fernández and Javier Rodríguez-Aseguinolaza. “Thermal energy storage for waste heat recovery in the steelworks: The case study of the REslag project”. In: *Applied Energy* 237 (Mar. 2019).

[66] François Faraldo and Paul Byrne. “A Review of Energy-Efficient Technologies and Decarbonating Solutions for Process Heat in the Food Industry”. In: *Energies* 17 (June 2024).

[67] Abdulmajeed S. Al-Ghamdi and Ali Alaidaros. “Small-Scale Parabolic Trough–Concrete Thermal Energy Storage for Dispatchable Heat for Pharmaceutical Processes: A Makkah Case Study”. In: *Energies* 19 (Feb. 2026).

[68] Anabel Palacios et al. “Thermal Energy Storage Technology Roadmap for Decarbonising Medium-Temperature Heat Processes—A Review”. In: *Sunstainability* 17 (Oct. 2025).

[69] Nishith B. Desai, Maria E. Mondejar, and Fredrik Haglind. “Techno-economic analysis of two-tank and packed-bed rock thermal energy storages for foil-based concentrating solar collector driven cogeneration plants”. In: *Renewable Energy* 186 (2022).

[70] Verena Jülch. “Comparison of electricity storage options using levelized cost of storage (LCOS) method”. In: *Applied Energy* 183 (2016).

[71] C. Martínez de Leon et al. “Levelized Cost of Storage (LCOS) for a hydrogen system”. In: *International Journal of Hydrogen Energy* 52 (2024).

Appendix A

MATLAB code

```
clc;
clear;

%% load air property interpolant functions

air_data = load('../air_props.mat');
cp_air_fun  = air_data.Cp_air_fun;
rho_air_fun = air_data.rho_air_fun;

% Preallocation of vectors with zeros
LCOS_EAFslag = zeros(1,200);
LCOS_SwedishDiabase = zeros(1,200);
LCOS_Concrete = zeros(1,200);
LCOS_CommonBrick = zeros(1,200);
LCOS_CoalBottomAsh = zeros(1,200);
LCOS_MISW = zeros(1,200);
NPV_EAFslag = zeros(1,200);
EnergyStorageCapacity = zeros(1,200);


j = 1;
for E_tes = 50:1:250   % Energy Capacity (Q) in MWh converted to
 ↪  Joules (J)

    %% Initial parameters

    E_tes_J = E_tes*1e6*3600;   % convert MWh to J

    t_ch_hr = 8;      % hours
```

```
t_dch_hr = 10;    % hours

t_ch = t_ch_hr * 3600;      % seconds
t_dch = t_dch_hr * 3600;    % seconds

t_op = t_ch + t_dch;  % (s) total operation time it is tcharge +
 ↪  tdischarge

q_tes = (E_tes/t_ch_hr)*1e6; % W


%% Storage volume and ratios of volume

% (EAF slag, Swedish diabase, concrete, common brick, coal
 ↪  bottom ash, MISW, fly ash)
rho_rock = [3430 3007 2250 1922 1400 2940];       % Density of
 ↪  TES materials in kg/m^3 from literature
cp_rock = [933 900 920 837 650 1030];             % Specific heat
 ↪  capacity of TES materials in J/kg·K from literature, assumed
 ↪  constant and equal to Cp(500°C)
c_rock = [31.03 294.75 174.65 250 45.61 44.34];  % Cost of TES
 ↪  material in $/m^3
num_mat = length(rho_rock);

% Packing fraction (volume fraction occupied by sand particles)
packing_fraction = 0.65; % Assumed packing fraction (adjustable)

T_max = 616.85; % °C
T_min = 20;     % °C

T1 = T_min + 273.15; % K
T2 = T_max + 273.15; % K

% ratios of volumes of materials taken from the COMSOL model
 ↪  (Geometry 1)
r_vermiculite_storage = 2.157276445; % ratio between the volume
 ↪  of vermiculite insulation and the volume of storage material
r_superwool_storage = 1.172937768;   % ratio between the volume
 ↪  of superwool insulation and the volume of storage material
```

```
r_steel_storage = 0.095603539;       % ratio between the volume
 ↪  of steel and the volume of storage material, assuming a
 ↪  thickness of 1mm

% Inputs necessary for the foundation volume calculation
rho_steel = 7850;       % kg/m^3
rho_vermiculite = 80;   % kg/m^3
rho_superwool = 96;     % kg/m^3

% Preallocation of vectors with zeros
volume_storage = zeros(1,num_mat);
rho_effective = zeros(1,num_mat);
W1 = zeros(1,num_mat);
W2 = zeros(1,num_mat);
W1_kN = zeros(1,num_mat);
W2_kN = zeros(1,num_mat);
P = zeros(1,num_mat);
A_foundation = zeros(1,num_mat);
V_foundation = zeros(1,num_mat);
capx = zeros(1,num_mat);
S = zeros(1,num_mat);
A = zeros(1,num_mat);
L = zeros(1,num_mat);
u_ch = zeros(1,num_mat);
u_dch = zeros(1,num_mat);
term1c = zeros(1,num_mat);
term2c = zeros(1,num_mat);
dpscale_ch = zeros(1,num_mat);
dp_ch = zeros(1,num_mat);
mdot_ch_A = zeros(1,num_mat);
term1d = zeros(1,num_mat);
term2d = zeros(1,num_mat);
dpscale_dch = zeros(1,num_mat);
dp_dch = zeros(1,num_mat);
mdot_dch_A = zeros(1,num_mat);
E_pump_charge = zeros(1,num_mat);
E_pump_discharge = zeros(1,num_mat);
E_pump = zeros(1,num_mat);
E_pump_kWh = zeros(1,num_mat);
opex = zeros(1,num_mat);
```

```
opex_hr = zeros(1,num_mat);
total_cost = zeros(1,num_mat);
capx_adj = zeros(1,num_mat);
OPEX_20years = zeros(1,num_mat);
LCOS = zeros(1,num_mat);
Anual_CAPEX = zeros(1,num_mat);
MWh_delivered_1cycle = zeros(1,num_mat);
MWh_delivered_1cycle_e = zeros(1,num_mat);
Q_in = zeros(1,num_mat);
m_water = zeros(1,num_mat);
MWh_delivered_1y_e = zeros(1,num_mat);
E_net_1y = zeros(1,num_mat);
Price_MWh = zeros(1,num_mat);
NPV_final = zeros(1,num_mat);
Payback = zeros(1,num_mat);


for i = 1: num_mat

   volume_storage(i) = E_tes_J /
    ↪  (rho_rock(i)*packing_fraction*cp_rock(i)*(T2-T1)); % in
    ↪  m^3

    %% Foundation volume calculation

    rho_effective(i) = rho_rock(i)*packing_fraction;

    W1(i) = volume_storage(i)*r_steel_storage*rho_steel +
     ↪  rho_vermiculite*volume_storage(i)*r_vermiculite_storage
     ↪  + rho_superwool*volume_storage(i)*r_superwool_storage;
     ↪  % Weight of packed bed system (W1)
    W2(i) = rho_effective(i)*volume_storage(i);   % Weight of
     ↪  packed storage material (W2)
    Load = 5000;    % the live load (kg); suggested: 1500-5000
     ↪  Live load (L)
    SF = 2;         % the safety factor:;   (SF) Suggested:
     ↪  1.5-2.0
    q_allow = 100;  % allowable soil bearing pressure (kN/m^2),
     ↪  suggested q allow = 100 to 150 kN/m2
```

```
depth = 0.75;   % foundation depth (m)     % Depth of
 ↪  foundation (d) Suggested: 0.5+

% Convert weights from kg to kN (1 kg = 0.00981 kN)
W1_kN(i) = W1(i) * 0.00981;
W2_kN(i) = W2(i) * 0.00981;
L_kN = Load * 0.00981;

% Total Load Calculation
P(i) = (W1_kN(i) + W2_kN(i) + L_kN) * SF; % Total foundation
 ↪  load in kN

% Foundation Area Calculation
A_foundation(i) = P(i) / q_allow; % Area of the foundation
 ↪  (m^2)

% Foundation Volume Calculation
V_foundation(i) = A_foundation(i) * depth; % Volume of the
 ↪  foundation (m^3)


%% Simplified MATLAB code to calculate CAPEX based on
 ↪  storage volume

c_vermiculite = 2000; % $/m^3
c_superwool = 800;    % $/m^3
c_steel = 42354;      % $/m^3

% capx = SUMM ( ci * Vi ) where ci is the unitary cost
 ↪  ($/m^3) and Vi is the volume (m^3) of each component
capx(i)= c_rock(i)*volume_storage(i) +
 ↪  c_vermiculite*volume_storage(i)*r_vermiculite_storage +
 ↪  c_superwool*volume_storage(i)*r_superwool_storage +
 ↪  c_steel*volume_storage(i)*r_steel_storage +
 ↪  c_rock(3)*V_foundation(i);   % $


%% opex calculations

S_orig = 0.201;  % m, original side of the porous domain
```

```
    L_orig = 0.382;  % m, original length of the porous domain
    V_orig = S_orig^2 * L_orig;  % m, original volume of the
     ↪ porous domain
    k = (volume_storage(i)/V_orig)^(1/3); % Linear scaling
     ↪ factor
    S(i) = k*S_orig;
    A(i) =  S(i)^2;  % Crosssection area of the packed bed
     ↪ (m^2), 0.040401;
    L(i) = k*L_orig; % Length of the packed bed (m);

    eta_0 = 0.9;     % 0.85; % preliminary Efficiency of TES
     ↪ during charging
    eta_0d = 0.9;    % 0.85; % preliminary Efficiency of TES
     ↪ during discharging
    dt = 1;          % Time step in seconds

    % average air properties from interpolant functions
    cp = integral(cp_air_fun,T1,T2)/(T2-T1);      % J/kgK
    rho_f = integral(rho_air_fun,T1,T2)/(T2-T1);  % kg/m3


    %% 3rd approach: using multiple TES units in parallel

    N_tes = 1; % no of tes units

while L > 5
    N_tes = N_tes + 1;
    k = ((volume_storage/N_tes)/V_orig)^(1/3); % Linear scaling
     ↪ factor
    S = k*S_orig;
    A = S^2;
    L = k*L_orig;
    capx= N_tes * (c_rock*volume_storage/N_tes +
     ↪ c_vermiculite*volume_storage/N_tes*r_vermiculite_storage
     ↪ + c_superwool*volume_storage/N_tes*r_superwool_storage +
     ↪ c_steel*volume_storage/N_tes*r_steel_storage +
     ↪ 174.65*V_foundation);   % $
end

    Tavg = 0.5*(T1+T2);  % K
```

```
% Dynamic viscosity of air (Pa·s)
mu = 1.716e-5*(Tavg/273.15)^(3/2)*((273.15+111)/(Tavg+111));
 ↪  % Sutherland's Equation which yields highly accurate
 ↪  results over standard atmospheric temperatures

delh= cp*(T2 - T1) ;

mscale_ch = E_tes*1e6*3.6e3/(delh*t_ch*N_tes*eta_0);    %
 ↪  kg/s for charging
mscale_dch = E_tes*1e6*3.6e3/(delh*t_dch*N_tes*eta_0d); %
 ↪  kg/s for discharging

epsilon = 1-packing_fraction;       % Void fraction
 ↪  (porosity) of the packed bed
u_ch(i) = mscale_ch/(rho_f*A(i));   % charging Superficial
 ↪  velocity of air (m/s)
u_dch(i) = mscale_dch/(rho_f*A(i)); % discharging
 ↪  Superficial velocity of air (m/s)
dia_p = 0.015;                      % Diameter of particles
 ↪  in the packed bed (m)


%% Charging Calculate pressure drop using Ergun equation

term1c(i) = (150 * mu * (1 - epsilon)^2 * u_ch(i)) /
 ↪  (epsilon^3 * dia_p^2) * L(i);
term2c(i) = (1.75 * rho_f * (1 - epsilon) * u_ch(i)^2) /
 ↪  (epsilon^3 * dia_p) * L(i);

dpscale_ch(i) = term1c(i) + term2c(i);

mdot_ch = mscale_ch;        % Mass flow rate during charging
 ↪  (vector)
dp_ch(i) = dpscale_ch(i);  % Pressure drop during charging
 ↪  (vector)

% mdot should be  per unit cross section.
mdot_ch_A(i) = mdot_ch/A(i); % (kg/m2s) according to
 ↪  trevisan paper
```

```
%% DisCharging Calculate pressure drop using Ergun equation

term1d(i) = (150 * mu * (1 - epsilon)^2 * u_dch(i)) /
 ↪  (epsilon^3 * dia_p^2) * L(i);
term2d(i) = (1.75 * rho_f * (1 - epsilon) * u_dch(i)^2) /
 ↪  (epsilon^3 * dia_p) * L(i);

dpscale_dch(i) = term1d(i) + term2d(i);

mdot_dch = mscale_dch;        % Mass flow rate during
 ↪  charging (vector)
dp_dch(i) = dpscale_dch(i);  % Pressure drop during charging
 ↪  (vector)

% mdot should be  per unit cross section.
mdot_dch_A(i) = mdot_dch/A(i); % (kg/m2s) according to
 ↪  trevisan paper


%% calculation of opex of pumping fluid

eta_circ = 0.95; % air circulator efficiency, assumed equal
 ↪  to 0.95

% mass flowrate and pressure drop assumed constant
E_pump_charge(i) = (A(i) * N_tes * mdot_ch_A(i) * dp_ch(i) *
 ↪  t_ch) / rho_f / eta_circ;
E_pump_discharge(i) = (A(i) * N_tes * mdot_dch_A(i) *
 ↪  dp_dch(i) * t_dch) / rho_f / eta_circ;

% here the unit comes to be Nm or joules
E_pump(i) = E_pump_charge(i) + E_pump_discharge(i) ;
E_pump_kWh(i)= E_pump(i)*(1e-3)/(3600); % converted to kWh

C_el = 0.11;  % ($/kWh_el) fixed electricity price

% Assumption: the system performs 1 complete cycle per day
cycles_per_day = 1;
```

```
cycles_per_year = 365 * cycles_per_day;
n = 20;

WAAC = 0.04;     % Realistic 4 % Weighted Average Cost of
 ↪  Capital
CRF = WAAC*(1+WAAC)^n / ((1+WAAC)^n-1);  % Capital Recovery
 ↪  Factor

Anual_CAPEX(i) = capx(i) * CRF;  % Anualized CAPEX

% Based on the article or the CAPEX
opex(i) = (0.02*Anual_CAPEX(i)) +
 ↪  (E_pump_kWh(i)*C_el*(365));  %% this is USD in a year


%% Levelized cost of storage (LCOS) calculation

MWh_delivered_1cycle(i) =
 ↪  A(i)*N_tes*mdot_dch_A(i)*cp*(0.82*T2-T1)*t_dch/(10^6*3600);
 ↪  % MWh th, 82% is the ratio Tfinal after 5 h resting /
 ↪  Tinit taken from COMSOL
MWh_delivered_1cycle_e(i) = 0.38*MWh_delivered_1cycle(i); %
 ↪  in MWhe efficiency of the cycle taken from article
 ↪  trevisan

% Assuming Heat Exchanger with water being heated from 0°C
 ↪  to 150°C
eta_HX = 0.75;  % efficiency of the heat exchanger
Q_in(i) = MWh_delivered_1cycle(i)*eta_HX/t_dch_hr*10^3;  %
 ↪  kW thermal
cp_water = 4184; % (J/(kg.K))approx. specific heat capacity
 ↪  of liquid water
delta_T = 150-0; % °C or K
h_1 = 0.01;  % enthalpy (kJ/kg) of superheated water at
 ↪  T=0°C
h_2 = 2803;  % enthalpy (kJ/kg) of superheated water at
 ↪  T=150°C
m_water(i) = 0.38*Q_in(i)/(cp_water/1000*delta_T+(h_2-h_1));
 ↪  % flow rate of water (kg/s) circulating in the HX
```

```
% Annual energy delivery based on complete cycles per year
MWh_delivered_1y_e(i) = MWh_delivered_1cycle_e(i) *
 ↪  cycles_per_year;

eta_CSP = 0.5;  % Approx. efficiency of CSP plant
E_input = E_tes / eta_CSP;  % MWh_e per cycle
E_input_1y = E_input * cycles_per_year;  % MWh_e per year
E_net_1y(i) = E_input_1y - MWh_delivered_1y_e(i);

DR = 0.07;  % Discount Rate of 7 %, trevisan

% LCOS formula (Annualized Costs / Annual Generation)
% LCOS = (Anual_CAPEX + opex) / E_net_1y; % USD/MWhe

% LCOS according to trevisan, over 20 years life of
 ↪  operation
cumulative_opex = 0;
cumulative_Enet = 0;
for a = 1:n
    cumulative_opex = cumulative_opex + opex(i) / (1+DR)^a;
    cumulative_Enet = cumulative_Enet + E_net_1y(i) /
     ↪  (1+DR)^a;
end
LCOS(i) = (capx(i) + cumulative_opex) / cumulative_Enet;  %
 ↪  USD/MWhe

total_cost(i) = (capx(i)+cumulative_opex)/1e6;  % in mil.
 ↪  USD, total cost withoyt considering the value of money

%% Net Present Value
Increase = 450; % 450 % of increase in relation with LCOS

cumulative_cash_flow = 0; % Reset the accumulator
Price_MWh(i) = (1 + Increase/100) * LCOS(i);  % USD/MWhe

Sales = zeros(20);
CF = zeros(20);
for p = 1:20
```

```
            Sales(p) = MWh_delivered_1y_e(i) * Price_MWh(i);  %
             ↪ Assuming that every year p the sold energy is cte.
             ↪ and 100% of the energy delivered is sold
            CF(p) = Sales(p) - opex(i);

            % cumulative discounted cash flow
            cumulative_cash_flow = CF(p)/(1+DR)^p +
             ↪ cumulative_cash_flow;
        end
        % Calculate final NPV for Year 20 under this specific
         ↪ 'Increase' value
        NPV_final(i) = -capx(i) + cumulative_cash_flow; % USD


        %% Payback Period
        % Payback period = Initial Investment / Annual Cash Inflow
        Payback(i) = capx(i) / CF(1);  % This is the simple payback,
         ↪ which does not account for the value of money

    end

    LCOS_EAFslag(j) = LCOS(1);
    LCOS_SwedishDiabase(j) = LCOS(2);
    LCOS_Concrete(j) = LCOS(3);
    LCOS_CommonBrick(j) = LCOS(4);
    LCOS_CoalBottomAsh(j) = LCOS(5);
    LCOS_MISW(j) = LCOS(6);
    NPV_EAFslag(j) = NPV_final(1) / 10^6;   % mil. USD
    EnergyStorageCapacity(j) = E_tes;
    j = j+1;
end

%% Plots
figure(1)
plot(EnergyStorageCapacity,LCOS_EAFslag,'Color','b','LineWidth',
 ↪ 1.5);
grid on;
hold on
plot(EnergyStorageCapacity,LCOS_SwedishDiabase,'Color','g','LineWidth',
 ↪ 1.5);
```

```
plot(EnergyStorageCapacity,LCOS_Concrete,'Color','r','LineWidth',
 ↪  1.5);
plot(EnergyStorageCapacity,LCOS_CommonBrick,'Color','c','LineWidth',
 ↪  1.5);
plot(EnergyStorageCapacity,LCOS_CoalBottomAsh,'Color','m','LineWidth',
 ↪  1.5);
plot(EnergyStorageCapacity,LCOS_MISW,'Color','k','LineWidth', 1.5);
title('LCOS vs Energy Storage Capacity for different TES materials')
xlabel('Energy Storage Capacity (MWh)')
ylabel('LCOS (USD/MWhe)')
legend('EAF slag','Swedish diabase', 'concrete', 'common brick',
 ↪  'coal bottom ash', 'MISW fly ash')
hold off

figure(2)
plot(EnergyStorageCapacity,NPV_EAFslag,'Color','b','LineWidth',
 ↪  1.5);
grid on;
title('NPV vs Energy Storage Capacity for EAF slag')
xlabel('Energy Storage Capacity (MWh)')
ylabel('NPV (mil. USD)')
```

Appendix B

Results from the TEA analysis

Tables B.1 and B.2 present the most relevant techno-economical results obtained using EAF slag as the storage material and employing the two approaches that were previously tested to calculate the cross-sectional area of the porous domain. Similarly, Tables B.3 to B.5 present the corresponding results obtained using the multiple units' approach when fixing the maximum length of the porous domain to 2, 5 and 10 m.

Table B.1: Results obtained using one single TES unit and scaling all the dimensions of the porous domain.

Energy Storage Capacity (MWh_{th})	0.05	50.05	100.05	150.05	200.05	250.05
Number of TES units	1	1	1	1	1	1
Length of the porous domain (m)	0.81	8.06	10.16	11.63	12.80	13.78
Cross-sectional area (m^2)	0.18	18.00	28.56	37.42	45.33	52.60
Velocity during charging (m/s)	0.14	1.37	1.73	1.98	2.18	2.35
Velocity during discharging (m/s)	0.11	1.10	1.38	1.58	1.74	1.88
Yearly OPEX (Thousands of USD / year)	0.00	191.22	733.12	1616.44	2837.37	4393.55
Cumulative OPEX (20y) (Thousands of USD)	0.03	2025.81	7766.72	17124.64	30059.14	46545.29
Electrical Fan Power (kWh_e)	0.01	4712.12	18158.53	40108.57	70467.15	109175.70
CAPEX (Thousands of USD)	1.51	1379.52	2757.54	4135.55	5513.57	6891.58
LCOS (USD/MWh_e)	4.70	10.40	16.09	21.67	27.19	32.68

Table B.2: Results obtained using one single TES unit and fixing the cross-sectional area of the porous domain to 20 m^2.

Energy Storage Capacity (MWh_{th})	0.05	50.05	100.05	150.05	200.05	250.05
Number of TES units	1	1	1	1	1	1
Length of the porous domain (m)	0.01	7.26	14.51	21.75	29.00	36.25
Cross-sectional area (m^2)	20.00	20.00	20.00	20.00	20.00	20.00
Velocity during charging (m/s)	0.00	1.24	2.47	3.70	4.94	6.17
Velocity during discharging (m/s)	0.00	0.99	1.98	2.96	3.95	4.94
Yearly OPEX (Thousands of USD / year)	0.00	142.59	2037.06	9934.55	30812.83	74376.29
Cumulative OPEX (20y) (Thousands of USD)	0.02	1510.56	21580.62	105246.80	326431.61	787943.43
Electrical Fan Power (kWh_e)	0.00	3500.76	50635.11	247284.38	767240.86	1852207.82
CAPEX (Thousands of USD)	1.51	1379.52	2757.54	4135.55	5513.57	6891.58
LCOS (USD/MWh_e)	4.68	8.83	37.20	111.48	253.75	486.10

Table B.3: Results obtained using multiple TES units and fixing a maximum length of the porous domain in each unit to 2 m.

Energy Storage Capacity (MWh_{th})	0.05	50.05	100.05	150.05	200.05	250.05
Number of TES units	1	66	131	197	262	328
Length of the porous domain (m)	0.81	2.00	2.00	2.00	2.00	2.00
Cross-sectional area (m^2)	0.18	1.10	1.11	1.11	1.11	1.11
Velocity during charging (m/s)	0.14	0.34	0.34	0.34	0.34	0.34
Velocity during discharging (m/s)	0.11	0.27	0.27	0.27	0.27	0.27
Yearly OPEX (Thousands of USD / year)	0.00	7.58	17.54	29.82	44.44	61.43
Cumulative OPEX (20y) (Thousands of USD)	0.03	80.31	185.78	315.87	470.83	650.81
Electrical Fan Power (kWh_e)	0.01	108.93	219.07	327.80	437.94	546.67
CAPEX (Thousands of USD)	1.51	2179.46	5939.02	11316.82	18251.74	26829.23
LCOS (USD/MWh_e)	4.70	6.90	9.36	11.86	14.31	16.81

Table B.4: Results obtained using multiple TES units and fixing a maximum length of the porous domain in each unit to 5 m.

Energy Storage Capacity (MWh_{th})	0.05	50.05	100.05	150.05	200.05	250.05
Number of TES units	1	5	9	13	17	21
Length of the porous domain (m)	0.81	4.72	4.88	4.94	4.98	5.00
Cross-sectional area (m^2)	0.18	6.16	6.60	6.77	6.86	6.91
Velocity during charging (m/s)	0.14	0.80	0.83	0.84	0.85	0.85
Velocity during discharging (m/s)	0.11	0.64	0.67	0.67	0.68	0.68
Yearly OPEX (Thousands of USD / year)	0.00	44.59	97.80	151.80	206.12	260.67
Cumulative OPEX (20y) (Thousands of USD)	0.03	472.34	1036.15	1608.17	2183.67	2761.53
Electrical Fan Power (kWh_e)	0.01	1058.10	2327.74	3613.11	4903.10	6195.07
CAPEX (Thousands of USD)	1.51	1428.75	2953.32	4575.22	6294.45	8111.01
LCOS (USD/MWh_e)	4.70	5.81	6.10	6.30	6.48	6.65

Table B.5: Results obtained using multiple TES units and fixing a maximum length of the porous domain in each unit to 10 m.

Energy Storage Capacity (MWh_{th})	0.05	50.05	100.05	150.05	200.05	250.05
Number of TES units	1	1	2	2	3	3
Length of the porous domain (m)	0.81	8.06	8.06	9.23	8.87	9.56
Cross-sectional area (m^2)	0.18	18.00	17.99	23.58	21.79	25.29
Velocity during charging (m/s)	0.14	1.37	1.37	1.57	1.51	1.63
Velocity during discharging (m/s)	0.11	1.10	1.10	1.26	1.21	1.30
Yearly OPEX (Thousands of USD / year)	0.00	191.22	382.11	837.82	999.88	1541.85
Cumulative OPEX (20y) (Thousands of USD)	0.03	2025.81	4048.08	8875.83	10592.76	16334.43
Electrical Fan Power (kWh_e)	0.01	4712.12	9415.10	20714.21	24697.97	38145.29
CAPEX (Thousands of USD)	1.51	1379.52	2782.01	4172.19	5611.18	7013.52
LCOS (USD/MWh_e)	4.70	10.40	10.44	13.30	12.39	14.28